UC Berkeley
UC Berkeley Electronic Theses and Dissertations

Title

On the Dynamics of Constrained Rigid Bodies

Permalink

Author

Honein, Theresa Elie

Publication Date

2024

On the Dynamics of Constrained Rigid Bodies

By

Theresa Elie Honein

A dissertation submitted in partial satisfaction of the

requirements for the degree of

Doctor of Philosophy

in

Engineering - Mechanical Engineering

in the

Graduate Division

of the

University of California, Berkeley

Committee in charge:

Professor Oliver M. O'Reilly, Chair
Professor Lawrence C. Evans
Professor James Casey

Summer 2024

On the Dynamics of Constrained Rigid Bodies

Abstract

On the Dynamics of Constrained Rigid Bodies

by

Theresa Elie Honein

Doctor of Philosophy in Engineering - Mechanical Engineering

University of California, Berkeley

Professor Oliver M. O'Reilly, Chair

In this dissertation, the dynamics of three classic mechanical systems are examined using a combination of numerical and analytical methods. The three systems are a rolling sphere, a pair of rolling cylinders, and a stack of blocks. The kinematics and dynamics of each of these systems are governed by a set of constraints. For the sphere and cylinders the complexities of their dynamics are governed by a set of non-integrable (non-holonomic) constraints, while the complexity of the stack of blocks can be attributed to stick-slip phenomena, impacts, and a time-varying set of integrable constraints. For each of these classic systems, we establish new results.

Consider a rigid body rolling with one point in contact with a fixed surface. Now suppose that the instantaneous point of contact traces out a closed path. As a demonstration of a phenomenon known as holonomy, the body will typically not return to its original orientation. The simplest demonstration of this phenomenon in rigid body dynamics occurs in the motion of a rolling sphere and finds application to path planning and reorientation of spherical robots. Motivated by recent works of Bryant and Johnson, we establish expressions for the change in orientation (i.e., holonomy) of a rolling sphere after its center of mass completes a rectangular path. The holonomy in this case can be quantified using an angle of rotation and an axis of rotation. We use numerical methods to show that all possible changes in orientation are possible using a single rectangular path. Based on the Euler angle parameterization of a rotation, we develop a more intuitive method to achieve a desired orientation using three rectangular paths. With regards to applications, the paths we discuss can be employed to achieve any desired reorientation of a spherical robot.

The next mechanical system we examine was inspired by a common, yet hazardous, method of transporting cylindrical tanks used to carry compressed gas. The method involves rolling both tanks at opposite angles of inclination to the vertical. By propelling one of the tanks while maintaining point contact between the tanks, both tanks can be moved such that their centers of mass move in a straight line. The purpose of our work is to explore this

locomotion mechanism. First, the problem of supporting an inclined cylinder in point contact with a rough surface is examined. The analysis shows that dependent on the geometry of the cylinder and the coefficient of static friction, a wide range of angles of inclination are feasible. The presence of non-integrable constraints on the motion of the rolling cylinder is explored using the concept of a holonomy. The problem of transporting two cylinders using the aforementioned mechanism is then analyzed with the help of Frobenius' integrability criterion for constraints and numerical simulations. Our result demonstrate the surprising mechanical advantage of transporting a pair of cylinders, the range of possible angles of inclination, and the forces needed to sustain the motion.

The third mechanical system of interest is a collection of two-dimensional blocks stacked vertically. The surfaces of the blocks are rough. Of particular interest is the case where the bottom block in the stack is driven by simple harmonic motion. In the ensuing motion, a typical block in the stack can be at rest, sliding, rotating, or sliding and rotating with respect to the block underneath it. A single block in motion on a rough plane is well-known from studies in the 1980s to exhibit complex dynamics. The complexity of the dynamics of a stack of blocks dramatically increases as the number of blocks increases. In addition, the challenges to numerically investigate the dynamics are considerable. In this dissertation, we adapt a nonsmooth generalized-alpha method for systems with frictional contact to compute the dynamics of the stack. From the simulations we observe that high-frequency excitations of the bottom block tend to stabilize the stack. Our simulations also reveal the existence of an abundance of distinct solutions stemming from a unique initial configuration and excitation of the bottom block. Many, but not all, of these motions result in the toppling of the stack of blocks: a result that illustrates the surprisingly complex dynamics of a simple mechanical system and has application to robotic manipulation of stacks of objects.

To my parents, Elie and Dolly

Contents

List of Figures

Acknowledgments

I truly believe that God's hand is with me through my academic career because nothing else can explain the amazing people and the wonderful circumstances that got me to this point.

I would like to express my deepest gratitude for my advisor, Professor Oliver O'Reilly, for his guidance, kindness, and patience. His dedication to making research relevant, rigorous, clear and elegant is now imprinted in me.

I am very grateful for the interactions I have had with students throughout my teaching experiences, and I am also especially grateful to Professor James Casey and Professor Noel Perkins who have mentored me in teaching over numerous semesters. I have learned so much from their student-centric and uncompromising teaching.

I have been fortunate to take classes with the amazing mechanics faculty here at Berkeley. In addition to Professor O'Reilly and Professor Casey, Professor Papadopoulos and Professor Steigmann have been very influential to me. I have also been very fortunate to take two classes in optimization with Professor Lawrence Craig Evans.

Many thanks to all my colleagues in the Dynamics Lab: Evan Hemingway, Nathaniel Goldberg, and Brian Muldoon; and to the fellow Mechanics and Dynamics students, Milad Shirani, Roshan Mathew Tom, Jason Byun, and Ian Li, whose company I have greatly enjoyed. I would also like to mention Andre Montes and Haley Wohlever, with whom I have had great conversations around Etcheverry Hall.

I also need to thank the Professors at my undergraduate institution, especially Professor Elie Honein, my father and first mentor. Also, many thanks to my uncle, Dr. Tony Honein, for answering my random questions and recommending books for topics in mathematics, mechanics and beyond.

I would like to thank Professor Olivier Brüls from the University of Liège in Belgium and Dr.-Ing. Giuseppe Capobianco from the Institute of Applied Dynamics at Friedrich-Alexander-Universität Erlangen-Nürnberg for their technical advice and assistance.

Most importantly, my deepest gratitude goes to my parents, Elie and Dolly, for being the caring, strong willed, brilliant people that they are. I cannot thank them enough for all they do for me. Back when I was receiving graduate school decisions from universities across the US, my mom was adamant that I will hear positively from Berkeley. To my siblings, Victor and Christian, my life would be so boring without you. I wish you good health and great success.

Chapter 1

Introduction

Constraints dictate the configurations and motions of mechanical systems. Each constraint or set of constraints acting on a system can be classified as holonomic (integrable) or nonholonomic (nonintegrable). The integrability of constraints can be determined using Frobenius' integrability criteria [62]. For systems with nonholonomic constraints, the Newton-Euler and Lagrange equations of motion are coupled with the nonholonomic constraint forces, thus complicating the numerical solutions of the equations of motion. There exists alternative formulations of the equations of motion that decouple them from nonholonomic constraint forces, thus making them more amenable to numerical solutions [35]. Discontinuities arising from unilateral contact constraints subject to Coulomb friction present added difficulties in the numerical solution of equations of motion.

In this dissertation, we consider the effect of constraints on three mechanical systems and adapt novel methods to deal with the previously described difficulties. Specifically, the dynamics of three classic mechanical systems are examined using a combination of numerical and analytical methods. The three systems are a rolling sphere, a pair of rolling cylinders, and a stack of blocks. The kinematics and dynamics of each of these systems are governed by a set of constraints. For the sphere and cylinders the complexities of their dynamics are governed by a set of non-integrable (non-holonomic) constraints, while the complexity of the stack of blocks can be attributed to stick-slip phenomena, impacts, and a time-varying set of integrable constraints. For each of these classic systems, we establish new results.

1.1   The Three Mechanical Systems of Interest

Consider a rigid body rolling with one point in contact with a fixed surface. Studies of a sphere rolling without slipping on a horizontal rough surface have a celebrated history beginning with Leonhard Euler in the 18th century and including important contributions by Gaspard-Gustave Coriolis in the 19th century [54, 62]. Now suppose that the instantaneous point of contact traces out a closed path in the plane. As a demonstration of a phenomenon known as holonomy, the body will typically not return to its original orientation. The

simplest demonstration of this phenomenon in rigid body dynamics occurs in the motion of a rolling sphere and finds application to path planning and reorientation of spherical robots. Motivated by recent works of Bryant [12] and Johnson [38], in Chapter 2, we establish expressions for the change in orientation (i.e., holonomy) of a rolling sphere after its center of mass completes a rectangular path. The holonomy in this case can be quantified using an angle of rotation ψ and an axis of rotation $\mathbf{s}$. We use numerical methods to show that all possible changes in orientation are possible using a single rectangular path. These results from this numerical investigation are not transparent and we were interested in finding an easier way of prescribing paths to achieve a given holonomy. Based on the Euler angle parameterization of a rotation, we develop a more intuitive method to achieve a desired orientation using three rectangular paths. With regards to applications, the paths we discuss can be employed to achieve any desired reorientation of a spherical robot - such as the Star Wars Robot BB-8. The work presented in Chapter 2 was previously published in the journal article [33].[1]

The next mechanical system we examine was inspired by a common, yet hazardous, method of transporting cylindrical tanks used to carry compressed gas. The method involves rolling both tanks at opposite angles of inclination to the vertical. By propelling one of the tanks while maintaining point contact between the tanks, both tanks can be moved such that their centers of mass move in a straight line.[2] The purpose of our work, which is described in Chapter 3 is to explore this locomotion mechanism. First, the problem of supporting an inclined cylinder in point contact with a rough surface is examined. The analysis shows that dependent on the geometry of the cylinder and the coefficient of static friction, a wide range of angles of inclination are feasible. The presence of non-integrable constraints on the motion of the rolling cylinder is explored using the concept of a holonomy. The problem of transporting two cylinders using the aforementioned mechanism is then analyzed with the help of Frobenius' integrability criterion for constraints and numerical simulations. Our result demonstrate the surprising mechanical advantage of transporting a pair of cylinders, the range of possible angles of inclination, and the forces needed to sustain the motion.

The third mechanical system of interest is a collection of two-dimensional blocks stacked vertically where the surfaces of the blocks are rough. The dynamics of a vertical stack of blocks has application to a wide range of problems including seismic response of containers in warehouses, the stability of containers on ships at sea, and the transport of stacks of blocks by robots. There has been a growing recent interest among the robotics community in robots stacking objects vertically to form columns [25, 47] or dry stacking objects to form two-dimensional walls [49, 51]. These works have mostly relied on vision-based learning algorithms, although a few also rely on physics simulators. A central question for these stacked objects is the prediction of their dynamics when the columns are perturbed. For instance, will the column stay close to its original configuration or will it collapse? Of

---

[1]The work is also mentioned in two online articles: Researchers explore the phenomenon of holonomy and Ready to roll that appeared in the Spring and Summer, respectively, of 2024.

[2]A demonstration of this type of transport can be found online: https://youtu.be/Vgn5fv_LAk.

particular interest is the case where the bottom block in the stack is driven by simple harmonic motion. In the ensuing motion, a typical block in the stack can be at rest, sliding, rotating, or sliding and rotating with respect to the block underneath it. Earlier works on the dynamics of a single rigid block resting on a oscillating horizontal surface show a range of complex dynamics including sensitive dependence on initial conditions, bifurcations of periodic motions and chaotic motions [4, 32, 36, 37]. The complexity of the dynamics of a stack of blocks dramatically increases as the number of blocks increases. In addition, the challenges to numerically investigate the dynamics are considerable. In Chapter 4 of this dissertation, we adapt a recently-developed nonsmooth generalized-α method for systems with frictional contact to compute the dynamics of the stack [3, 10, 14, 18]. We test our numerical method on the known instability of the Leaning Tower of Lire [39]. Next, from the simulations of the stack of blocks we observe that high-frequency excitations of the bottom block tend to stabilize the stack. Our simulations also reveal the existence of an abundance of distinct solutions stemming from a unique initial configuration and excitation of the bottom block. Many, but not all, of these motions result in the toppling of the stack of blocks: a result that illustrates the surprisingly complex dynamics of a simple mechanical system and has application to robotic manipulation of stacks of objects.

A series of Appendices A-I are included in the dissertation. These appendices contain additional background information, details on algebraic calculations, and conclude with a discussion of Painlevé's paradox.

1.2   Background and Notation

Relevant background on rigid body dynamics can be found in the textbooks [54, 62] and Shuster's review article [70] on rotations. We follow the notation used in [54]. To parameterize the rotation tensor $\mathbf{Q}$ of a rigid body the a set of 3-1-3 Euler angles, ψ, ϑ, and φ, are used. The angles define the orientation of a basis $\{\mathbf{e}_1, \mathbf{e}_2, \mathbf{e}_3\}$ that corotates with the rigid body with respect to a fixed Cartesian basis $\{\mathbf{E}_1, \mathbf{E}_2, \mathbf{E}_3\}$: $\mathbf{Q} = \mathbf{e}_1 \otimes \mathbf{E}_1 + \mathbf{e}_2 \otimes \mathbf{E}_2 + \mathbf{e}_3 \otimes \mathbf{E}_3$. Here, $\otimes$ is the tensor product of two vectors. While the first and third Euler angles range from 0 to 2π, the second Euler angle, $\vartheta \in (0, \pi)$ in order to avoid a coordinate singularity associated with the Euler angle parameterization of a rotation tensor [31]. Additional details on the 3-1-3 Euler angles, including a representation for the angular velocity vector $\boldsymbol{\omega}$, the reader is referred to Appendix A.

Chapter 2

Explorations of the Holonomy of a Rolling Sphere

2.1 Introduction

Imagine a rolling sphere in motion so that its center of mass traces out a rectangular path (cf. Figure 2.1). As the center of mass of the sphere returns to the starting point of this motion, a change in orientation of the sphere may have occurred. The change in some of the states of a system when others have returned to their original values is known as a holonomy [7, 77], and the rolling sphere provides one of the simplest illustrations of a holonomy; one that is amenable to classroom demonstrations using basketballs or tennis balls. If we view the motion of the rolling sphere as simply a sequence of non-commutative rotations, then the holonomy can be readily explained. By way of contrast, the explanation for the holonomy behind another popular example, parallel parking, is far more challenging (cf. [13, 52]).

Our interest in the holonomy of the rolling sphere lies in potential application to spherical robots and was inspired by Bryant [12] and Johnson [38]. If it is possible to prescribe a rectangular path to achieve a desired reorientation, then it should be possible to use the path to reorient a spherical robot. An example illustrating the paths of two points on a rolling sphere is shown in Figure 2.1. Our goal for these motions is to establish expressions for the components of the unit quaternion representing the change in orientation of the rolling sphere (cf. (2.4.6)). For two particular types of rectangular paths, we are able to compute explicit expressions for the axis and angle of rotation of the change in orientation. These two paths are generalizations of those found previously by Johnson [38, Lemmas 1 & 2] and we use them to demonstrate how three rectangular paths can be used to produce any desired change in orientation of the rolling sphere. The demonstrations also provide a novel representation for the Euler angle parameterization of a rotation. A summary of the paths is shown in Figure 2.2: they find application to path planning for spherical robots. The three paths can be used to achieve any desired reorientation of a spherical robot. We also present numerical methods that enable us to prescribe a single rectangular path that can achieve a
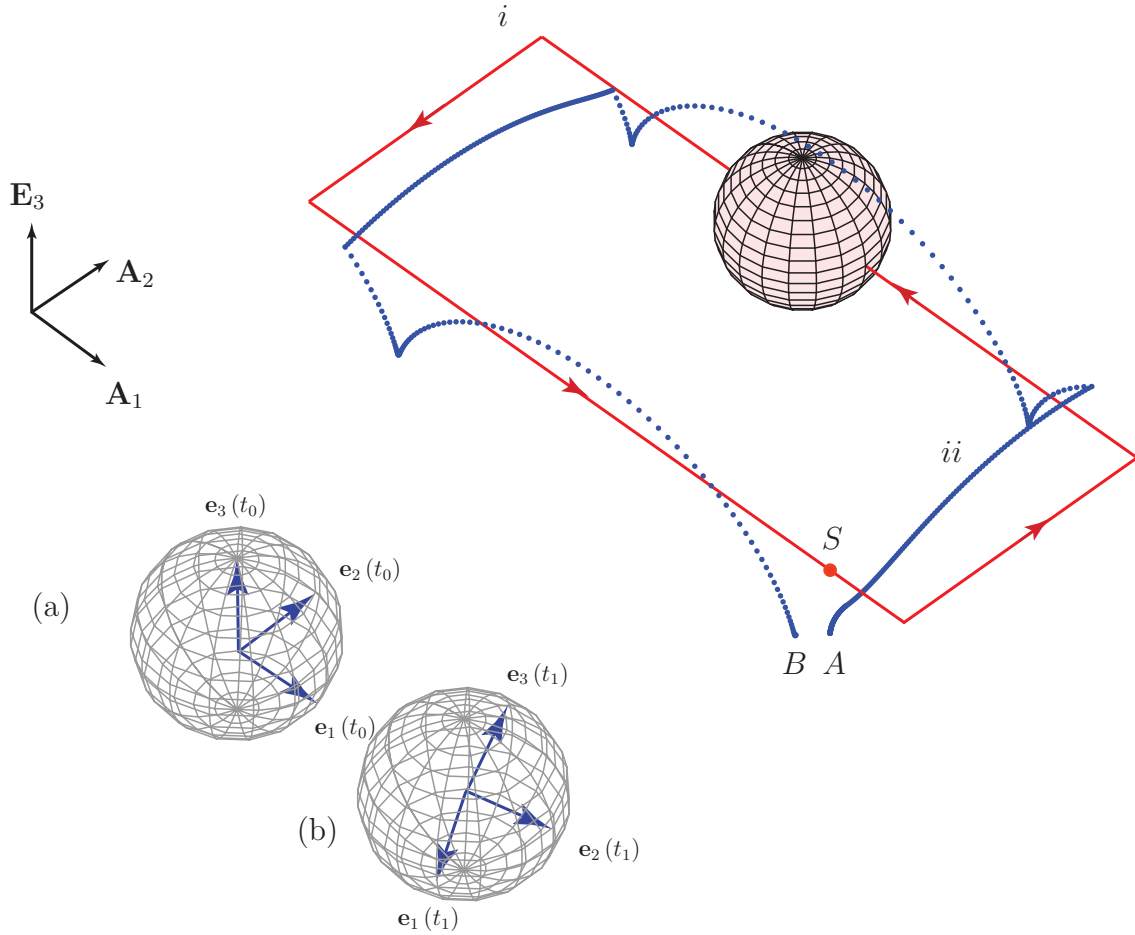
Figure 2.1: Time traces for the center of mass C and the material point X that was the initial instantaneous point of contact P during a time interval $[t_0, t_1]$. The traces are labelled i and ii, respectively. While the center of mass returns to its original location S, X has been relocated from A to B, and the sphere has reoriented from the image shown in (a) to the one shown in (b). Both the reorientation of the sphere and the relocation of X are manifestations of the holonomy. An animation of the motion can be found in the supplemental material for this chapter.

desired reorientation of a rolling sphere.

Earlier works by Bryant [12] and Johnson [38] examined the holonomy of the rolling sphere on rectangular and circular paths. In contrast to [12, 38], our analysis relies on the extensive use of rotation tensors. A second approach to computing the change in orientation of the rolling sphere could use Levi's work [48]. He showed how the change in orientation of the rolling sphere moving on a closed path can be computed using the Gauss-Bonnet theorem. Levi extended a classic (but forgotten) result on rotations by Kelvin and Tait [43,
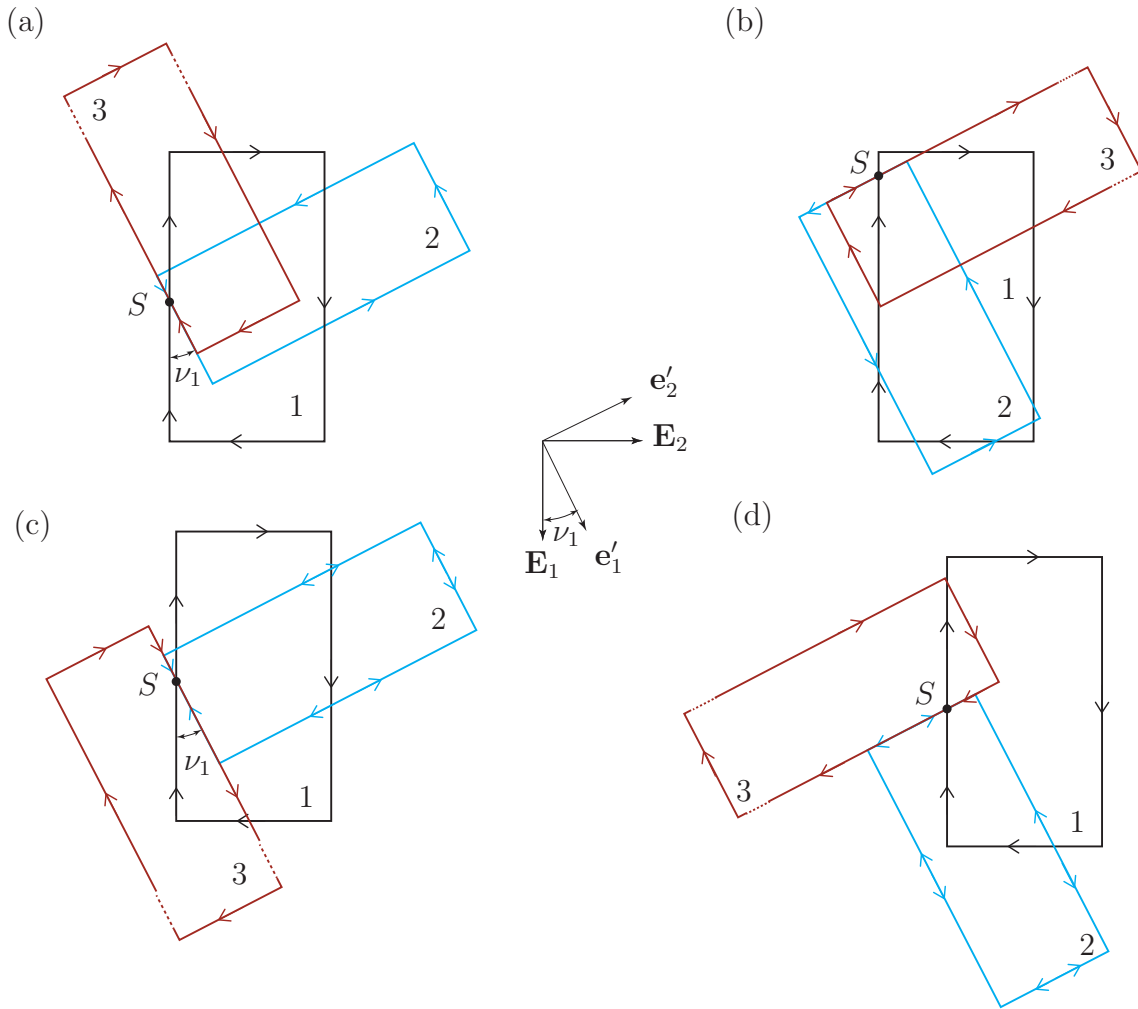
Figure 2.2: Schematic of the sequence of three rectangular paths for (a) 3-2-3, (b) 3-1-3, (c) 3-2-1, and (d) 3-1-2 sets of Euler angles.

Section 123] that can also be used to relate the change in orientation of the rolling sphere to Codman's paradox in orthopaedic biomechanics (cf. [17, 67]). A third approach is to examine the holonomy from the perspective of nonholonomic constraints. This approach involves the use Frobenius' theorem and the methods used in Burke [13] and Nelson [52] to explore parallel parking. We hope the reader finds our treatment of the holonomy complementary to the insights that can be gained from the aforementioned approaches.

Supplemental material for this chapter can be found here:
https://github.com/ThH00/Explorations-of-the-Holonomy-of-the-Rolling-Sphere

2.2   Background on Rotation Tensors

We recall, from [54], the Euler and unit quaternion parameterizations of a rotation tensor $\mathbf{R}$ in terms of an axis of rotation described by a unit vector $\mathbf{r}$ and an angle of rotation θ:

$$\begin{aligned} \mathbf{R} = \mathbf{R}\left(\theta, \mathbf{r}\right) &= \cos\left(\theta\right)\left(\mathbf{I} - \mathbf{r} \otimes \mathbf{r}\right) + \sin\left(\theta\right)\operatorname{skewt}\left(\mathbf{r}\right) + \mathbf{r} \otimes \mathbf{r} \\ &= \tilde{\mathbf{R}}\left(q_0, \mathbf{q}\right) = \left(q_0^2 - \mathbf{q}\cdot\mathbf{q}\right)\mathbf{I} + 2\mathbf{q}\otimes\mathbf{q} + 2q_0\operatorname{skewt}\left(\mathbf{q}\right), \end{aligned} \tag{2.2.1}$$

where

$$q_0 = \cos\left(\frac{\theta}{2}\right), \qquad \mathbf{q} = \sin\left(\frac{\theta}{2}\right)\mathbf{r}. \tag{2.2.2}$$

In (2.2.1) and the sequel, $\mathbf{I}$ is the identity tensor, $\operatorname{skewt}\left(\mathbf{a}\right)$ is a skew-symmetric tensor with the property that $\operatorname{skewt}\left(\mathbf{a}\right)\mathbf{b} = \mathbf{a} \times \mathbf{b}$, and $\otimes$ is the tensor product of two vectors: $\mathbf{Ib} = \mathbf{b}$ and $\left(\mathbf{b}\otimes\mathbf{c}\right)\mathbf{d} = \left(\mathbf{c}\cdot\mathbf{d}\right)\mathbf{b}$ for all $\mathbf{a}$, $\mathbf{b}$, $\mathbf{c}$, and $\mathbf{d}$. A tilde is used in (2.2.1) to distinguish the quaternion and axis-angle representations of a rotation tensor. We note the useful interpretation that the axis of rotation is a unit eigenvector of the rotation tensor: $\mathbf{Rr} = \mathbf{r}$.

As proven by Euler, a rotation tensor is proper orthogonal: $\mathbf{R}^T\mathbf{R} = \mathbf{I}$ and $\det\left(\mathbf{R}\right) = 1$ where T denotes the transpose. The representation $(2.2.1)_1$ can be used to show that the inverse rotation can be found by changing the sign of the angle of rotation or the direction of the axis of rotation:

$$\mathbf{R}^T = \mathbf{R}\left(-\theta, \mathbf{r}\right) = \mathbf{R}\left(\theta, -\mathbf{r}\right). \tag{2.2.3}$$

In addition, (2.2.1) can also be used to show the 2-1 covering of the group of rotations by the parameter pairs $\left(\theta, \mathbf{r}\right)$ and $\left(q_0, \mathbf{q}\right)$:

$$\mathbf{R}\left(\theta, \mathbf{r}\right) = \mathbf{R}\left(-\theta, -\mathbf{r}\right), \qquad \tilde{\mathbf{R}}\left(q_0, \mathbf{q}\right) = \tilde{\mathbf{R}}\left(-q_0, -\mathbf{q}\right). \tag{2.2.4}$$

The rotation tensor $\mathbf{R}$ has an associated angular velocity vector $\boldsymbol{\omega}_\mathbf{R}$:

$$\boldsymbol{\omega}_\mathbf{R} = \dot{\theta}\mathbf{r} + \sin\left(\theta\right)\dot{\mathbf{r}} + \left(1 - \cos\left(\theta\right)\right)\mathbf{r}\times\dot{\mathbf{r}}. \tag{2.2.5}$$

The angular velocity vector was computed from the identity $\operatorname{skewt}\left(\boldsymbol{\omega}_R\right) = \dot{\mathbf{R}}\mathbf{R}^T$.[1]

2.3   A Rolling Sphere

The motion of any material point X of a rigid body can be described by a translation of the center of mass C and a rotation:

$$\mathbf{x} = \mathbf{Q}\boldsymbol{\Pi} + \bar{\mathbf{x}}. \tag{2.3.1}$$

---

[1]Details on this calculation can be found in, e.g., [54, Section 6.5] or [70].

Here, $\mathbf{x}$ is the position vector of X at time t, $\mathbf{Q} = \mathbf{Q}(t)$ is a rotation tensor, $\bar{\mathbf{x}}$ is the position vector of C at time t, $\boldsymbol{\pi} = \boldsymbol{\pi}(t) = \mathbf{Q}\boldsymbol{\Pi}$ is the position vector of X relative to C at time t, and $\boldsymbol{\Pi}$ is the position vector of X relative to C in a fixed reference configuration.

In addition to the Euler and unit-quaternion parameterizations (2.2.1), there are other useful parameterizations for the rotation tensor $\mathbf{Q}$ for the rigid body. For present purposes, it is helpful to define a fixed Cartesian basis $\{\mathbf{E}_1, \mathbf{E}_2, \mathbf{E}_3\}$ for $\mathbb{E}^3$ and to define a basis $\{\mathbf{e}_1, \mathbf{e}_2, \mathbf{e}_3\}$ that corotates with the rigid body. Thus,

$$\mathbf{Q} = \sum_{k=1}^{3} \mathbf{e}_k \otimes \mathbf{E}_k, \qquad \mathbf{Q}^T = \sum_{k=1}^{3} \mathbf{E}_k \otimes \mathbf{e}_k, \qquad \mathbf{Q}\mathbf{Q}^T = \mathbf{I}, \qquad (2.3.2)$$

where $(\mathbf{a} \otimes \mathbf{b})^T = \mathbf{b} \otimes \mathbf{a}$ for all $\mathbf{a}$ and $\mathbf{b}$. Given a motion of a rigid body during a time interval $[t_0, t_1]$, the change in orientation of the rigid body is given by the relative rotation

$$\mathbf{Q}(t_1) \mathbf{Q}^T(t_0) = \sum_{k=1}^{3} \mathbf{e}_k(t_1) \otimes \mathbf{e}_k(t_0). \qquad (2.3.3)$$

In many instances, one chooses $\mathbf{e}_k(t_0) = \mathbf{E}_k$ so $\mathbf{Q}(t_0) = \mathbf{I}$.

Consider a rigid body rolling on a stationary rough plane and assume a single point P of instantaneous contact. The constraints on the motion of the rigid body are $\mathbf{v}_P = \mathbf{0}$:

$$\bar{\mathbf{v}} + \boldsymbol{\omega} \times \boldsymbol{\pi}_P = \mathbf{0}, \qquad (2.3.4)$$

where $\boldsymbol{\omega}$ is the angular velocity vector associated with the rotation $\mathbf{Q}$ of the rigid body. For convenience, we choose $\mathbf{E}_3$ to be the normal to the plane and define an additional Cartesian basis $\{\mathbf{A}_1, \mathbf{A}_2, \mathbf{A}_3 = \mathbf{E}_3\}$. As a result, $\boldsymbol{\pi}_P = -R\mathbf{E}_3$ and, with the help of (2.3.4) and the representation $\boldsymbol{\omega} = \sum_{k=1}^{3} \Omega_k \mathbf{A}_k$:

$$\bar{\mathbf{v}} = R\Omega_2 \mathbf{A}_1 - R\Omega_1 \mathbf{A}_2. \qquad (2.3.5)$$

That is, a rotation of the sphere in the $\mathbf{A}_1$ direction produces motion of the center of mass in the $\mathbf{A}_2$ direction and vice-versa. The spinning speed of the sphere, Ω_3, has no influence on the motion of the center of mass. With the help of Frobenius's Integrability Criterion, it can be shown that two of the constraints on a rolling sphere are non-holonomic (cf. [54, Section 8.5]).

We assume that the sole forces acting on the sphere of mass m are a gravitational force $-mg\mathbf{E}_3$ acting at C, a normal force $\mathbf{N} = N\mathbf{E}_3$ acting at P and a static friction force $\mathbf{F}_f = F_{f_1}\mathbf{A}_1 + F_{f_2}\mathbf{A}_2$ acting at P. A classic analysis can be used to show that the sphere will move with constant $\bar{\mathbf{v}}$ and $\boldsymbol{\omega}$, that $\mathbf{F}_f = \mathbf{0}$ and $\mathbf{N} = mg\mathbf{E}_3$, and the center of mass will move in a straight line. To initiate such a motion an angular impulse $\frac{2mR^2}{5}\boldsymbol{\omega}$ and a linear impulse $m\bar{\mathbf{v}} = mR\boldsymbol{\omega} \times \mathbf{E}_3$ are required.
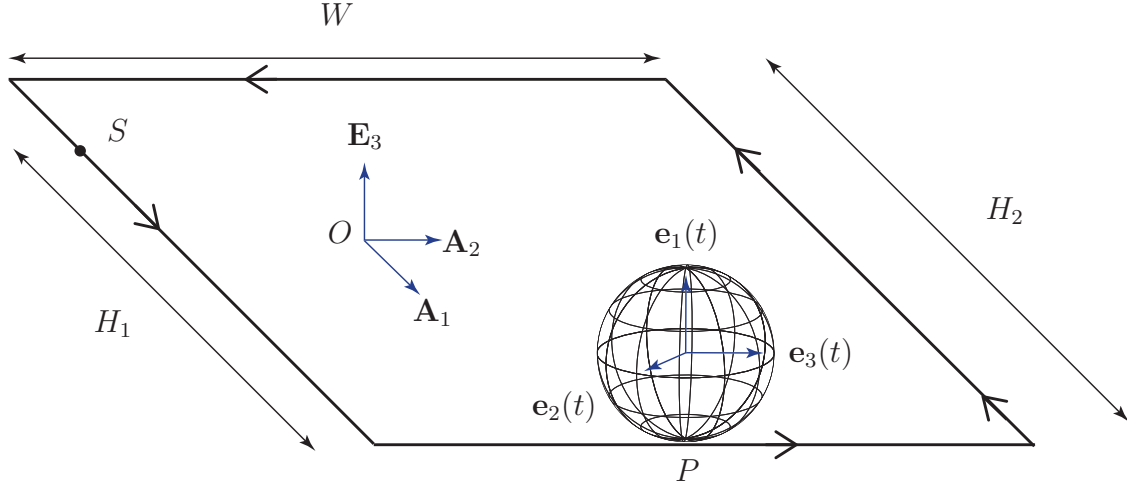
Figure 2.3: The rectangular path of the center of mass C. The sphere of radius R contacts the plane at the point S initially and the instantaneous point of contact P traces out the closed path in a counterclockwise direction during a time interval $[t_0, t_1]$. The path has dimensions $H_2 = R\varphi_2$ and $W = R\vartheta$. The starting point S is specified by the parameter $H_1 = R\varphi_1$.

2.4 Motion of a Rolling Sphere Around a Rectangular Path

Referring to Figure 2.3, we consider a rectangular path of the center of mass and assume that the center of mass is initially the point labelled S. The freedom to vary $\varphi_1 \in [0, \varphi_2]$ enables us to vary the starting point S. Applying an impulse to generate the motion and subsequent impulses to change the linear and angular velocities, the sphere's center of mass can be made to follow the rectangular path in a counterclockwise direction and return to S. The sequence of values for the angular velocity vector $\boldsymbol{\omega}$ are as follows:

$$\boldsymbol{\omega} = \mathbf{0} \rightarrow (\Omega_2 > 0)\, \mathbf{A}_1 \rightarrow (\Omega_1 < 0)\, \mathbf{A}_2 \rightarrow (\Omega_2 < 0)\, \mathbf{A}_1$$
$$\rightarrow (\Omega_1 > 0)\, \mathbf{A}_2 \rightarrow (\Omega_2 > 0)\, \mathbf{A}_1 \rightarrow \mathbf{0}. \tag{2.4.1}$$

Assuming the motion occurs during the time interval $[t_0, t_1]$, the change in orientation of the sphere is given by the tensor (cf. (2.3.3))

$$\mathbf{S} = \hat{\mathbf{S}}\left(\vartheta, \varphi_1, \varphi_2, \mathbf{A}_1, \mathbf{A}_2, \circlearrowleft\right)$$
$$= \mathbf{R}\left(\varphi_2 - \varphi_1, \mathbf{A}_2\right) \mathbf{R}\left(\vartheta, \mathbf{A}_1\right) \mathbf{R}\left(-\varphi_2, \mathbf{A}_2\right) \mathbf{R}\left(-\vartheta, \mathbf{A}_1\right) \mathbf{R}\left(\varphi_1, \mathbf{A}_2\right), \tag{2.4.2}$$

where

$$\vartheta = \frac{W}{R}, \qquad \varphi_1 = \frac{H_1}{R}, \qquad \varphi_2 = \frac{H_2}{R}. \tag{2.4.3}$$

The parameter $\circlearrowleft, \circlearrowright$ in $\hat{\mathbf{S}}$ is used to distinguish counterclockwise and clockwise directions, respectively, of circumnavigating the rectangular path. It is interesting to note that the motions we employ to locomote the sphere are geodesics on the configuration manifold $\mathbb{R}^2 \otimes SO(3)$, where $SO(3)$ is the group of rotations and the line element for the manifold is the kinematical line-element: $ds = \sqrt{\frac{2T}{m}} dt$ where T is the kinetic energy of the sphere.[2]

We note that $\mathbf{S}$ is a rotation tensor and has an associated axis $\mathbf{s}$ and angle ψ of rotation:

$$\begin{aligned} \mathbf{S} &= \hat{\mathbf{S}}\left(\vartheta, \varphi_1, \varphi_2, \mathbf{A}_1, \mathbf{A}_2, \circlearrowleft\right) \\ &= \mathbf{R}\left(\psi, \mathbf{s}\right) \\ &= \mathbf{R}\left(-\psi, -\mathbf{s}\right). \end{aligned} \tag{2.4.4}$$

A change in the orientation of the sphere can also be produced by traversing the path in the clockwise direction. It follows from (2.4.2) and (2.4.4) that the resulting change of orientation is

$$\begin{aligned} \mathbf{S}^T &= \hat{\mathbf{S}}\left(\vartheta, \varphi_1, \varphi_2, \mathbf{A}_1, \mathbf{A}_2, \circlearrowright\right) \\ &= \hat{\mathbf{S}}^T\left(\vartheta, \varphi_1, \varphi_2, \mathbf{A}_1, \mathbf{A}_2, \circlearrowleft\right) \\ &= \mathbf{R}\left(-\psi, \mathbf{s}\right) = \mathbf{R}\left(\psi, -\mathbf{s}\right). \end{aligned} \tag{2.4.5}$$

Representations for the components $S_{ik} = (\mathbf{SA}_k) \cdot \mathbf{A}_i$ of $\mathbf{S}$ can be found in Appendix B. The relation (2.4.4) can be used to show that if a path is circumnavigated n times in the same direction then the resulting reorientation has the same axis of rotation $\mathbf{s}$ and an angle of rotation of $n\psi$.

Quaternion Representation

To compute the axis $\mathbf{s}$ and angle of rotation ψ of $\mathbf{S}$, it proves insightful to use the quaternion parameterization of $\mathbf{S}$. This representation for $\mathbf{S}$ can be obtained by repeated application of the Rodrigues formula for compound rotations.[3] After a set of four successive applications of the Rodrigues formula, we find the quaternion representation for the compound rotation $\mathbf{S} = \tilde{\mathbf{S}}\left(q_0, \mathbf{q}, \mathbf{A}_1, \mathbf{A}_2, \circlearrowleft\right)$:

$$q_0 = \cos\left(\frac{\psi}{2}\right) = 1 - \sin^2\left(\frac{\vartheta}{2}\right)\sin^2\left(\frac{\varphi_2}{2}\right),$$

$$\mathbf{q} = \sin\left(\frac{\psi}{2}\right)\mathbf{s} = \sin\left(\vartheta\right)\sin\left(\frac{\varphi_2}{2}\right)\mathbf{A}_r + \sin\left(\varphi_2\right)\sin^2\left(\frac{\vartheta}{2}\right)\mathbf{A}_2, \tag{2.4.6}$$

---

[2]Additional details on geodesics of $SO(3)$ can be found in [53].

[3]Consider a pair of rotations $\mathbf{A} = \tilde{\mathbf{A}}\left(a_0, \mathbf{a}\right)$ and $\mathbf{B} = \tilde{\mathbf{B}}\left(b_0, \mathbf{b}\right)$ parameterized by unit quaternions $(a_0, \mathbf{a})$ and $(b_0, \mathbf{b})$, respectively. Then, the compound rotation $\mathbf{C} = \mathbf{BA}$ is parameterized by the unit quaternion $(c_0 = a_0 b_0 - \mathbf{a} \cdot \mathbf{b}, \mathbf{c} = a_0 \mathbf{b} + b_0 \mathbf{a} + \mathbf{b} \times \mathbf{a})$.

where

$$\mathbf{A}_r = -\cos\left(\varphi_1 - \frac{\varphi_2}{2}\right)\mathbf{A}_3 + \sin\left(\varphi_1 - \frac{\varphi_2}{2}\right)\mathbf{A}_1. \tag{2.4.7}$$

We observe immediately from (2.4.6) that while the angle of rotation ψ is independent of the starting point (i.e., φ_1), the axis of rotation $\mathbf{s}$ depends on all three angles.

Rectangular Paths that Don't Produce a Holonomy

The change in orientation of the sphere is determined by the product of five rotation tensors: $\mathbf{S} = \mathbf{R}_4\mathbf{R}_2^T\mathbf{R}_3\mathbf{R}_2\mathbf{R}_1$ where $\mathbf{R}_{1,2,3,4}$ are rotation tensors. Suppose $\mathbf{R}_2$ or $\mathbf{R}_3$ is the identity tensor $\mathbf{I}$, then $\mathbf{S} = \mathbf{I}$ and there will be no change in the orientation of the sphere (i.e., the holonomy vanishes). Other instances of $\mathbf{S} = \mathbf{I}$ can be inferred with the help of (2.4.6)$_1$. The following is a summary of all such instances:

$$\hat{\mathbf{S}}\left((2\ell-1)\pi, \varphi_1 \in [0, (2m-1)\pi], (2m-1)\pi, \mathbf{A}_1, \mathbf{A}_2, \cdot\right) = \mathbf{R}\left(2(2n-1)\pi, \mathbf{s}\right) = \mathbf{I},$$
$$\hat{\mathbf{S}}\left(2n\pi, \varphi_1 \in [0, \varphi_2], \varphi_2, \mathbf{A}_1, \mathbf{A}_2, \cdot\right) = \mathbf{R}\left(4m\pi, \mathbf{s}\right) = \mathbf{I},$$
$$\hat{\mathbf{S}}\left(\vartheta, \varphi_1 \in [0, 2n\pi], 2n\pi, \mathbf{A}_1, \mathbf{A}_2, \cdot\right) = \mathbf{R}\left(4m\pi, \mathbf{s}\right) = \mathbf{I}, \tag{2.4.8}$$

where $\ell, m, n \in \mathbb{Z}^+$ and the direction of circumnavigation can be in either the clockwise or counterclockwise directions. Thus, if the sphere rolls along any rectangular path where the length of each side is a multiple of $R\pi$ in length or the lengths of two of the sides are multiples of $2R\pi$, then the sphere will return to its original orientation. As a consequence, the material point corresponding to the instantaneous point of contact will also be the same.

A Pair of Rectangular Paths

The expressions (2.4.6) do not admit to a closed-form solution for the parameters φ_1, φ_2, and ϑ required to produce a desired axis and angle of rotation of the sphere. However, with the assistance of (2.2.1) and (2.2.2), two special cases are immediately apparent upon inspection of (2.4.6): $\varphi_2 = \pi$ and $\vartheta = \pi$. For both cases, two of the sides of the rectangle are $R\pi$ in length and they produce the following change of orientation of the sphere:

$$\hat{\mathbf{S}}\left(\vartheta, \varphi_1 \in [0, \pi], \pi, \mathbf{A}_1, \mathbf{A}_2, \circlearrowleft\right) = \mathbf{R}\left(2\vartheta, \mathbf{A}_r\right) = \mathbf{R}\left(-2\vartheta, -\mathbf{A}_r\right),$$
$$\hat{\mathbf{S}}\left(\pi, \varphi_1 \in \left[0, \frac{\varphi_2}{2}\right], \varphi_2, \mathbf{A}_1, \mathbf{A}_2, \circlearrowleft\right) = \mathbf{R}\left(2\varphi_2, \mathbf{A}_2\right) = \mathbf{R}\left(-2\varphi_2, -\mathbf{A}_2\right). \tag{2.4.9}$$

An example of (2.4.9)$_1$ is shown in Figure 2.1. For this particular example, the reorientation can be characterized as follows (cf. (2.4.2) and (2.4.4)):

$$\mathbf{S} = \hat{\mathbf{S}}\left(\frac{4\pi}{3} - 0.5, \frac{\pi}{2} - 0.4, 3\pi, \mathbf{A}_1, \mathbf{A}_2, \circlearrowleft\right)$$
$$= \mathbf{R}\left(\psi = 62.7042°, \mathbf{s} = -0.389418\mathbf{A}_1 - 0.921061\mathbf{A}_3\right). \tag{2.4.10}$$
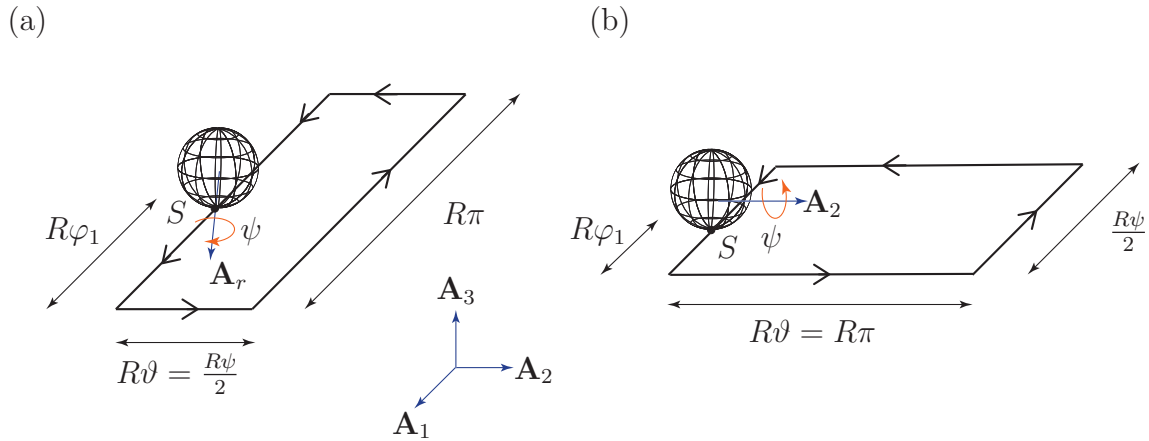
Figure 2.4: Two rectangular paths. In (a), the sphere will have rotated through a counter-clockwise angle $\psi = 2\vartheta$ about $\mathbf{A}_r$ after circumnavigating the path in the counterclockwise ($\circlearrowleft$) direction. In (b), the sphere will have rotated through a counterclockwise angle $\psi = 2\varphi_2$ about $\mathbf{A}_2$ after circumnavigating the path in the counterclockwise ($\circlearrowleft$) direction. The rotations of the sphere for (a) and (b) are given by $(2.4.9)_1$ and $(2.4.9)_2$, respectively.

For the resulting motion of the sphere, $\mathbf{e}_3(t_0) = \mathbf{E}_3$ and $\mathbf{e}_3(t_1) = 0.194194\mathbf{A}_1 + 0.346057\mathbf{A}_2 + 0.917896\mathbf{E}_3$.

The two motions $(2.4.9)_{1,2}$ can be considered as generalizations of Lemmas 1 and 2, respectively, in Johnson [38]. In addition, the rectangular paths associated with this pair of motions will be of particular interest when we examine the Euler angle parameterization of a rotation (cf. Figure 2.4). Lemma 1 in [38] states that traversing a rectangular path where $\varphi_1 = \frac{\pi}{2}$ and $\varphi_2 = \pi$ will produce a holonomy of the sphere that has an counterclockwise angle of rotation $\psi = 2\vartheta$ about an axis of rotation $-\mathbf{A}_3 = -\mathbf{E}_3$. By allowing other values of φ_1, we find that the rectangular path will produce a holonomy of the sphere corresponding to a rotation about $\psi = 2\vartheta$ about an axis $\mathbf{A}_r$. An example of the corresponding path is shown in Figure 2.4(a). It is remarkable that by rotating the sphere successively about $\mathbf{A}_2$, $\mathbf{A}_1$, $\mathbf{A}_2$, $\mathbf{A}_1$, and $\mathbf{A}_2$ has produced a clockwise rotation of 2ϑ about $\mathbf{A}_r$. In addition, by varying the starting point of the motion, we can produce an axis of rotation that has a horizontal component. Lemma 2 in [38] states that traversing a rectangular path where $\varphi_1 = 0$ and $\vartheta = \pi$ will produce a holonomy of the sphere that has an counterclockwise angle of rotation $\psi = 2\varphi_2$ about an axis of rotation $\mathbf{A}_2$. Our results show that the same rotation can be achieved for any $\varphi_1 \leq \varphi_2$. An example of the corresponding rectangular path is shown in Figure 2.4(b).
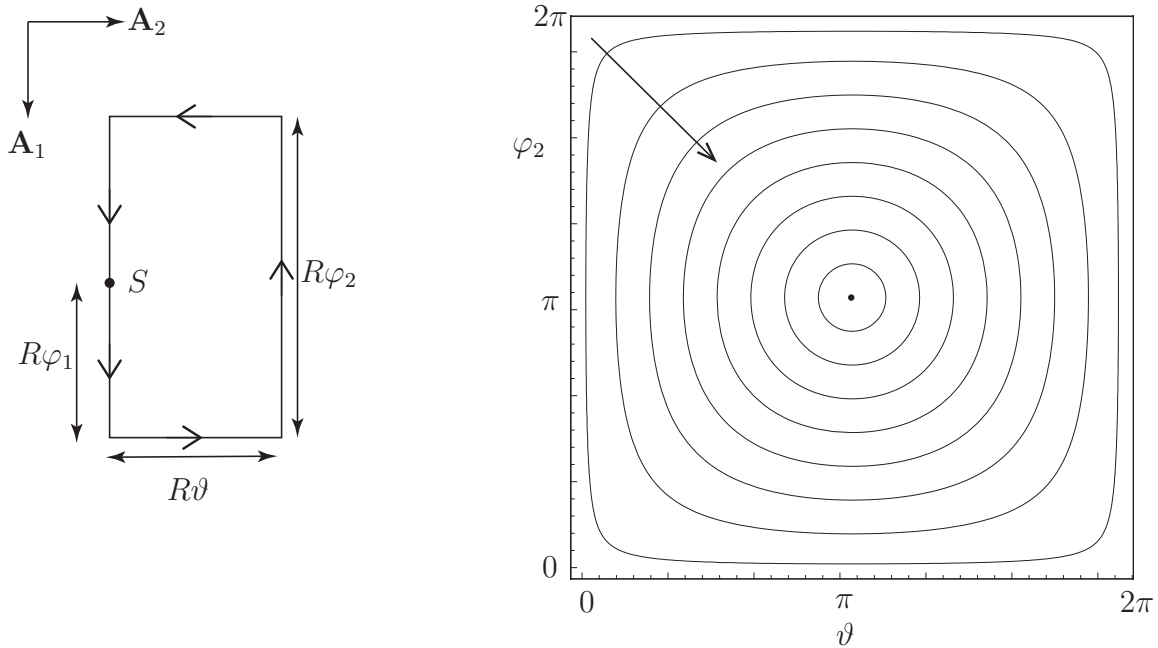
Figure 2.5: Level sets of the angle of rotation ψ of the rotation $\mathbf{S} = \hat{\mathbf{S}} \left(\vartheta, \varphi_1, \varphi_2, \mathbf{A}_1, \mathbf{A}_2, \circlearrowleft \right)$ defined in (2.4.2) as a function of the angles of rotations ϑ and φ_2. The results are computed using (2.4.11). The inset image shows the rectangular path taken by the sphere and the dimensions of the path. The arrow indicates the direction of increasing value of ψ and the level sets shown are for $\psi = 5^o$, $\psi = 45^o$, $\psi = 90^o$, $\psi = 135^o$, $\psi = 180^o$, $\psi = 225^o$, $\psi = 270^o$, and $\psi = 315^o$. When $\vartheta = \varphi_2 = \pi$, the angle of rotation $\psi = 2\pi$: i.e., $\mathbf{S} = \mathbf{I}$.

Finding a Rectangular Path That Produces a Prescribed Holonomy

We next seek to explore the possibility of prescribing a rectangular path so the reorientation of the sphere by any rotation $\mathbf{R} \left(\psi, \mathbf{s} \right)$ can be achieved. That is, given ψ and $\mathbf{s}$, we seek to determine φ_1, φ_2, and ϑ such that (2.4.6) are satisfied. We first examine the range of possible ψ using numerical methods and compute the angle of rotation ψ as a function of ϑ and φ_2, $\psi = \hat{\psi} \left(\vartheta, \varphi_2 \right)$, using (2.4.6)$_1$:

$$\cos \left(\frac{\psi}{2} \right) = 1 - \sin^2 \left(\frac{\vartheta}{2} \right) \sin^2 \left(\frac{\varphi_2}{2} \right). \tag{2.4.11}$$

The results are shown in Figure 2.5 for values of ϑ and φ_2 in the range of 0 to 2π and are readily extended to other values of these angles. Referring to Figure 2.5, it is possible to achieve any angle of rotation by appropriately choosing ϑ and φ_2 and, apart from values of 0 or 2π, every angle of rotation ψ is associated with a one-parameter family of values of ϑ and φ_2. It is tempting to conclude that given any $(\psi, \mathbf{s})$, a rectangular path can be

constructed by appropriate choice of the three parameters ϑ, φ_1, and φ_2, but before drawing such a conclusion we need to examine $\mathbf{s} = \hat{\mathbf{s}}(\vartheta, \varphi_1, \varphi_2)$.

Ideally, we would like to prove that a three-parameter (ϑ, φ_1, and φ_2) rectangular path can be found for any pair of $\mathbf{s}$ and ψ. However, apart from the cases $\mathbf{s} = \mathbf{A}_r$ and $\mathbf{s} = \mathbf{A}_2$ discussed in Section 2.4, we needed to resort to numerical methods to explore if it was possible to find a triple $(\vartheta, \varphi_1, \varphi_2)$ for any given pair $(\mathbf{s}, \psi)$. An outline of the numerical algorithm is presented in Appendix C. By searching over all possible pairs $(\mathbf{s}, \psi)$, our numerical work demonstrated that a rectangular path could be constructed such that a sphere circumnavigating the path would experience a desired holonomy.
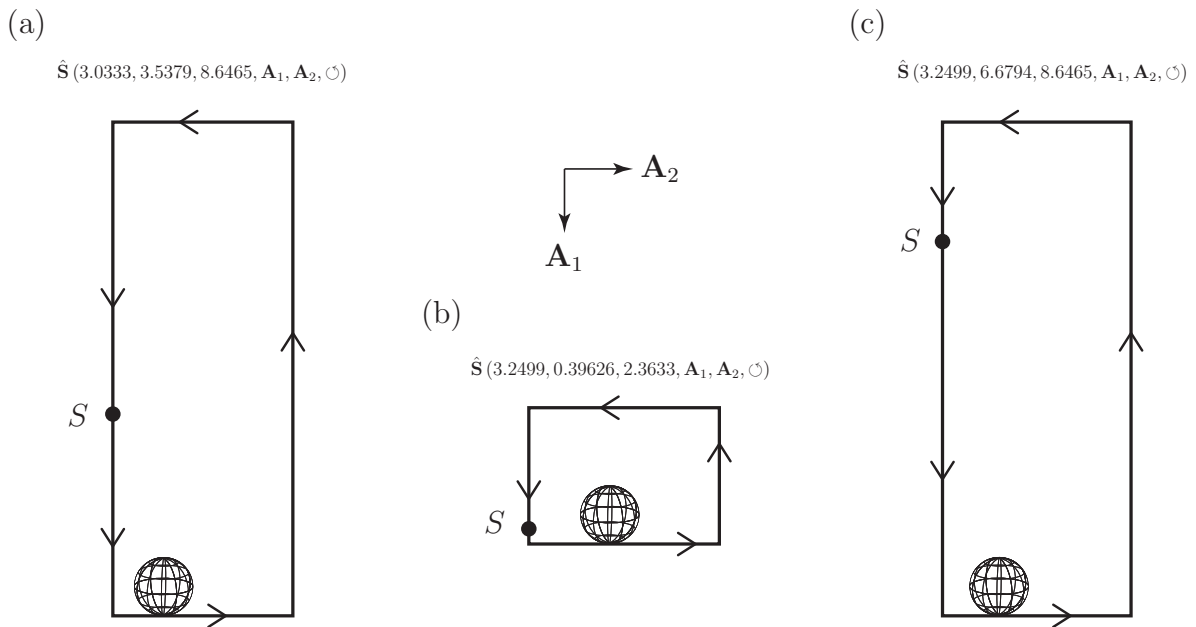
Figure 2.6: Scaled images of the three rectangular paths that produce the following holonomy of a rolling sphere: $\mathbf{R}\left(\frac{3\pi}{2}, 0.1\mathbf{A}_1 + \sqrt{0.98}\mathbf{A}_2 + 0.1\mathbf{A}_3\right)$. From (a)–(c), the paths are described by $(2.4.12)_{1,2,3}$, respectively.

Because a holonomy remains unchanged when the lengths of the sides of the rectangle are increased by multiples of $2\pi R$, the path associated with a holonomy is always non-unique. In addition to this non-uniqueness, we also find instances where a given holonomy can be achieved by three distinct rectangular paths where the breadth and height of the rectangles are not related by multiples of $2\pi R$. For example, the following rotation can be achieved

using three distinct rectangular paths:

$$
\mathbf{R}\left(\frac{3\pi}{2}, 0.1\mathbf{A}_1 + \sqrt{0.98}\mathbf{A}_2 + 0.1\mathbf{A}_3\right) = \hat{\mathbf{S}}\left(3.0333, 3.5379, 8.6465, \mathbf{A}_1, \mathbf{A}_2, \circlearrowleft\right)
$$
$$
= \hat{\mathbf{S}}\left(3.2499, 0.39626, 2.3633, \mathbf{A}_1, \mathbf{A}_2, \circlearrowleft\right)
$$
$$
= \hat{\mathbf{S}}\left(3.2499, 6.6794, 8.6465, \mathbf{A}_1, \mathbf{A}_2, \circlearrowleft\right). \qquad (2.4.12)
$$

The paths are shown in Figure 2.6 and the code used to compute the solutions can be found in the supplemental materials for this chapter.

The complexity of finding the three parameters associated with a given rotation contrasts with the simplicity of the Euler angle representation for a rotation. This difference led us to explore the use of three rectangular paths to achieve any desired holonomy of the rolling sphere. The paths and their relation to the Euler angle parameterization of a rotation are discussed in the next section.

2.5   Euler Angles and the Motion of a Sphere

The Euler angle parameterization of a rotation tensor $\mathbf{T}$ can be visualized as a decomposition of $\mathbf{T}$ into the product of three rotations. There are 12 possible sets of Euler angles and several techniques can be used to visualize them. The first dates to Euler [21] and uses spherical geometry to show a set of symmetric Euler angles, such as the 3-1-3 and 3-2-3 sets, on the unit sphere.[4] The second visualization can be traced to Lagrange [46] in 1870 and equates the first Euler angle to the precession, the second Euler angle to the nutation, and the third Euler angle to the spin of a celestial body. The asymmetric sets of Euler angles, such as the 3-1-2 and 3-2-1 sets, were first formulated in optometry in the 1840s [22, 28, 30] and aerodynamics in the late 1800s and early 1900s [11, 73]. The asymmetric sets are readily visualized as the yaw, pitch, and roll motions of a vehicle. We now present a new method of defining the 3-1-3, 3-2-3, 3-2-1, and 3-1-2 sets of Euler angles that exploits holonomy. In particular, we demonstrate how a succession of three rectangular paths can be used to produce any orientation of the sphere. A summary of the paths was shown previously in Figure 2.2. In the construction, we make liberal use of the freedom to increase the length of a side of a rectangle by a multiple of $2R\pi$ without changing the resulting rotation of the sphere along that particular side. The developments are followed by a discussion of Euler angle singularities.[5]

---

[4]Junkins and Shuster [40] have a detailed discussion of this topic.

[5]The reader is referred to Appendix A for additional details on the 3-1-3 Euler angles.

The 3-2-3 and 3-1-3 sets of Euler Angles

For the 3-2-3 set, the first rotation is defined about $\mathbf{E}_3$ through a counterclockwise angle ν_1. This rotation can be used to define a second basis:

$$\mathbf{e}_1' = \cos\left(\nu_1\right)\mathbf{E}_1 + \sin\left(\nu_1\right)\mathbf{E}_2, \quad \mathbf{e}_2' = -\sin\left(\nu_1\right)\mathbf{E}_1 + \cos\left(\nu_1\right)\mathbf{E}_2, \quad \mathbf{e}_3' = \mathbf{E}_3. \quad (2.5.1)$$

The second rotation is about $\mathbf{e}_2'$ through a counterclockwise angle of rotation ν_2:

$$\mathbf{e}_1'' = \cos\left(\nu_2\right)\mathbf{e}_1' - \sin\left(\nu_2\right)\mathbf{e}_3', \quad \mathbf{e}_2'' = \mathbf{e}_2', \quad \mathbf{e}_3'' = \sin\left(\nu_2\right)\mathbf{e}_1' + \cos\left(\nu_2\right)\mathbf{e}_3'. \quad (2.5.2)$$

The third and final rotation is a rotation about $\mathbf{e}_3''$ through a counterclockwise angle of rotation ν_3:

$$\mathbf{e}_1 = \cos\left(\nu_3\right)\mathbf{e}_1'' + \sin\left(\nu_3\right)\mathbf{e}_2'', \quad \mathbf{e}_2 = -\sin\left(\nu_3\right)\mathbf{e}_1'' + \cos\left(\nu_3\right)\mathbf{e}_2'', \quad \mathbf{e}_3 = \mathbf{e}_3''. \quad (2.5.3)$$

The unit vectors used to define the rotations are known as the Euler basis vectors:

$$\left\{\mathbf{g}_1 = \mathbf{E}_3, \mathbf{g}_2 = \mathbf{e}_2', \mathbf{g}_3 = \mathbf{e}_3''\right\}. \quad (2.5.4)$$

Combining the aforementioned rotations, we arrive at the representation:

$$\mathbf{T} = \bar{\mathbf{T}}_{3-2-3}\left(\nu_1, \nu_2, \nu_3\right) = \sum_{i=1}^{3}\mathbf{e}_i \otimes \mathbf{E}_i = \mathbf{R}\left(\nu_3, \mathbf{e}_3''\right)\mathbf{R}\left(\nu_2, \mathbf{e}_2'\right)\mathbf{R}\left(\nu_1, \mathbf{E}_3\right). \quad (2.5.5)$$

The corresponding developments for the 3-1-3 set produce the representation:

$$\mathbf{T} = \bar{\mathbf{T}}_{3-1-3}\left(\nu_1, \nu_2, \nu_3\right) = \sum_{i=1}^{3}\mathbf{e}_i \otimes \mathbf{E}_i$$
$$= \mathbf{R}\left(\nu_3, \mathbf{e}_3'' = \cos\left(\nu_2\right)\mathbf{E}_3 - \sin\left(\nu_2\right)\mathbf{e}_2'\right)\mathbf{R}\left(\nu_2, \mathbf{e}_1'\right)\mathbf{R}\left(\nu_1, \mathbf{E}_3\right). \quad (2.5.6)$$

For convenience, we use the same notation for both sets of angles.

For ease of exposition, we first consider the 3-2-3 set of Euler angles. Now, imagine a rolling sphere where the center of mass describes a series of 3 rectangular paths and returns to its original starting point S. The paths are shown in Figure 2.7. The starting point for the first path is located at the midpoint of the side of a rectangle of height $R\pi$ and breadth $\frac{R\nu_1}{2}$:

$$\hat{\mathbf{S}}\left(\frac{\nu_1}{2}, \frac{\pi}{2}, \pi, \mathbf{E}_1, \mathbf{E}_2, \circlearrowright\right) = \mathbf{R}\left(\nu_1, \mathbf{E}_3\right). \quad (2.5.7)$$

After the sphere has circumnavigated the rectangle in the clockwise direction, a rotation of ν_1 about an axis $\mathbf{E}_3$ will have been achieved. The second motion is a counterclockwise path about a rectangle which has a base of length $R\pi$ and height $\frac{R\nu_2}{2}$. The rectangle is rotated so
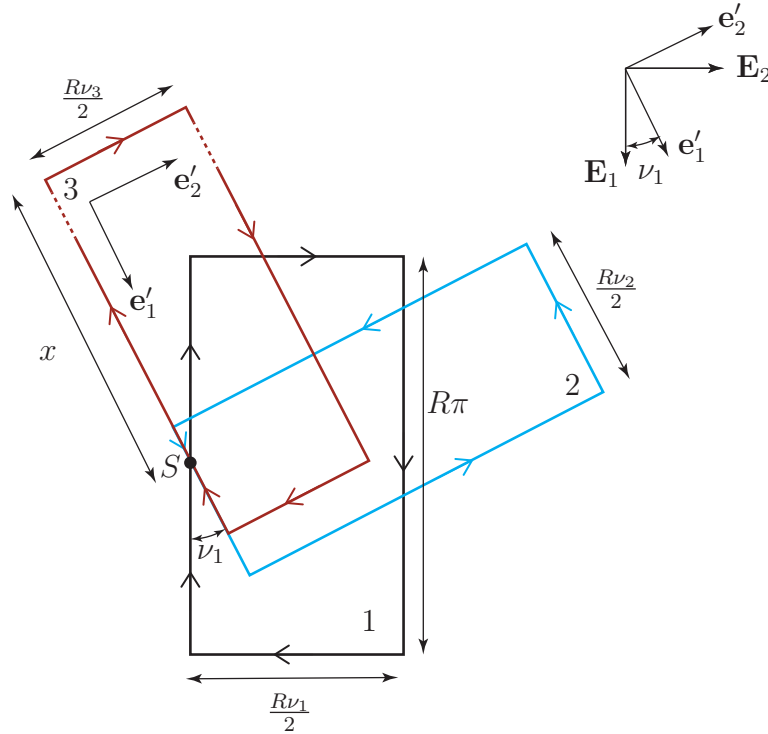
Figure 2.7: The three motions for the set of 3-2-3 Euler angles: ν_1, ν_2, and ν_3. The first rectangular path (labelled 1) has a base of length $\frac{R\nu_1}{2}$ and height $R\pi$. The second rectangular path (labelled 2) has base of length $R\pi$ and height $\frac{R\nu_2}{2}$. The third, and final rectangular path (labelled 3) has a base of length $\frac{R\nu_3}{2}$ and height $3R\pi$. The parameter $x = R\left(\frac{\pi}{2} + \nu_2\right)$ defines the location of S on the third rectangle. Observe that the second and third paths have been rotated by an angle of ν_1 to the horizontal.

that the base is parallel to $\mathbf{e}_2'$.[6] After the sphere has circumnavigated the second rectangle, a rotation of ν_2 about an axis $\mathbf{e}_2'$ will have been achieved. That is,

$$\hat{\mathbf{S}}\left(\pi, \varphi_1 \in \left[0, \frac{\nu_2}{2}\right], \frac{\nu_2}{2}, \mathbf{e}_1', \mathbf{e}_2', \circlearrowleft\right) = \mathbf{R}\left(\nu_2, \cos\left(\nu_1\right)\mathbf{E}_2 - \sin\left(\nu_1\right)\mathbf{E}_1\right). \qquad (2.5.8)$$

For the 3-2-3 set of Euler angles, ν_2 is positive so the second rectangular path is always traversed in a counterclockwise direction. For the third, and final, rotation, we consider a rectangle with a base of length $\frac{R\nu_3}{2}$ and height $3R\pi$. That is, $\varphi_2 = 3\pi$. To determine S and the orientation of the rectangle, we observe that for the third rotation and concomitant rectangular path, the axes of rotation for the ensuing motion of the sphere are given by the following respective representations (cf. (2.4.6) and (2.4.7)):

$$\mathbf{e}_3'' = \sin\left(\nu_2\right)\mathbf{e}_1' + \cos\left(\nu_2\right)\mathbf{e}_3',$$
$$\mathbf{s}_3 = \sin\left(\varphi_1\right)\mathbf{A}_3 + \cos\left(\varphi_1\right)\mathbf{A}_1. \qquad (2.5.9)$$

---

[6]That is, the basis vectors $\mathbf{A}_1$ and $\mathbf{A}_2$ in Figure 2.5 are chosen to be $\mathbf{e}_1'$ and $\mathbf{e}_2'$, respectively.

To align these vectors and accommodate the range $[0, \pi]$ of ν_2, φ_1, $\mathbf{A}_1$, and $\mathbf{A}_3$ are prescribed as follows:

$$\varphi_1 = \frac{5\pi}{2} - \nu_2, \qquad \mathbf{A}_1 = \mathbf{e}_1', \qquad \mathbf{A}_3 = \mathbf{e}_3' = \mathbf{E}_3. \tag{2.5.10}$$

That is, the starting point and orientation of the rectangle are chosen judiciously so that the axis of rotation for the resulting motion of the sphere will be parallel to $\mathbf{e}_3''$. After the sphere has circumnavigated the third rectangle in the clockwise direction, a rotation of ν_3 about an axis $\mathbf{e}_3''$ will have been achieved. That is,

$$\hat{\mathbf{S}}\left(\frac{\nu_3}{2}, \frac{5\pi}{2} - \nu_2, 3\pi, \mathbf{e}_1', \mathbf{e}_2', \circlearrowright\right) = \mathbf{R}\left(\nu_3, \mathbf{e}_3''\right). \tag{2.5.11}$$

Combining the results (2.5.7), (2.5.8), and (2.5.11), we arrive at the conclusion:

$$\bar{\mathbf{T}}_{3-2-3}\left(\nu_1, \nu_2, \nu_3\right) = \hat{\mathbf{S}}\left(\frac{\nu_3}{2}, \frac{5\pi}{2} - \nu_2, 3\pi, \mathbf{e}_1', \mathbf{e}_2', \circlearrowright\right) \hat{\mathbf{S}}\left(\pi, \varphi_1 \in \left[0, \frac{\nu_2}{2}\right], \frac{\nu_2}{2}, \mathbf{e}_1', \mathbf{e}_2', \circlearrowright\right)$$
$$\times \hat{\mathbf{S}}\left(\frac{\nu_1}{2}, \frac{\pi}{2}, \pi, \mathbf{E}_1, \mathbf{E}_2, \circlearrowright\right). \tag{2.5.12}$$

That is, the 3-2-3 set of Euler angles can be defined by the change in orientation achieved by rolling a sphere that has travelled along a set of three consecutive rectangular paths. An animation of this type of reorientation can be found in the supplemental materials for this chapter.

For the 3-1-3 set of Euler angles, the first rectangular path is identical to the one used for the 3-2-3 set of Euler angles (cf. (2.5.7)). The second rotation is about $\mathbf{e}_1'$ and, thus, we now choose the second rectangular path to have a base of length $R\pi$ and a height of $\frac{R\nu_2}{2}$. The rectangle is oriented so $\mathbf{A}_1 = -\mathbf{e}_2'$ and $\mathbf{A}_2 = \mathbf{e}_1'$:

$$\hat{\mathbf{S}}\left(\pi, \varphi_1 \in \left[0, \frac{\nu_2}{2}\right], \frac{\nu_2}{2}, -\mathbf{e}_2', \mathbf{e}_1', \circlearrowright\right) = \mathbf{R}\left(\nu_2, \cos\left(\nu_1\right)\mathbf{E}_1 + \sin\left(\nu_1\right)\mathbf{E}_2\right). \tag{2.5.13}$$

The third rectangle has a base of length $\frac{R\nu_3}{2}$ and a height of $3R\pi$, and will be circumnavigated in the clockwise direction. To prescribe the location of the starting point S and the angle φ_1, we note that

$$\mathbf{e}_3'' = -\sin\left(\nu_2\right)\mathbf{e}_2' + \cos\left(\nu_2\right)\mathbf{e}_3',$$
$$\mathbf{s}_3 = \sin\left(\varphi_1\right)\mathbf{A}_3 + \cos\left(\varphi_1\right)\mathbf{A}_1. \tag{2.5.14}$$

To align these vectors and accommodate the range $[0, \pi]$ of ν_2, φ_2, $\mathbf{A}_1$, and $\mathbf{A}_3$ are prescribed as follows:

$$\varphi_1 = \frac{5\pi}{2} - \nu_2, \qquad \mathbf{A}_1 = -\mathbf{e}_2', \qquad \mathbf{A}_3 = \mathbf{e}_3' = \mathbf{E}_3. \tag{2.5.15}$$
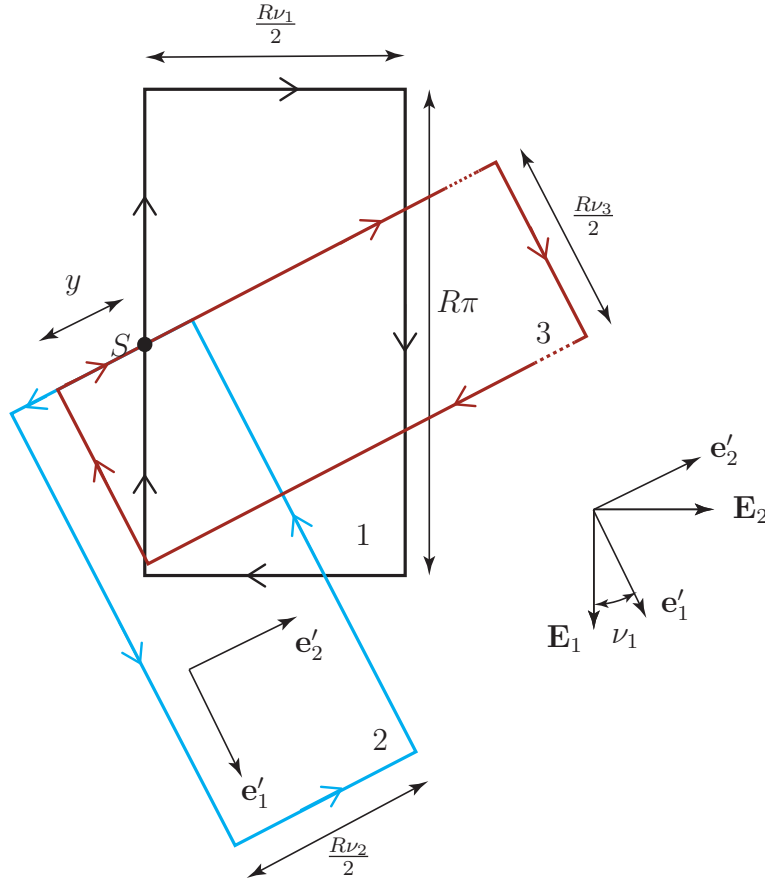
Figure 2.8: The three motions for the set of 3-1-3 Euler angles: ν_1, ν_2, and ν_3. The first rectangular path (labelled 1) has a base of length $\frac{R\nu_1}{2}$ and height $R\pi$. The second rectangular path (labelled 2) has base of length $R\pi$ and height $\frac{R\nu_2}{2}$. The third, and final rectangular path (labelled 3) has a base of length $\frac{R\nu_3}{2}$ and height $3R\pi$. For the 3-1-3 set of Euler angles, $\nu_2 \in [0, \pi]$ and $y = \frac{5R\pi}{2} - R\nu_2$.

In conclusion:

$$\bar{\mathbf{T}}_{3-1-3}\left(\nu_1, \nu_2, \nu_3\right) = \hat{\mathbf{S}}\left(\frac{\nu_3}{2}, \frac{5\pi}{2} - \nu_2, 3\pi, -\mathbf{e}_2', \mathbf{e}_1', \circlearrowleft\right) \hat{\mathbf{S}}\left(\pi, \varphi_1 \in \left[0, \frac{\nu_2}{2}\right], \frac{\nu_2}{2}, -\mathbf{e}_2', \mathbf{e}_1', \circlearrowleft\right)$$

$$\times \hat{\mathbf{S}}\left(\frac{\nu_1}{2}, \frac{\pi}{2}, \pi, \mathbf{E}_1, \mathbf{E}_2, \circlearrowleft\right). \tag{2.5.16}$$

The rectangular paths are shown in Figure 2.8.

The 3-2-1 and 3-1-2 sets of Euler Angles

The construction for the 3-2-1 and 3-1-2 sets follow those for the 3-2-3 and 3-1-3 sets, respectively, with two modifications. The first of these modifications accommodates the

range of the second Euler angle for the asymmetric sets: $\nu_2 \in \left[-\frac{\pi}{2}, \frac{\pi}{2}\right]$. To accommodate the range, the second rectangle, which has a breadth of $\frac{R}{2}\left|\nu_2\right|$ is circumnavigated in the clockwise direction if $\nu_2 < 0$ and counterclockwise direction if $\nu_2 > 0$. The second modification pertains to $\mathbf{s}_3$. For the 3-2-1 set of Euler angles, we can follow the developments leading to (2.5.10). We now need to prescribe φ_1, $\mathbf{A}_1$, and $\mathbf{A}_3$ such that

$$
\begin{aligned}
\mathbf{e}_1'' &= -\sin\left(\nu_2\right)\mathbf{e}_3' + \cos\left(\nu_2\right)\mathbf{e}_1', \\
\mathbf{s}_3 &= \sin\left(\varphi_1\right)\mathbf{A}_3 + \cos\left(\varphi_1\right)\mathbf{A}_1.
\end{aligned}
\tag{2.5.17}
$$

To align these vectors and accommodate the range $\left[-\frac{\pi}{2}, \frac{\pi}{2}\right]$, we prescribe

$$
\varphi_1 = \pi + \nu_2, \qquad \mathbf{A}_1 = -\mathbf{e}_1', \qquad \mathbf{A}_2 = -\mathbf{e}_2', \qquad \mathbf{A}_3 = \mathbf{e}_3' = \mathbf{E}_3.
\tag{2.5.18}
$$

That is, the third rectangle in Figure 2.7 will be rotated by 180°. The developments for the 3-1-2 set of Euler angles follow from the 3-1-3 set. In place of (2.5.14), we need to prescribe φ_1, $\mathbf{A}_1$, and $\mathbf{A}_3$ such that

$$
\begin{aligned}
\mathbf{e}_2'' &= \cos\left(\nu_2\right)\mathbf{e}_2' + \sin\left(\nu_2\right)\mathbf{e}_3', \\
\mathbf{s}_3 &= \sin\left(\varphi_1\right)\mathbf{A}_3 + \cos\left(\varphi_1\right)\mathbf{A}_1.
\end{aligned}
\tag{2.5.19}
$$

Thus,

$$
\varphi_1 = 2\pi + \nu_2, \qquad \mathbf{A}_1 = \mathbf{e}_2', \qquad \mathbf{A}_2 = -\mathbf{e}_1', \qquad \mathbf{A}_3 = \mathbf{e}_3' = \mathbf{E}_3.
\tag{2.5.20}
$$

The rectangular paths are shown in Figure 2.9. The resulting representations for $\bar{\mathbf{T}}_{3-2-1}\left(\nu_1, \nu_2, \nu_3\right)$ and $\bar{\mathbf{T}}_{3-1-2}\left(\nu_1, \nu_2, \nu_3\right)$ are readily inferred from our earlier work (cf. (2.5.12) and (2.5.16)).

Euler Angle Singularities

We note that the construction applies even when a coordinate singularity known as the Euler angle singularity is present. The arguments are similar for both the four sets of Euler angles under consideration. In the interests of brevity, we confine our comments to the 3-2-3 set of Euler angles. In order for the Euler basis to span $\mathbb{E}^3$, the basis vectors $\{\mathbf{E}_3, \mathbf{e}_2', \mathbf{e}_3''\}$ must be linearly independent. Thus, the angle ν_2 is restricted in order to avoid the coordinate singularity: $\nu_2 \in (0, \pi)$, otherwise where $\nu_2 = 0, \pi$ then $\mathbf{e}_3'' = \pm\mathbf{E}_3$ and the Euler angles fail to be a coordinate system for the group of rotations $SO(3)$. These instances are the pair of Euler angle singularities for the 3-2-3 set of Euler angles. To illustrate how this singularity manifests in the holonomy construction, consider the case $\nu_2 = \pi$. In this case, (2.5.12) can be used to show that the second rectangular path will result in a rotation of the sphere about $\mathbf{e}_2'$ of π and the third rectangular path will produce a rotation about $-\mathbf{E}_3$ through an angle ν_3, as expected.

2.6 Closing Remarks

The holonomies we have discussed have application to spherical robots (such as BB-8 [1]).[7] By moving the robot around either a single prescribed rectangular path or a prescribed trio of rectangular paths any given orientation of the robot can be achieved. Furthermore, most spherical robots have a drive system which can produce fixed axis rotations (the mechanism in BB-8 provides an excellent example) so the rectangular paths discussed in this paper are feasible.

---

[7]Additional details on spherical robots can be found in the articles [15, 42].
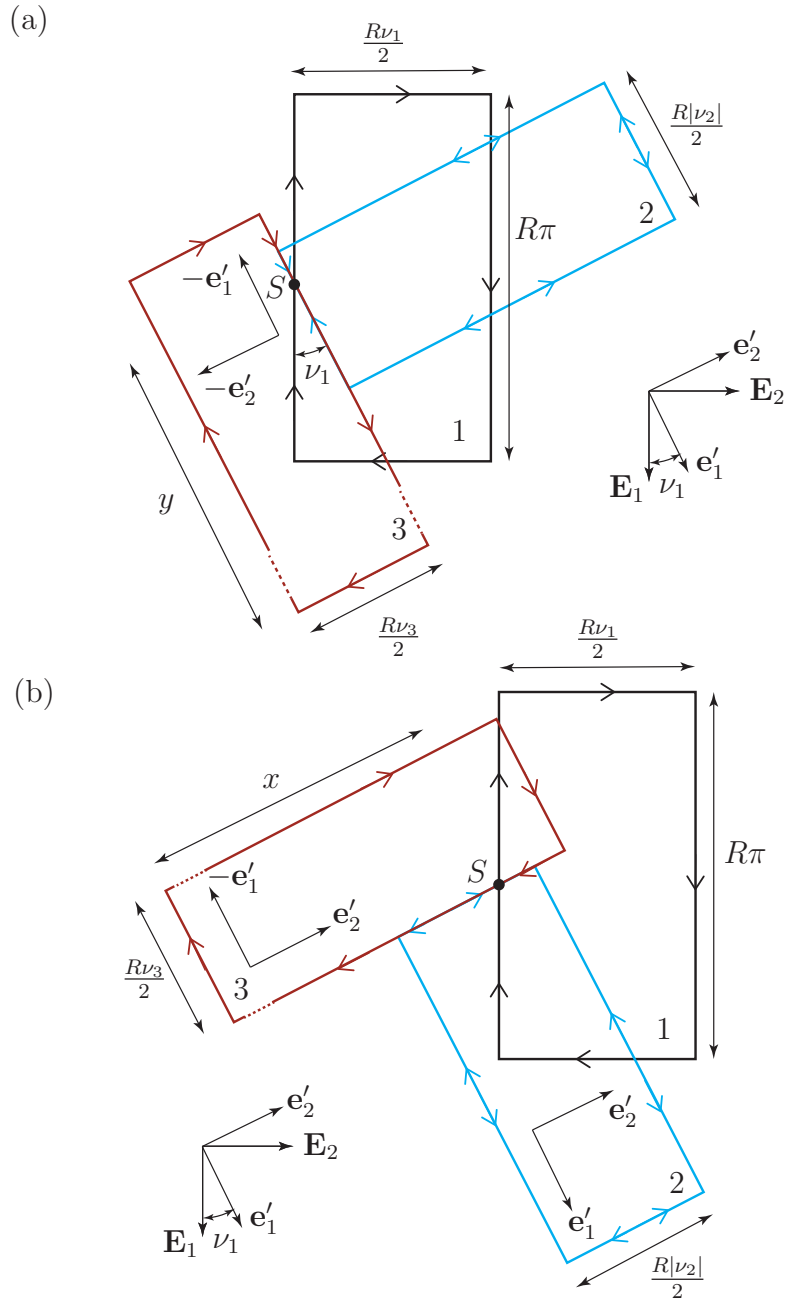
Figure 2.9: The three motions for the sets of (a) 3-2-1 Euler angles and (b) 3-1-2 Euler angles: ν_1, ν_2, and ν_3. The first rectangular path (labelled 1) has a base of length $\frac{R\nu_1}{2}$ and height $R\pi$. The second rectangular path (labelled 2) has base of length $R\pi$ and height $\frac{R|\nu_2|}{2}$. This path is circumnavigated in the clockwise direction if $\nu_2 < 0$ and in the counter clockwise direction if $\nu_2 > 0$. The figure illustrates the latter case. The third, and final rectangular path (labelled 3) has a base of length $\frac{R\nu_3}{2}$ and height $3R\pi$. For the 3-2-1 and 3-1-2 set of Euler angles, $\nu_2 \in \left[-\frac{\pi}{2}, \frac{\pi}{2}\right]$, $x = R\pi - R\nu_2$ and $y = 2R\pi - R\nu_2$.

Chapter 3

On the Dynamics of Transporting Rolling Cylinders

3.1 Introduction

A common, yet hazardous, method of transporting cylindrical tanks used to carry compressed gas involves rolling both tanks at opposite angles of inclination to the vertical (cf. Figure 3.1).[1] By propelling one of the tanks while maintaining point contact between the tanks, both tanks can be transported together with their centers of mass moving in straight lines. Apart from safety concerns, this mechanism for transporting tanks also raises questions about the dynamics of the cylinders involved. For instance, is there rolling or sliding contact at the point of contact between the cylinders and is it necessary to support the entire weight of both cylinders?

To explore the dynamics of the locomotion mechanism, we are able to leverage the wealth of research on rolling cylinders in the literature. Much of this work can be traced to seminal papers by Appell [2] and Korteweg [45] on the rolling disk in the early 1900s and the large numbers of recent papers (cf. e.g., [5, 8, 44, 71]) that were inspired by the paradoxical behavior of a cylinder of chrome plated cast iron known as Euler's Disk.

We start our analysis with a exploration of the problem of supporting an inclined cylinder that has a single point in contact with a rough surface and is supported by an applied force at the other end of the cylinder. As the contact condition is maintained by a static friction force, multiple equilibrium configurations and a range of applied forces are feasible. As an alternative to showing that the constraints on the rolling cylinder are non-integrable, we instead leverage the works of [12, 33, 38] and explore the holonomy of the rolling cylinder. With these two preliminary studies completed, we then turn to exploring the dynamics of a pair of cylinders in contact at a single point moving in unison on rough horizontal surface. With the help of Frobenius' theorem on integrability of a system of constraints [54, 62], we argue that the point contact is one of slipping. With the help of a recently developed

---

[1]A demonstrative example can be found here: https://youtu.be/Vgn5fv_LAk.
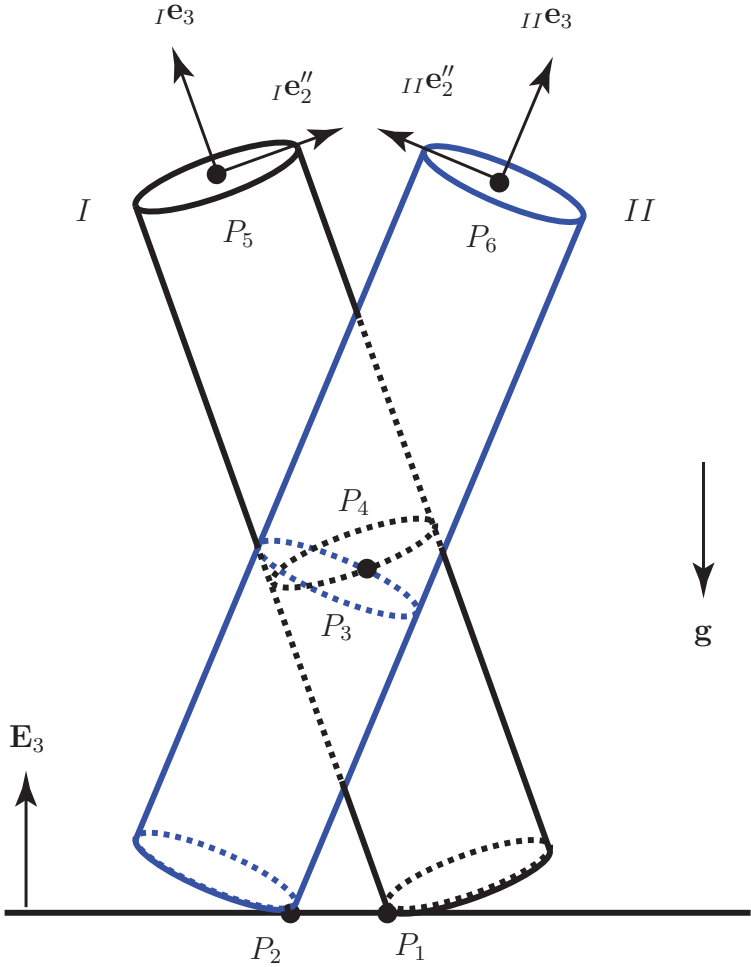
Figure 3.1: A pair of cylinders in motion on a horizontal surface. Each cylinder has a single point of contact with the surface and a single point of mutual contact.

numerical method by Capobianco et al. [14], a numerical simulation of the locomotion mechanism is then developed.

Supplemental material for this chapter can be found here:
https://github.com/ThH00/On-the-Dynamics-of-Transporting-Rolling-Cylinders

3.2 A Rolling Cylinder

We consider a homogeneous circular cylinder of mass m, height h, and radius R. The position vector of the center of mass $\bar{X}$ is denoted by $\bar{\mathbf{x}}$ and the position vector of the instantaneous

point of contact P is denoted by $\mathbf{x}_P$:

$$\bar{\mathbf{x}} = x_1 \mathbf{E}_1 + x_2 \mathbf{E}_2 + x_3 \mathbf{E}_3 \qquad (3.2.1)$$

where $\{\mathbf{e}_1, \mathbf{e}_2, \mathbf{e}_3\}$ is a right-handed set of Cartesian basis vectors for $\mathbb{E}^3$. The position vector of P relative to $\bar{X}$ is denoted by $\boldsymbol{\pi}_P$.

To parameterize the rotation tensor $\mathbf{Q}$ of the cylinder a set of 3-1-3 Euler angles, ψ, ϑ, and φ, are used. The angles define the orientation of a basis $\{\mathbf{e}_1, \mathbf{e}_2, \mathbf{e}_3\}$ that corotates with the cylinder with respect to the basis $\{\mathbf{E}_1, \mathbf{E}_2, \mathbf{E}_3\}$: $\mathbf{Q} = \mathbf{e}_1 \otimes \mathbf{E}_1 + \mathbf{e}_2 \otimes \mathbf{E}_2 + \mathbf{e}_3 \otimes \mathbf{E}_3$. Here, $\otimes$ is the tensor product of two vectors. While the first and third Euler angles range from 0 to 2π, the second Euler angle, $\vartheta \in (0, \pi)$ in order to avoid a coordinate singularity associated with the Euler angle parameterization of a rotation tensor [31]. Referring to Figure 3.2, we observe that ϑ is a measure of the inclination of the cylinder to the vertical: when $\vartheta = 0$, the cylinder is vertical and when $\vartheta = \frac{\pi}{2}$ the cylinder is horizontal. In both of these cases, the point contact assumption we employ fails. Consequently, for our analyses we assume $\vartheta \in \left(0, \frac{\pi}{2}\right)$ unless otherwise stated. For additional details on the 3-1-3 Euler angles, including a representation for the angular velocity vector $\boldsymbol{\omega}$, the reader is referred to Appendix A.

The constraints that the cylinder rolls without slipping on the horizontal surface can be expressed in terms of the velocity vector of the instantaneous point of contact: $\mathbf{v}_P = \mathbf{0}$. As $\mathbf{v}_P = \bar{\mathbf{v}} + \boldsymbol{\omega} \times \boldsymbol{\pi}_P$, the constraints can be expressed as

$$\Pi_1 = 0, \qquad \Pi_2 = 0, \qquad \Pi_3 = 0. \qquad (3.2.2)$$

That is,

$$\Pi_k = \bar{\mathbf{v}} \cdot \mathbf{E}_k + (\boldsymbol{\omega} \times \boldsymbol{\pi}_P) \cdot \mathbf{E}_k, \qquad (k = 1, 2, 3), \qquad (3.2.3)$$

where

$$\boldsymbol{\pi}_P = -\frac{h}{2}\mathbf{e}_3 - r\mathbf{e}_2'', \qquad (3.2.4)$$

and representations for $\mathbf{e}_2''$ and $\boldsymbol{\omega}$ can be found in (A.1.2), (A.1.3), and (A.2.1) in Appendix A. The constraints functions (3.2.2) can be expressed in their component forms:

$$\Pi_1 = \dot{x}_1 + f_1 \cos(\psi)\dot{\psi} - f_2 \sin(\psi)\dot{\vartheta} + r \cos(\psi)\dot{\varphi},$$
$$\Pi_2 = \dot{x}_2 + f_1 \sin(\psi)\dot{\psi} + f_2 \cos(\psi)\dot{\vartheta} + r \sin(\psi)\dot{\varphi},$$
$$\Pi_3 = \dot{x}_3 - f_1\dot{\vartheta}, \qquad (3.2.5)$$

where

$$f_1 = r \cos(\vartheta) - \frac{h}{2}\sin(\vartheta), \qquad f_2 = r \sin(\vartheta) + \frac{h}{2}\cos(\vartheta). \qquad (3.2.6)$$
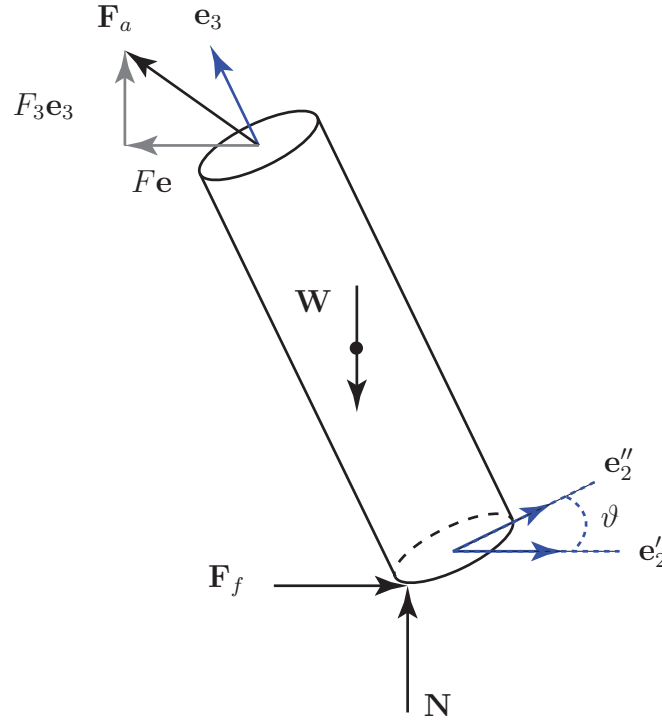
Figure 3.2: The forces acting on the cylinder are the weight $\mathbf{W} = -mg\mathbf{E}_3$ acting at its center of mass, the normal force $\mathbf{N} = N\mathbf{E}_3$ and the friction force $\mathbf{F}_f = F_{f_1}\mathbf{E}_1 + F_{f_2}\mathbf{E}_2$ acting at the contact between the cylinder and the ground, and an applied force $\mathbf{F}_a = F_1\mathbf{E}_1 + F_2\mathbf{E}_2 + F_3\mathbf{E}_3$ at mid point of the upper surface of the cylinder.

As discussed in Appendix D, the system of constraints (3.2.2) are non-integrable (or non-holonomic). In addition, the constraint $\Pi_3 = 0$ is integrable and implies that $x_3 = r\sin(\vartheta) + \frac{h}{2}\cos(\vartheta)$ modulo a constant.

Referring to Figure 3.2, the forces acting on the cylinder are a gravitational force $-mg\mathbf{E}_3$ acting at $\bar{X}$, a normal $N\mathbf{E}_3$ and static friction force $\mathbf{F}_f = F_{f_1}\mathbf{E}_1 + F_{f_2}\mathbf{E}_2$ acting at the instantaneous point of contact P, and an applied force $\mathbf{F}_a$ acting at a point X_a on the upper extremities of the cylinder: $\boldsymbol{\pi}_a = \frac{h}{2}\mathbf{e}_3$. The cylinder is assumed to be axisymmetric with an inertia tensor

$$\mathbf{J} = \lambda_t \left(\mathbf{e}_1 \otimes \mathbf{e}_1 + \mathbf{e}_2 \otimes \mathbf{e}_2\right) + \lambda_a \mathbf{e}_3 \otimes \mathbf{e}_3, \tag{3.2.7}$$

where λ_t and λ_a are moments of inertia. The balance laws for the cylinder are

$$\mathbf{F}_a + \mathbf{F}_f + (N - mg)\mathbf{E}_3 = m\dot{\mathbf{v}},$$
$$\boldsymbol{\pi}_a \times \mathbf{F}_a + \boldsymbol{\pi}_P \times (\mathbf{F}_f + N\mathbf{E}_3) = \mathbf{J}\dot{\boldsymbol{\omega}} + \boldsymbol{\omega} \times (\mathbf{J}\boldsymbol{\omega}), \tag{3.2.8}$$

where $\boldsymbol{\pi}_a = \frac{h}{2}\mathbf{e}_3$. These balance laws are supplemented by the constraints (3.2.2) to form a determinate system of equations to compute the motion of the cylinder and the normal and static friction forces.

3.3 Supporting Rectilinear Motions of a Cylinder

We start by considering the simplest possible locomotion for an inclined cylinder: rectilinear motion of the center of mass at constant speed. The goal of our analysis is to determine the applied force $\mathbf{F}_a$ required to sustain the motion. For the motion of interest, two of the Euler angles are constant and the spin rate $\dot{\varphi}$ is constant:

$$\dot{\psi} = 0, \qquad \dot{\vartheta} = 0, \qquad \dot{\varphi} = \omega_0. \tag{3.3.1}$$

The constraints (3.2.2) are satisfied provided

$$\bar{\mathbf{v}} = -r\omega_0 \mathbf{e}_1'. \tag{3.3.2}$$

The balances of linear and angular momenta (3.2.8) simplify dramatically:

$$F\mathbf{e} + F_3\mathbf{E}_3 + F_{f_1}\mathbf{E}_1 + F_{f_2}\mathbf{E}_2 + N\mathbf{E}_3 - mg\mathbf{E}_3 = \mathbf{0},$$
$$\left(-\frac{h}{2}\mathbf{e}_3 - r\mathbf{e}_2''\right) \times (N\mathbf{E}_3 - F\mathbf{e}) + \frac{h}{2}\mathbf{e}_3 \times (F\mathbf{e} + F_3\mathbf{E}_3) = \mathbf{0}, \tag{3.3.3}$$

where the unit vector $\mathbf{e} = \beta_1\mathbf{e}_1' + \beta_2\mathbf{e}_2'$. With the help of equation $(3.3.3)_1$, we conclude that

$$N + F_3 = mg,$$
$$F_{f_1}\mathbf{E}_1 + F_{f_2}\mathbf{E}_2 = -F\mathbf{e}. \tag{3.3.4}$$

After expressing the balance of angular momentum $(3.3.3)_2$ in components with respect to the $\{\mathbf{e}_1', \mathbf{e}_2', \mathbf{E}_3\}$ basis, we find that:

$$N\left(\frac{h}{2}\sin(\vartheta) - r\cos(\vartheta)\right) - \frac{hF_3}{2}\sin(\vartheta) - F\beta_2\left(r\sin(\vartheta) + h\cos(\vartheta)\right) = 0,$$
$$F\beta_1\left(r\sin(\vartheta) + h\cos(\vartheta)\right) = 0, \tag{3.3.5}$$
$$-F\beta_1\left(r\cos(\vartheta) - h\sin(\vartheta)\right) = 0.$$

We conclude from the component forms that $\beta_1 = 0$ and then set $\beta_2 = 1$. That is, the friction force serves solely to balance the horizontal component of the applied force: $\mathbf{F}_f = -F\mathbf{e}_2'$. Using $(3.3.4)_1$ to eliminate $F_3 = mg - N$, we find that the balance of angular momentum reduces to a single non-trivial equation:

$$N\left(r\cos(\vartheta) - h\sin(\vartheta)\right) + \frac{mgh}{2}\sin(\vartheta) = -F\left(r\sin(\vartheta) + h\cos(\vartheta)\right). \tag{3.3.6}$$

The friction force $\mathbf{F}_f$ is subject to the the static friction criterion: $\sqrt{F_{f1}^2 + F_{f2}^2} = |F| \leq \mu N$. We henceforth restrict attention to the extreme cases of maximum friction force $|F| = \mu N$:

$$\mu N \left(r \sin(\vartheta) + h \cos(\vartheta)\right) = \left| \frac{mgh}{2} \sin(\vartheta) + N \left(r \cos(\vartheta) - h \sin(\vartheta)\right) \right|. \tag{3.3.7}$$

This equality is equivalent to a pair of identities:

$$\frac{mg - F_3}{mg} = \frac{N}{mg} = \frac{\frac{1}{2} \sin(\vartheta)}{\sin(\vartheta) - \frac{r}{h} \cos(\vartheta) \pm \left(\frac{r\mu}{h} \sin(\vartheta) + \cos(\vartheta)\right)}. \tag{3.3.8}$$

The condition that $N > 0$ and $F_3 > 0$ are simultaneously satisfied implies that $0 < \frac{N}{mg} < 1$ and also places a restriction on the allowable range of the angle of inclination ϑ:

$$\vartheta \in \left(\min\left(0, \tan^{-1}\left(\frac{\frac{r}{h} - \mu}{\frac{1}{2} + \frac{r\mu}{h}}\right)\right), \frac{\pi}{2}\right) \qquad \text{in the } (+) \text{ case,}$$

$$\vartheta \in \left(\min\left(0, \cot^{-1}\left(\frac{\frac{1}{2} - \frac{r\mu}{h}}{\frac{r}{h} + \mu}\right)\right), \frac{\pi}{2}\right) \qquad \text{in the } (-) \text{ case.} \tag{3.3.9}$$

For a given inclination of the cylinder (i.e., a given value of ϑ), two limiting friction force distributions with distinct applied forces $\mathbf{F}_a$ are possible. At the transitional case where the horizontal plane is smooth ($\mu = 0$), (3.3.8) simplifies to

$$\frac{mg - F_3}{mg} = \frac{N}{mg} = \frac{\frac{1}{2} \sin(\vartheta)}{\sin(\vartheta) - \frac{r}{h} \cos(\vartheta)}, \qquad \vartheta \in \left(\tan^{-1}\left(\frac{2r}{h}\right), \frac{\pi}{2}\right). \tag{3.3.10}$$

To explore possible inclinations of the cylinder, we plot $\frac{mg}{N}$ as a function of the angle of inclination for three limiting cases: $\mathbf{F}_f = -\mu N \mathbf{e}_2'$, $\mathbf{F}_f = \mathbf{0}$, and $\mathbf{F}_f = \mu N \mathbf{e}_2'$. These cases are defined by (3.3.8)$_-$, (3.3.10), and (3.3.8)$_+$, respectively. The results are shown in Figures 3.3, fig:force-ratio-figs, and 3.5. From these figures we observe that not all possible combinations of F_3 and ϑ are possible because of the limiting value of the static friction force. The results shown in Figures 3.4 and 3.5 demonstrate how the range in feasible values of (ϑ, F_3) depends on the geometry of the cylinder and the static coefficient of friction.

Referring to Figure 3.4, we observe that the curves for the case $\mathbf{F}_f = \mu N \mathbf{e}_2'$ (i.e., (3.3.8)$_+$) intersect at a single point that is independent of $\frac{r}{h}$. We can compute the coordinates of this point from (3.3.8) by combining the $\frac{r}{h}$ terms and setting their coefficient to be zero:

$$\left(\vartheta = \tan^{-1}\left(\frac{1}{\mu}\right), \frac{N}{mg} = \frac{1}{2\left(1 + \mu^2\right)}\right). \tag{3.3.11}$$

We also note the points where $N = mg$ and $F_3 = 0$ at which the inclined cylinder is in equilibrium under the action of its weight, normal and friction forces, and an applied force that counterbalances the friction force: $\mathbf{F}_a = -\mathbf{F}_f$. As evidenced by the results shown in Figure 3.5, the larger μ then the larger the range of angles of inclination ϑ for a given F_3.
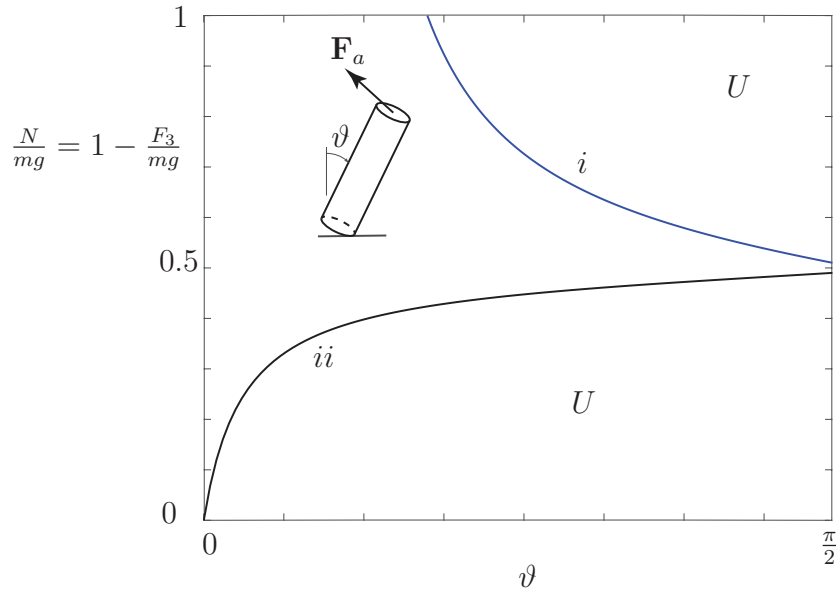
Figure 3.3: The space of possible configurations of the inclined rolling cylinder displayed as a function of the angle of inclination ϑ and the dimensionless force $\frac{N}{mg} = 1 - \frac{F_3}{mg}$. The bounding curves correspond to the restriction imposed by the static friction criterion. For the regions labeled U, the motions of interest are not possible. The curve labelled i is obtained from $(3.3.8)_+$ and the curve labelled ii is computed from $(3.3.8)_-$. The results shown in this figure pertain to the case where $\mu = 0.2$ and $\frac{r}{h} = 0.1$.

The Smallest Force

The results so far show that the same angle of inclination ϑ can be sustained by multiple values of the applied force $\mathbf{F}_a$. The multiplicity is made possible by the nature of the static friction force. It is of interest to see if there is a minimum force. More precisely, for given values of μ and $\frac{r}{h}$, what is the minimum force $\|\mathbf{F}_a\|$ required to maintain a given angle of inclination ϑ?

To answer the question, we return to (3.3.6) and eliminate N using the identity $N = mg - F_3$. After some rearranging, we find an expression for the dimensionless horizontal component of $\mathbf{F}_a$:

$$\frac{F}{mg} = \alpha_1 \left(\frac{F_3}{mg} \right) + \alpha_2, \tag{3.3.12}$$

where

$$\alpha_1 = \frac{\frac{r}{h}\cos(\vartheta) - \sin(\vartheta)}{\frac{r}{h}\sin(\vartheta) + \cos(\vartheta)}, \qquad \alpha_2 = -\frac{\frac{r}{h}\cos(\vartheta) - \frac{1}{2}\sin(\vartheta)}{\frac{r}{h}\sin(\vartheta) + \cos(\vartheta)}, \tag{3.3.13}$$

If we seek to compute the minimum applied force for a given ϑ, then a geometric argument applied to the linear relation (3.3.12) in the $F_3 - F$ space, shows that the point on the line
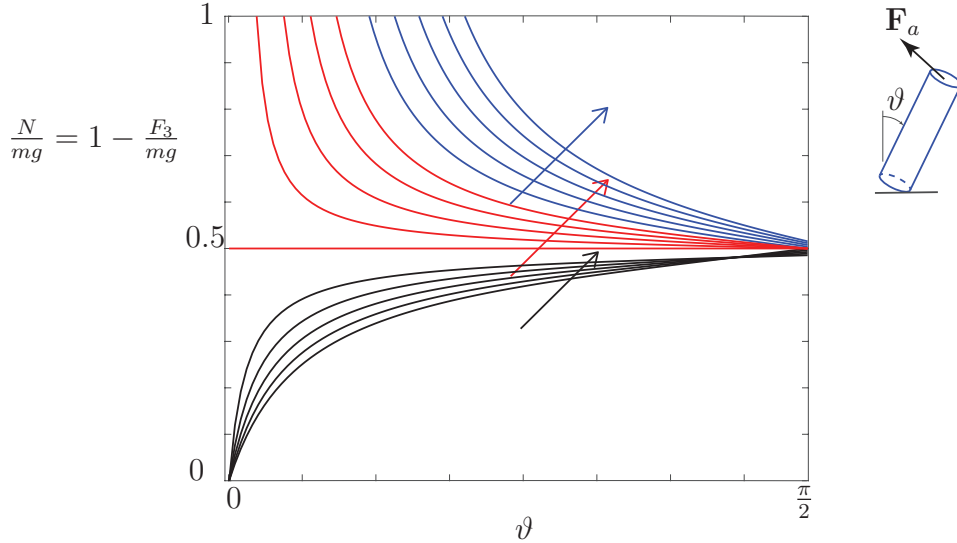
Figure 3.4: The dimensionless force $1 - \frac{F_3}{mg}$ as a function of the angle of inclination ϑ. The black curves are obtained from $(3.3.8)_+$, the red curves from $(3.3.10)$ (i.e., $(3.3.8)_{\mu=0}$), and the blue curves are obtained from $(3.3.8)_-$ for $\mu = 0.2$ and various values of $\frac{r}{h}$. The arrows point in direction of increasing $\frac{r}{h}$ from 0 to 0.15. When $\frac{r}{h} = 0$, the cylinder is a slender rod of length h while at the other extreme when $\frac{r}{h} = \infty$ the rigid body is circular disk of radius r.

$(3.3.12)$ closest to the origin is found by the intersection of this line with the perpendicular intercept:

$$\frac{F}{mg} = -\frac{1}{\alpha_1}\left(\frac{F_3}{mg}\right). \tag{3.3.14}$$

That is,

$$\left(\frac{F_3}{mg} = -\frac{\alpha_1\alpha_2}{1+\alpha_1^2}, \quad \frac{F}{mg} = \frac{\alpha_2}{1+\alpha_1^2}\right). \tag{3.3.15}$$

Thus, the minimum magnitude of the applied force for given values of $\frac{r}{h}$ and ϑ is

$$\|\mathbf{F}_a\| = \frac{mg|\alpha_2|}{\sqrt{1+\alpha_1^2}} = \frac{mg}{\sqrt{1+\left(\frac{r}{h}\right)^2}}\left|\frac{r}{h}\cos(\vartheta) - \frac{1}{2}\sin(\vartheta)\right|. \tag{3.3.16}$$

The solution $(3.3.15)$ to the minimum force problem is valid provided the static friction criterion, $|F| \le \mu N = \mu(mg - F_3)$, is satisfied:

$$|\alpha_2| \le \mu\left(\alpha_1^2 + \alpha_1\alpha_2 + 1\right). \tag{3.3.17}$$
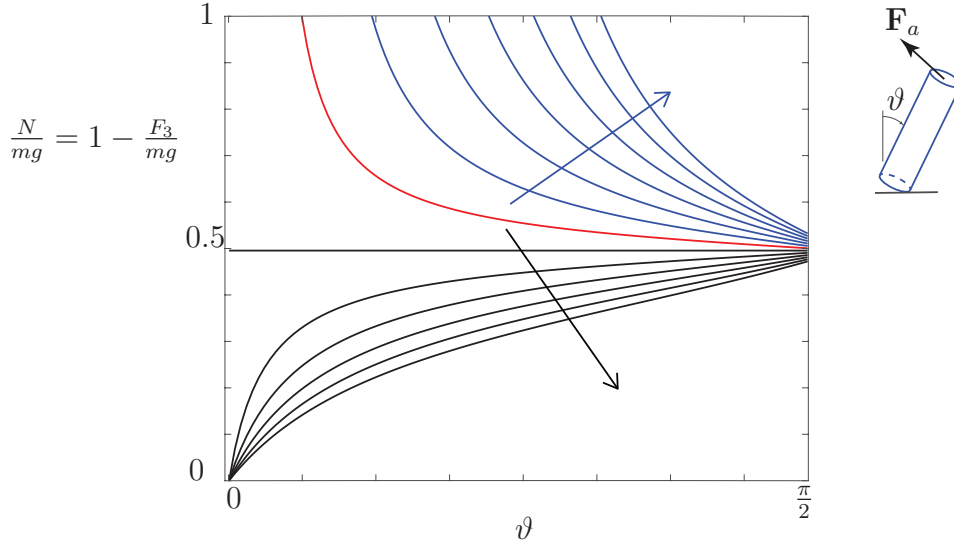
Figure 3.5: The dimensionless force $1 - \frac{F_3}{mg}$ as a function of the angle of inclination ϑ. The black curves are obtained from $(3.3.8)_+$, the red curves from $(3.3.10)$ (i.e., $(3.3.8)_{\mu=0}$), and the blue curves are obtained from $(3.3.8)_-$ for $\frac{r}{h} = 0.1$ and various values of $\mu = 0, 0.1, 0.2, 0.3, 0.4, 0.5, 0.6$. The arrows point in direction of increasing μ. The results for $\mu = 0$ coincide with the red curve.

A representative case, labeled i, where $(3.3.14)$ is used to compute the minimum applied force is shown in Figure 3.6.

If $(3.3.15)$ does not satisfy $(3.3.17)$, then the minimizing solution must be found by seeking the point on the line $(3.3.12)$ that is closest to the origin that satisfies $|F| \leq \mu N = \mu (mg - F_3)$. A representative case where $(3.3.15)$ does not yield a minimal applied force that satisfies the static friction condition $(3.3.17)$, is shown in Figure 3.6 where it is labeled ii. Consider the case where the point which minimizes the applied force $\mathbf{F}_a$ lies at the intersection of the line $(3.3.12)$ with $\mu N = \mu(mg - F_3) = F$ or $\mu N = \mu (mg - F_3) = -F$, depending on whichever minimizes that $\mathbf{F}_a$. This intersection points in the positive and negative cases are, respectively,

$$\left(\frac{F_3}{mg} = \frac{\mu - \alpha_2}{\mu + \alpha_1}, \quad \frac{F}{mg} = \mu \frac{\alpha_1 + \alpha_2}{\mu + \alpha_1} \right), \\ \left(\frac{F_3}{mg} = \frac{\mu + \alpha_2}{\mu - \alpha_1}, \quad \frac{F}{mg} = \mu \frac{\alpha_1 + \alpha_2}{\mu - \alpha_1} \right).$$

(3.3.18)

The third and penultimate case we need to consider arises when the line $(3.3.12)$ intersects the vertical axis $\frac{F_3}{mg} = 0$ and the restriction $F_3 \geq 0$ is imposed. In this case, the minimizing
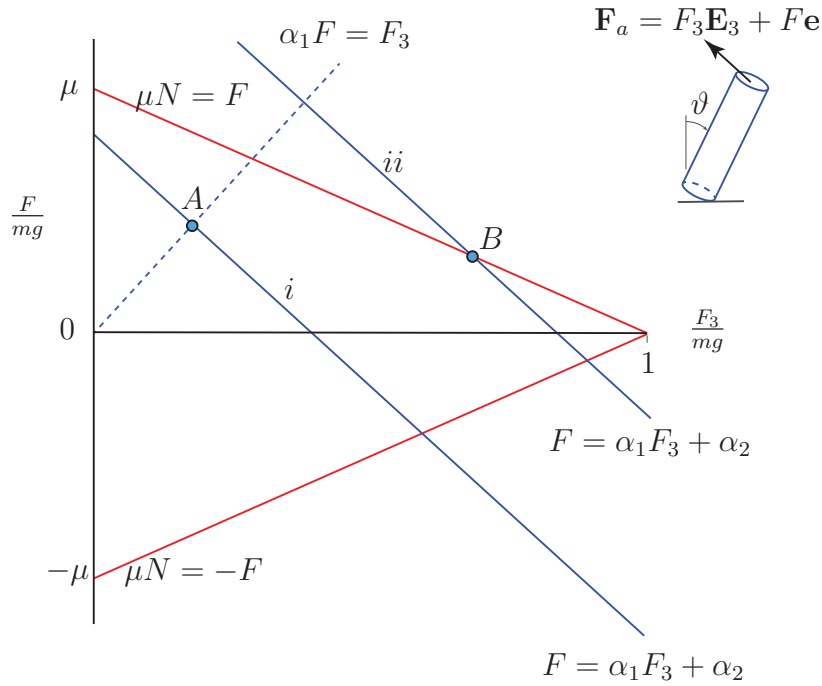
Figure 3.6: The space $\frac{F_3}{mg} - \frac{F}{mg}$ showing the admissible region defined by the static friction criterion $|F| \leq \mu N$ and two examples of the linear relation (3.3.12). For the example labelled i, the point corresponding to the minimum force $|\mathbf{F}_a|$ is labelled A and can be computed using (3.3.15). For the example labelled ii, the minimum force $|\mathbf{F}_a|$ computed using (3.3.15) does not satisfy the static friction criterion and the minimum force (labelled B) is computed using (3.3.18). The angle ϑ and parameters $\frac{r}{h}$ and μ are all assumed to be constant.

value of $||\mathbf{F}_a|| = mg\,|\alpha_2|$. The corresponding values of the components of $\mathbf{F}_a$ are

$$\left(\frac{F_3}{mg} = 0, \quad \frac{F}{mg} = \alpha_2 \right). \tag{3.3.19}$$

The fourth case arises when the cylinder is vertical ($\vartheta = 0$) or completely horizontal. In these cases, the normal force is balanced by gravity, the friction force vanishes, and the minimum $\mathbf{F}_a = \mathbf{0}$. In summary, four sets of values of $(F_3/mg, F/mg)$ are used to compute minimum values of $\|\mathbf{F}_a\|$ for $\vartheta \in [0, 90°]$.

As shown in Figure (3.7), we consider a fixed value of $\frac{r}{h} = 0.1$ and a fixed $\mu = 0.2$ and vary $\vartheta \in (0, 90°)$. With the help of (3.3.17) and (3.3.18), the locus of points $(F_3/mg, F/mg)$ corresponding to minimum values of $\|\mathbf{F}_a\|$ are computed. Referring to the figure, the points B and C correspond to the intersection points of the families of lines (3.3.12) and (3.3.14),
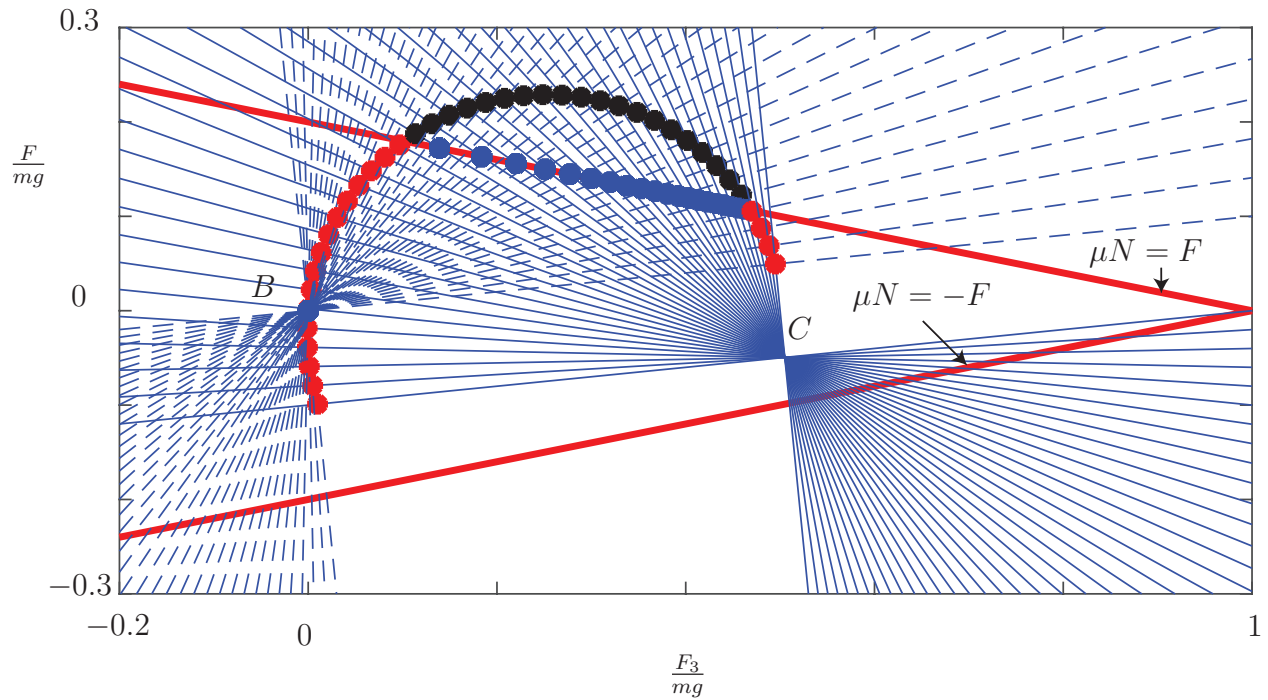
Figure 3.7: The components of the minimum force $\mathbf{F}_a$ in the $\frac{F_3}{mg} - \frac{F}{mg}$ plane trace a circle with diameter BC given by (3.3.20) for $\vartheta \in (0, 90°)$. The points belonging to the aforementioned circle for which (3.3.17) is satisfied are drawn in red, otherwise, they are drawn in black. In the latter case, the force minimizing points that satisfy the static friction criterion are drawn in blue, and belong either to the lines $\mu N = \pm F$ or $F_3 = 0$.

respectively, for a given $\frac{r}{h}$ value. The coordinates of these points

$$
\begin{aligned}
B &= \left(\frac{F_3}{mg} = 0, \quad \frac{F}{mg} = 0 \right), \\
C &= \left(\frac{F_3}{mg} = \frac{\frac{1}{2} + \left(\frac{r}{h} \right)^2}{1 + \left(\frac{r}{h} \right)^2}, \quad \frac{F}{mg} = \frac{-\frac{1}{2}\frac{r}{h}}{1 + \left(\frac{r}{h} \right)^2} \right).
\end{aligned}
\tag{3.3.20}
$$

Since the lines (3.3.12) and (3.3.14) always pass through the points B and C respectively, and are perpendicular. Thus, the locus of the intersection point of these lines is a circle of diameter BC.

For a given cylinder and contacting plane, the components of the minimum applied force as a function of ϑ are shown in Figure 3.8. The point labelled D corresponds to the absolute minimum applied force which is $\|\mathbf{F}_a\| = 0$ which arises when the angle of inclination $\vartheta = \tan^{-1}\left(\frac{2r}{h} \right)$. The cylinder self balances at this angle of inclination and the static friction force vanishes. The graphs of $\|\mathbf{F}_a\|(\vartheta)$, $F(\vartheta)$, and $F_3(\vartheta)$ are discontinuous at $\vartheta = 0, 90°$ as
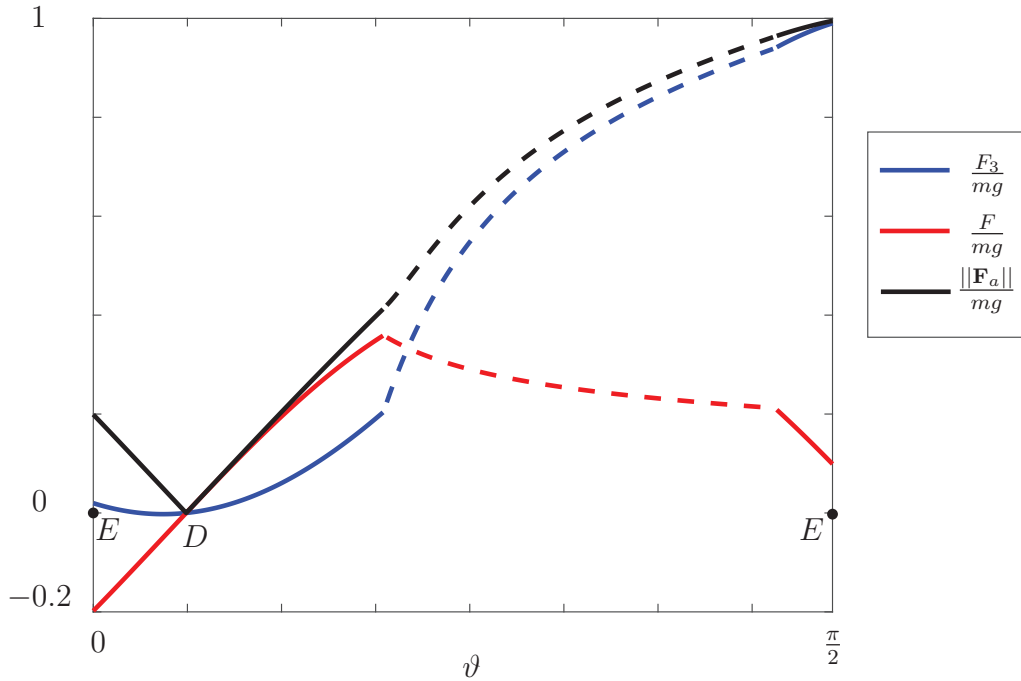
Figure 3.8: The minimum force satisfying the static friction criterion vs. ϑ for $\mu = 0.2$ and $\frac{r}{h} = 0.1$. The continuous portion of the curve corresponds to solutions of (3.3.15) satisfying (3.3.17). In the regions where (3.3.17) is not satisfied, the curve is dashed with relevant values given either by (3.3.18) or (3.3.19). The points labeled E correspond to the minimum values of $\mathbf{F}_a = \mathbf{0}$ when $\vartheta = 0, 90°$.

the minimum applied force $\mathbf{F}_a = \mathbf{0}$ at these points. The two points are labelled E in Figure 3.8 and signify discontinuities in the graphs of $F(\vartheta)$ and $F_3(\vartheta)$ as $\vartheta \searrow 0$ and $\vartheta \nearrow \frac{\pi}{2}$.

3.4 Holonomies of a Rolling Cylinder

Consider a cylinder rolling on a horizontal surface while its center of mass traces out a closed path. After the center of mass has returned to its original location, we will typically find that the orientation of the cylinder has changed. The change in orientation is known as a holonomy. Holonomies in rigid body dynamics can be attributed to the non-holonomic constraints on the motion of the body. The phenomenon in rolling spheres with application to spherical robots has been discussed in [12, 33, 38] and discussions of holonomy in parallel parking can be found in [13, 52].

Recall that we are using a set of 3-1-3 Euler angles to parameterize the rotation of the cylinder. The angles $\psi \in [0, 2\pi]$ and $\vartheta = [0, \pi]$ can each be individually altered without changing the other angles or the location of the instantaneous point of contact P. As

a result, and in contrast to our earlier work on the holonomy of rolling spheres [33], we restrict attention to motions of the cylinder that produce changes in φ. The two motions of interest are those where the instantaneous point of contact traces out a rectangular path and a circular path. We now establish closed form expressions for the change in orientation (holonomy) for both types of path.

(a) (b)
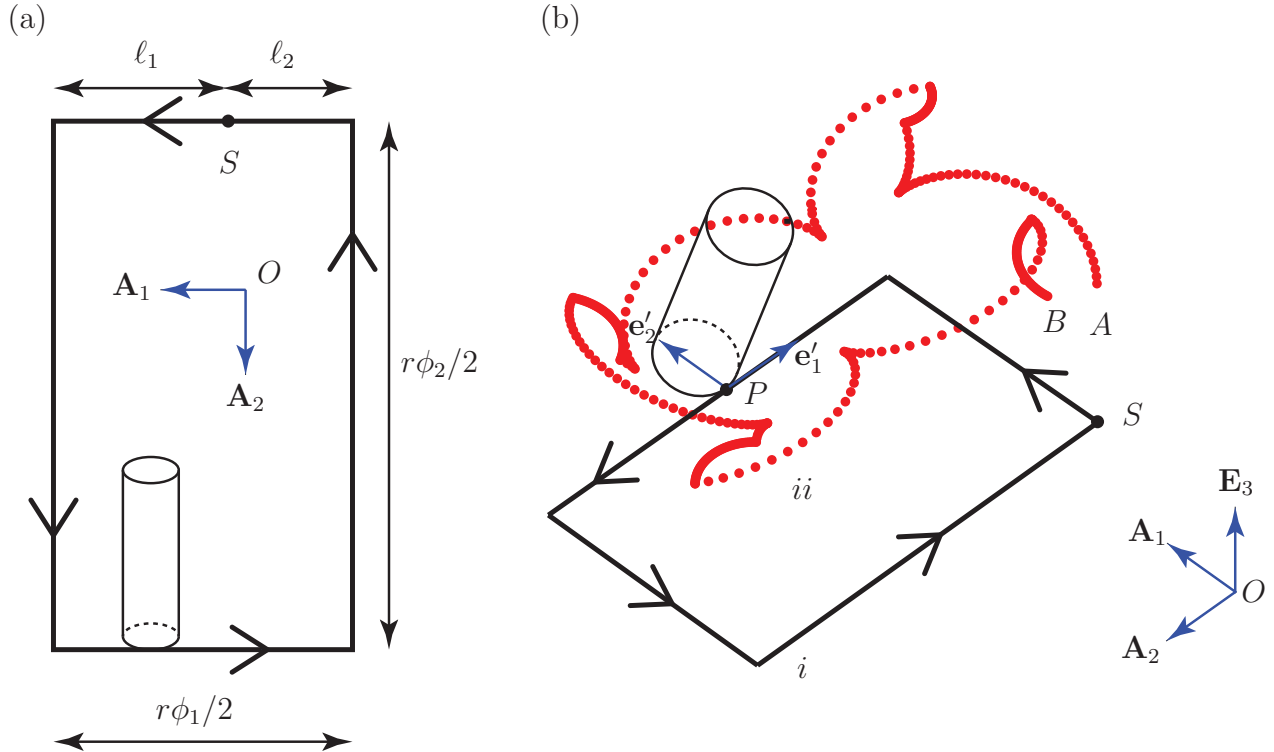
Figure 3.9: (a) The rectangular path traced by the instantaneous point of contact P between the cylinder and the horizontal plane. The cylinder starts the circumnavigation at the point labeled S. The location of S is defined by the parameter $s \in [0,1]$: $\ell_1 = \frac{r(1-s)\phi_1}{2}$ and $\ell_2 = \frac{rs\phi_1}{2}$. The rectangle has sides of length $\frac{r\phi_1}{2}$ and $\frac{r\phi_2}{2}$ and produces a holonomy of $\phi_1 + \phi_2$ in the rolling inclined cylinder. (b) Time traces of the point P and of a material point X on the rim of the cylinder as P traces the rectangular path. The traces are labelled i and ii respectively. While the center of mass returns to its original location S, X has relocated from A to B. The example shown is classified as Case I.

Holonomy of a Rolling Cylinder Tracing a Rectangular Path

If we imagine an rolling inclined cylinder tracing a closed rectangular path starting at a point S, then the change in the angle φ when the center of mass has returned to its original location will typically be non-trivial. The change in the angle φ is an example of a holonomy. As we

shall explain, the change in the angle is not only a function of the lengths of the sides of the rectangles, whether or not the path is traversed in a counterclockwise or clockwise manner, the angle ϑ of inclination of the rectangle, and whether the unit vector $\mathbf{e}_2'$ points inward or outward to the path. We refer to these two instances as Case I and Case II, respectively. The holonomy will be shown to be independent of the choice of starting point S.

To proceed with our analysis, we consider Case I. Now consider a rectangle with side lengths $\frac{r\phi_1}{2}$ and $\frac{r\phi_2}{2}$ as depicted in Figure 3.9. Without loss in generality, the starting point S is specified by the parameter $s \in [0, 1]$. The Cartesian basis vectors $\mathbf{A}_1$ and $\mathbf{A}_2$ are each parallel to two sides of the rectangle. Tracing a rectangular path in a counterclockwise manner using a rolling cylinder is achieved using two types of motion: rotations about $\mathbf{e}_3$ and rotations about $\mathbf{E}_3$. For the first of these, $\boldsymbol{\omega} = \dot{\varphi}\mathbf{e}_3$, and the constraints $\mathbf{v}_P = \mathbf{0}$ imply that

$$\bar{\mathbf{v}} = -r\dot{\varphi}\mathbf{e}_1'. \tag{3.4.1}$$

That is the cylinder's center of mass moves in a straight line. As $\dot{\varphi}_1 > 0$, this implies that $\mathbf{e}_1'$ is antiparallel to the direction of motion and $\mathbf{e}_2'$ is one of the two outward normals to the path. For motions where $\boldsymbol{\omega} = \dot{\psi}\mathbf{E}_3$, the constraints $\mathbf{v}_P = \mathbf{0}$ implies that

$$\bar{\mathbf{v}} = -\dot{\psi}f_1\mathbf{e}_1'. \tag{3.4.2}$$

These motions enable the cylinder to turn the corners of the rectangle. For the rectangular path shown in Figure 3.9, either $\mathbf{e}_1' = \pm\mathbf{A}_1$ or $\mathbf{e}_1' = \pm\mathbf{A}_2$.

Tracing the rectangle depicted in Figure 3.9(a) in a counterclockwise direction requires the cylinder to undergo a sequence of nine rotations. The combined rotation, which is also the change in orientation of the cylinder, is $\mathbf{S}$ where

$$\begin{aligned}
\mathbf{S} &= \hat{\mathbf{S}}_I\left(\vartheta, \phi_1, \phi_2, s, r, h, \psi_0, \circlearrowleft\right) \\
&= \mathbf{A}\left(\frac{s\phi_1}{2}, {}_0\mathbf{e}_3\right) \mathbf{A}\left(\frac{\pi}{2}, \mathbf{E}_3\right) \mathbf{A}\left(\frac{\phi_2}{2}, {}_3\mathbf{e}_3\right) \mathbf{A}\left(\frac{\pi}{2}, \mathbf{E}_3\right) \mathbf{A}\left(\frac{\phi_1}{2}, {}_2\mathbf{e}_3\right) \\
&\quad \times \mathbf{A}\left(\frac{\pi}{2}, \mathbf{E}_3\right) \mathbf{A}\left(\frac{\phi_2}{2}, {}_1\mathbf{e}_3\right) \mathbf{A}\left(\frac{\pi}{2}, \mathbf{E}_3\right) \mathbf{A}\left(\frac{(1-s)\phi_1}{2}, {}_0\mathbf{e}_3\right)
\end{aligned} \tag{3.4.3}$$

where $\mathbf{A}(\xi, \mathbf{r})$ denotes a rotation about an axis $\mathbf{r}$ through a counterclockwise angle of rotation ξ,

$$_i\mathbf{e}_3 = \mathbf{A}\left(\frac{i\pi}{2}, \mathbf{E}_3\right) {}_0\mathbf{e}_3, \qquad (i = 1, 2, 3),$$

$$_0\mathbf{e}_3 = \sin(\psi_0)\sin(\vartheta)\mathbf{E}_1 - \cos(\psi_0)\sin(\vartheta)\mathbf{E}_2 + \cos(\vartheta)\mathbf{E}_3. \tag{3.4.4}$$

The parameter $\circlearrowright, \circlearrowleft$ in $\hat{\mathbf{S}}$ is used to distinguish counterclockwise and clockwise directions, respectively, of circumnavigating the rectangular path. Computing the products of the rotations in (3.4.3), we conclude that

$$\hat{\mathbf{S}}_I\left(\vartheta, \phi_1, \phi_2, s, r, h, \psi_0, \circlearrowleft\right) = \mathbf{A}\left(\phi_1 + \phi_2, {}_0\mathbf{e}_3\right). \tag{3.4.5}$$

That is, the holonomy is

$$\Delta\varphi = \phi_1 + \phi_2. \tag{3.4.6}$$

We observe that $\mathbf{A}\left(2n\pi, {}_0\mathbf{e}_3\right) = \mathbf{I}$, where $\mathbf{I}$ is the identity tensor. Thus, we can increase the lengths of the sides of the rectangle by integer multiples of 2π without changing the holonomy $\Delta\varphi$. If we were to traverse the rectangle in a clockwise manner, then the sign of the holonomy reverses:

$$\hat{\mathbf{S}}_I\left(\vartheta, \phi_1, \phi_2, s, r, h, \psi_0, \circlearrowright\right) = \mathbf{A}\left(-\phi_1 - \phi_2, {}_0\mathbf{e}_3\right). \tag{3.4.7}$$

That is, $\Delta\varphi = -\phi_1 - \phi_2$.

For Case II, the expression (3.4.1) for $\bar{\mathbf{v}}$ holds, however $\dot\varphi < 0$. Assuming the path is circumnavigated in a counterclockwise manner, the unit vector $\mathbf{e}_2'$ now points inwards. The expression for $\hat{\mathbf{S}}_{II}$ is readily established by changing the signs of ϕ_1 and ϕ_2 in (3.4.3). The resulting holonomies are

$$\hat{\mathbf{S}}_{II}\left(\vartheta, \phi_1, \phi_2, s, r, h, \psi_0, \circlearrowright\right) = \mathbf{A}\left(-\phi_1 - \phi_2, {}_0\mathbf{e}_3\right),$$
$$\hat{\mathbf{S}}_{II}\left(\vartheta, \phi_1, \phi_2, s, r, h, \psi_0, \circlearrowleft\right) = \mathbf{A}\left(\phi_1 + \phi_2, {}_0\mathbf{e}_3\right). \tag{3.4.8}$$

As the expressions for the angle and axes of the holonomies are independent of s, we conclude that the holonomies (3.4.6), (3.4.7), and (3.4.8) are independent of the starting point S. Representative examples of Case I and Case II are shown in Figure 3.10.

We can also verify (3.4.6) and (3.4.8) using a quaternion representation of a rotation and the Rodrigues formula for compound rotations.[2] Restricting attention to Case I, repeated application of the Rodrigues formula to (3.4.3) shows that the unit quaternion associated with the rotation $\hat{\mathbf{S}}_I\left(\vartheta, \phi_1, \phi_2, s, r, h, \psi_0, \circlearrowleft\right)$ has the representation

$$q_0 = \cos\left(\frac{\gamma}{2}\right) = \cos\left(\pi + \frac{\phi_1}{2} + \frac{\phi_2}{2}\right),$$
$$\mathbf{q} = \sin\left(\frac{\gamma}{2}\right)\mathbf{r} = \sin\left(\pi + \frac{\phi_1}{2} + \frac{\phi_2}{2}\right){}_0\mathbf{e}_3, \tag{3.4.9}$$

where γ is the angle of rotation and $\mathbf{r}$ is the axis of rotation: a result that is in agreement with (3.4.6). The analysis for Case II is similar and in the interests of brevity is not presented here.

---

[2]Consider a pair of rotations $\mathbf{A} = \tilde{\mathbf{A}}\left(a_0, \mathbf{a}\right)$ and $\mathbf{B} = \tilde{B}\left(b_0, \mathbf{b}\right)$ parameterized by unit quaternions $\left(a_0, \mathbf{a}\right)$ and $\left(b_0, \mathbf{b}\right)$, respectively. Then, the compound rotation $\mathbf{C} = \mathbf{B}\mathbf{A}$ is parameterized by the unit quaternion

$$c_0 = a_0 b_0 - \mathbf{a}\cdot\mathbf{b},$$
$$\mathbf{c} = a_0\mathbf{b} + b_0\mathbf{a} + \mathbf{b}\times\mathbf{a}.$$

(a)

(b)
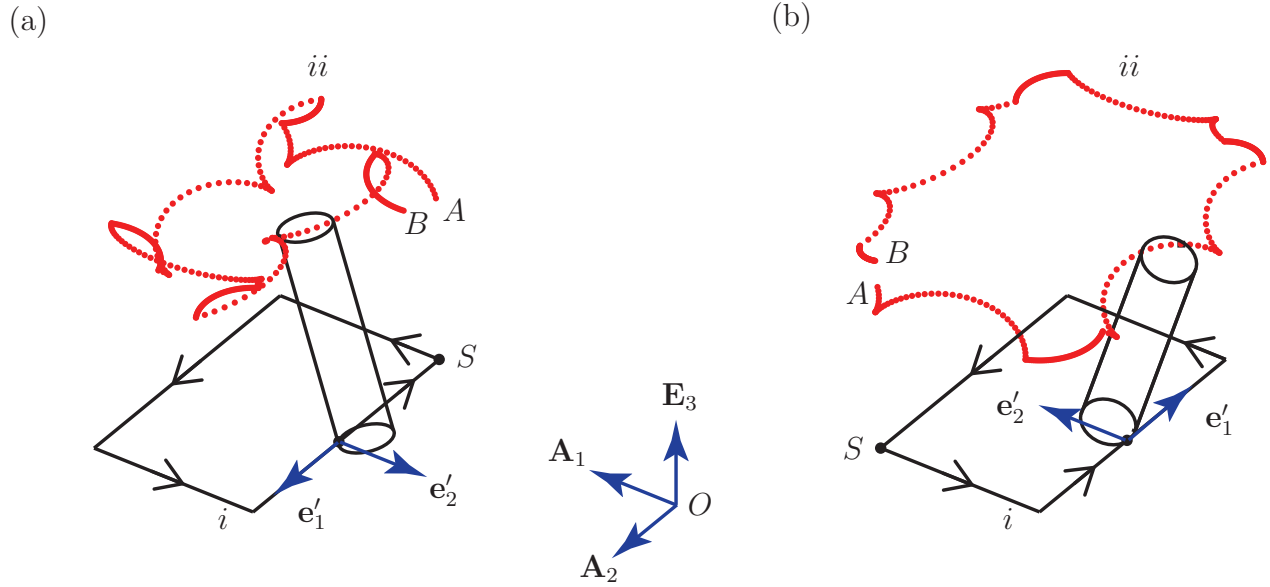
Figure 3.10: Motions of a cylinder where the center of mass traces a rectangular path in a counterclockwise manner and produces a holonomy: (a) Case I where $\Delta\varphi = 36.3901^o$ and (b) Case II where $\Delta\varphi = -36.3901^o$. For the results shown in this figure, $h = 8.3333r$, $\phi_1 = \frac{13\pi}{3}$, $\phi_2 = \frac{29\pi}{4}$, $\vartheta = \frac{\pi}{10}$, and $s = 0$.

Holonomy of a Rolling Cylinder Tracing a Circle

We now turn to the case where the center of mass of the cylinder traces a circular path. We are able to establish a simple expression (3.4.16) for the radius ℓ of the path of the instantaneous point of contact P to establish any desired relative change in the Euler angle φ of the cylinder. As with the case of a rectangular path and as illustrated in Figure 3.11, there are two cases to consider: Case I where $\mathbf{e}_2'$ points radially outward and Case II where $\mathbf{e}_2'$ points radially inwards.

For the motion of interest, ϑ is constant, $\boldsymbol{\omega} = \dot{\psi}_0 \mathbf{E}_3 + \dot{\varphi}_0 \mathbf{e}_3$, and $\dot{\psi}_0$ and $\dot{\varphi}_0$ are constant. The constraints (3.2.2) imply that

$$\bar{\mathbf{v}} = v_0 \mathbf{e}_1' \tag{3.4.10}$$

where

$$\mathbf{e}_1' = \cos\left(\psi\right)\mathbf{E}_1 + \sin\left(\psi\right)\mathbf{E}_2, \qquad v_0 = -f_1\dot{\psi}_0 - r\dot{\varphi}_0. \tag{3.4.11}$$

For a motion to be possible with $\dot{\psi}_0 \neq 0$ and $\dot{\varphi} \neq 0$, the center of mass traces a circle in a counterclockwise manner: that is, the orbital speed $\dot{\psi}_0 > 0$. If we let k be the radius of the
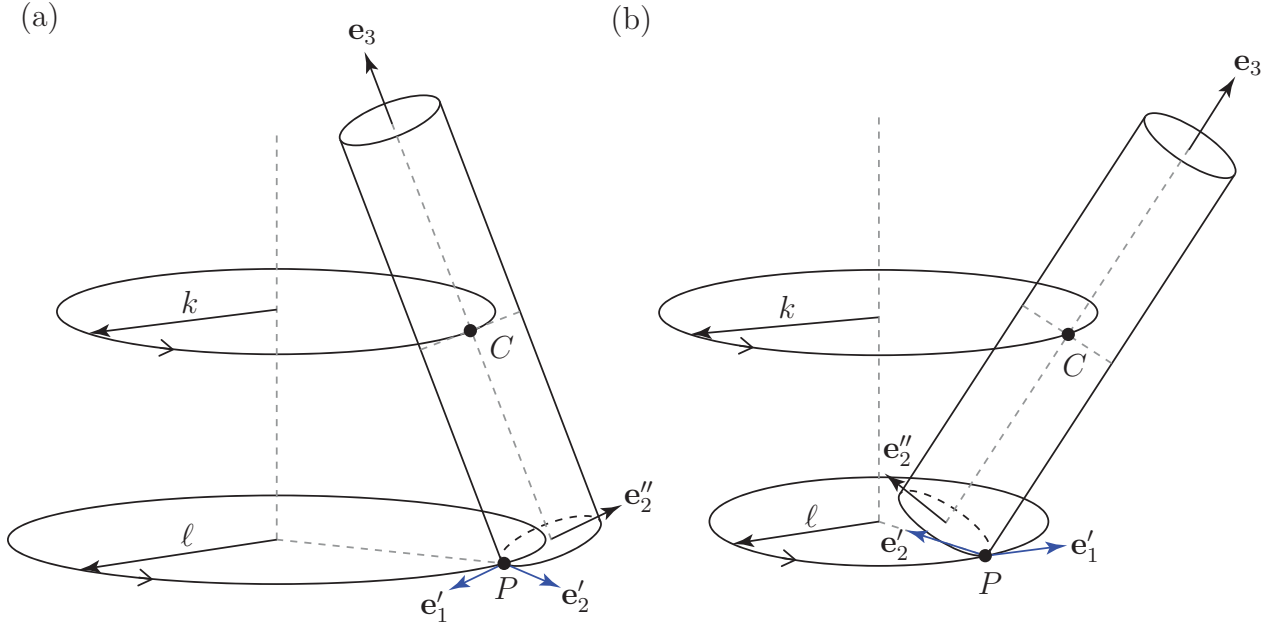
Figure 3.11: Motions of a cylinder where the center of mass C traces a circular path of radius k and the instantaneous point of contact P traces a circular path of radius ℓ. Both paths are traced in a counterclockwise manner. (a) Case I where $\mathbf{e}_2'$ points radially outward and (b) Case II where $\mathbf{e}_2'$ points radially inward.

circular path traced by the center of mass, then

$$\begin{cases} \bar{\mathbf{r}} = k\mathbf{e}_2', & \bar{\mathbf{v}} = -k\dot{\psi}_0\mathbf{e}_1' & \text{for Case I,} \\ \bar{\mathbf{r}} = -k\mathbf{e}_2', & \bar{\mathbf{v}} = k\dot{\psi}_0\mathbf{e}_1' & \text{for Case II.} \end{cases} \tag{3.4.12}$$

Combining the previous results, we obtain

$$\begin{cases} \left(\frac{h}{2}\sin(\vartheta) - r\cos(\vartheta)\right)\dot{\psi}_0 - r\dot{\varphi}_0 = -k\dot{\psi}_0 & \text{for Case I,} \\ \left(\frac{h}{2}\sin(\vartheta) - r\cos(\vartheta)\right)\dot{\psi}_0 - r\dot{\varphi}_0 = k\dot{\psi}_0 & \text{for Case II.} \end{cases} \tag{3.4.13}$$

That is,

$$\begin{cases} k = -\frac{h}{2}\sin(\vartheta) + r\cos(\vartheta) + \frac{r\dot{\varphi}_0}{\dot{\psi}_0} & \text{for Case I,} \\ k = \frac{h}{2}\sin(\vartheta) - r\cos(\vartheta) - \frac{r\dot{\varphi}_0}{\dot{\psi}_0} & \text{for Case II.} \end{cases} \tag{3.4.14}$$

If the center of mass traces a circle of radius k in a counterclockwise direction while ϑ is constant, then as $\boldsymbol{\pi}_P \cdot \mathbf{e}_1' = 0$ and $\boldsymbol{\pi}_P \cdot \mathbf{e}_2' = \frac{h}{2}\sin(\vartheta) - r\cos(\vartheta)$, we find that the instantaneous point of contact P traces a circle of radius ℓ such that

$$\begin{cases} \ell - k = \frac{h}{2}\sin(\vartheta) - r\cos(\vartheta) & \text{for Case I,} \\ \ell - k = r\cos(\vartheta) - \frac{h}{2}\sin(\vartheta) & \text{for Case II.} \end{cases} \tag{3.4.15}$$

To trace a complete circle, we require $\Delta\psi = 2\pi$. We conclude that

$$\begin{cases} \Delta\varphi = \frac{2\pi\ell}{r} & \text{for Case I,} \\ \Delta\varphi = -\frac{2\pi\ell}{r} & \text{for Case II.} \end{cases} \qquad (3.4.16)$$

We can adjust the radius ℓ of the circular path traced by P to obtain any desired rotation $\Delta\varphi$. Representative examples for the two cases are shown in Figure 3.12. If the circular path is traversed in a clockwise manner, then there will be sign changes to the results for $\Delta\varphi$ in (3.4.16).
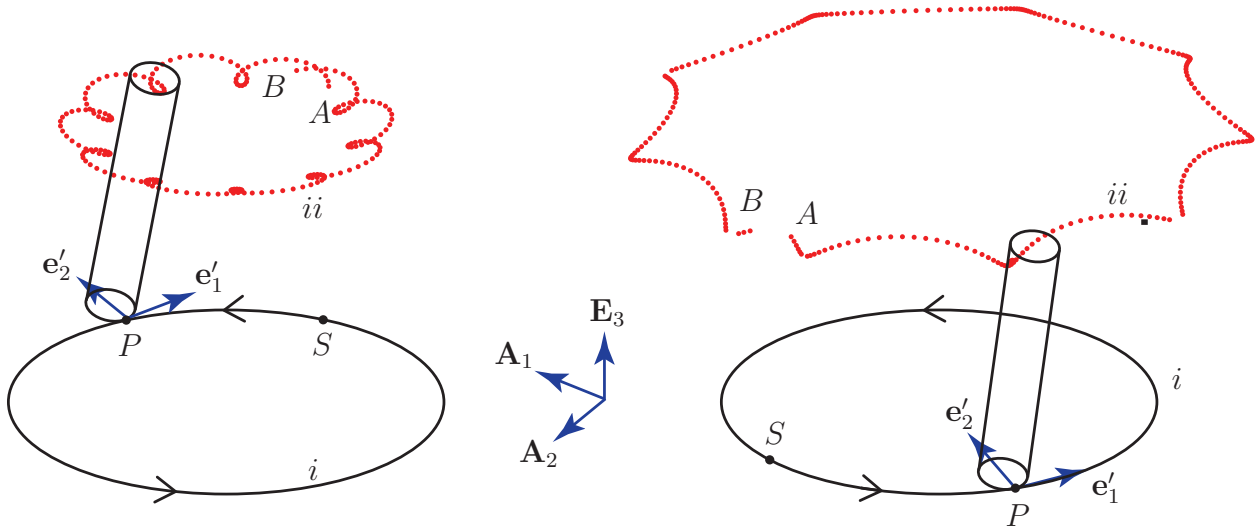
Figure 3.12: Time traces of the point P and of a material point X on the rim of the cylinder as P traces the circular path. The traces are labelled i and ii respectively. While the center of mass returns to its original location S, X has relocated from A to B. The radius of the path traced by P is ℓ (cf. (3.4.14) and (3.4.15)). For the results shown in these images, $\ell = 9.44233r$, $\vartheta = \frac{\pi}{10}$, and $h = 13.3333r$: (a) Case I where $\bar{\mathbf{r}} = 8.33r\mathbf{e}_2'$ and $\Delta\varphi = 59.3283^o$ and (b) Case II where $\bar{\mathbf{r}} = -10.5515r\mathbf{e}_2'$ and $\Delta\varphi = -59.3283^o$.

3.5   Kinematics of a Pair of Contacting Cylinders

Referring to Figure 3.1, consider a pair of cylinders are each in motion with a single point of instantaneous contact with a horizontal surface. The sides of the cylinders touch each other at a single point and the top of each cylinder is supported by applied forces and moments. The system of two rigid bodies has a total of eight possible permutations of slipping and rolling contacts at the three contact points. For present purposes, we are interested in examining the set of constraints where one cylinder is spun about its axis while both cylinders are constrained so that their points of contact trace straight parallel lines on the ground.

As shown in Figures 3.1 and 3.13, we identify the individual cylinders using the indices $I, 1$ and $II, 2$, respectively. The position vector $\bar{\mathbf{x}}_{I,II}$ of the center of mass $\bar{X}_{I,II}$ of the respective cylinders are parameterised by Cartesian coordinates:

$$
\begin{aligned}
\bar{\mathbf{x}}_I &= x_{I_1}\,\mathbf{E}_1 + x_{I_2}\,\mathbf{E}_2 + x_{I_3}\,\mathbf{E}_3, \\
\bar{\mathbf{x}}_{II} &= x_{II_1}\,\mathbf{E}_1 + x_{II_2}\,\mathbf{E}_2 + x_{II_3}\,\mathbf{E}_3.
\end{aligned}
\tag{3.5.1}
$$

Following works on the dynamics of rolling disks and cylinders (cf. [44, 56]), it is convenient to use a pair of sets of 3-1-3 Euler angles to parameterize the rotation of the cylinders.[3] Thus, the rotation tensor $\mathbf{Q}$ and associated angular velocity vectors $\boldsymbol{\omega}$ of the rigid bodies have the following representations:

$$
\begin{aligned}
\mathbf{Q}_I &= \mathbf{Q}_I\left(\psi_1, \vartheta_1, \varphi_1\right), & \boldsymbol{\omega}_I &= \dot{\psi}_1\,\mathbf{E}_3 + \dot{\vartheta}_1\,_I\mathbf{e}_1'' + \dot{\varphi}_1\,_I\mathbf{e}_3, \\
\mathbf{Q}_{II} &= \mathbf{Q}_{II}\left(\psi_2, \vartheta_2, \varphi_2\right), & \boldsymbol{\omega}_{II} &= \dot{\psi}_2\,\mathbf{E}_3 + \dot{\vartheta}_2\,_{II}\mathbf{e}_1'' + \dot{\varphi}_2\,_{II}\mathbf{e}_3.
\end{aligned}
\tag{3.5.2}
$$

The bases $\{\mathbf{E}_3, {}_I\mathbf{e}_1'', {}_I\mathbf{e}_3\}$ and $\{\mathbf{E}_3, {}_{II}\mathbf{e}_1'', {}_{II}\mathbf{e}_3\}$ are the Euler bases associated with the respective sets of Euler angles.

Formulating Contact Constraints

The constraints that cylinder I of height h_1 and radius r_1 rolls without slipping on the horizontal surface can be represented as:

$$
\mathbf{v}_1 = \bar{\mathbf{v}}_I + \boldsymbol{\omega}_I \times \boldsymbol{\pi}_{P_1} = \mathbf{0}.
\tag{3.5.3}
$$

The position of the instantaneous point of contact P_1 relative to the center of mass has the following representation:

$$
\boldsymbol{\pi}_{P_1} = -\frac{h_1}{2}\,{}_I\mathbf{e}_3 - r_1\,{}_I\mathbf{e}_2''.
\tag{3.5.4}
$$

In an identical manner, the constraints that cylinder II of height h_2 and radius r_2 rolls without slipping on the horizontal surface have several representations:

$$
\mathbf{v}_2 = \bar{\mathbf{v}}_{II} + \boldsymbol{\omega}_{II} \times \boldsymbol{\pi}_{P_2} = \mathbf{0},
\tag{3.5.5}
$$

where

$$
\boldsymbol{\pi}_{P_2} = -\frac{h_2}{2}\,{}_{II}\mathbf{e}_3 - r_2\,{}_{II}\mathbf{e}_2''.
\tag{3.5.6}
$$

---

[3]Additional background on the 3-1-3 set of Euler angles can be found in Appendix A and in [54, Chapter 6, Section 8.2].
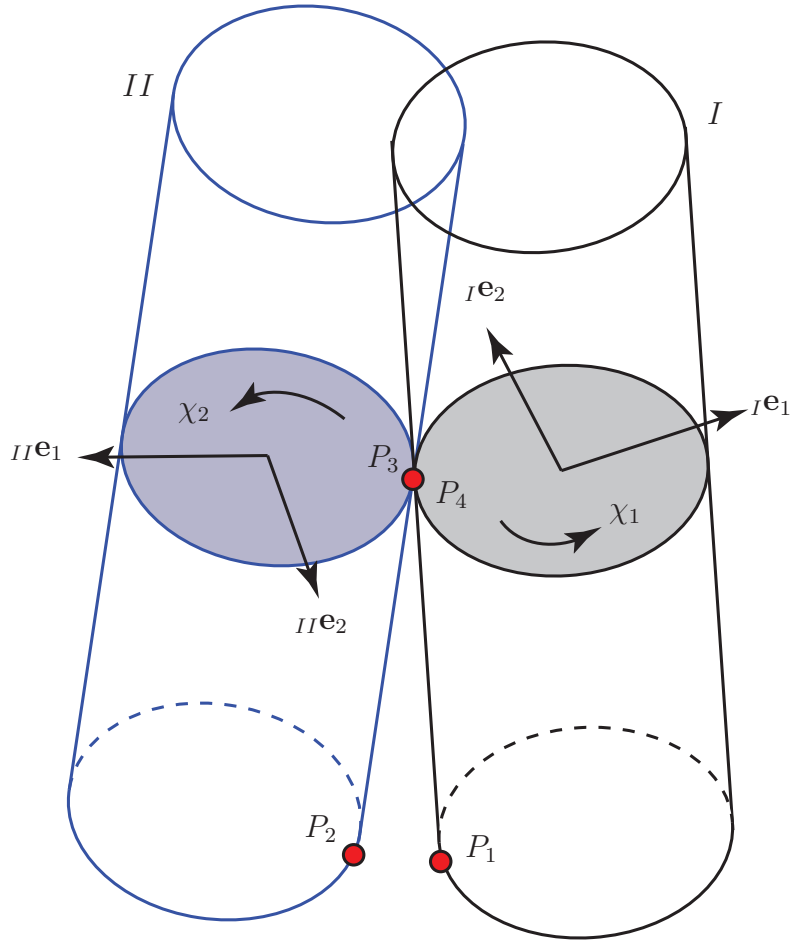
Figure 3.13: The instantaneous contact points for the pair of cylinders. The points P_1 and P_2 are the instantaneous points of contact of cylinders I and II, respectively with the horizontal plane and the points P_3 and P_4 are the instantaneous points of mutual contact.

The instantaneous points of contact between the cylinders are denoted by P_3 and P_4. The vectors $\boldsymbol{\pi}_{P_3}$ and $\boldsymbol{\pi}_{P_4}$ are the position vectors of the instantaneous points of contact P_3 and P_4 relative to the centers of mass of the respective cylinders:

$$\begin{aligned}
\mathbf{x}_3 &= \bar{\mathbf{x}}_I + \boldsymbol{\pi}_{P_3}, \\
\mathbf{x}_4 &= \bar{\mathbf{x}}_{II} + \boldsymbol{\pi}_{P_4}.
\end{aligned} \tag{3.5.7}$$

The tangent planes to both cylinders at P_3 and P_4 are identical and spanned by the basis $\{_I\mathbf{e}_3, \, _{II}\mathbf{e}_3\}$. A unit normal $\mathbf{n}$ can also be defined such that

$$\left\{ _I\mathbf{e}_3, \, _{II}\mathbf{e}_3, \, \mathbf{n} = \frac{_I\mathbf{e}_3 \times \, _{II}\mathbf{e}_3}{||_I\mathbf{e}_3 \times \, _{II}\mathbf{e}_3||} \right\} \tag{3.5.8}$$

is a basis for $\mathbb{E}^3$.

The rolling contact between the two cylinders can be described by the vector equation:

$$\mathbf{v}_3 = \mathbf{v}_4, \tag{3.5.9}$$

where

$$\begin{aligned} \mathbf{v}_3 &= \bar{\mathbf{v}}_I + \boldsymbol{\omega}_I \times \boldsymbol{\pi}_{P_3}, & \mathbf{x}_3 &= \bar{\mathbf{x}}_I + \boldsymbol{\pi}_{P_3}, \\ \mathbf{v}_4 &= \bar{\mathbf{v}}_{II} + \boldsymbol{\omega}_{II} \times \boldsymbol{\pi}_{P_4}, & \mathbf{x}_4 &= \bar{\mathbf{x}}_{II} + \boldsymbol{\pi}_{P_4}. \end{aligned} \tag{3.5.10}$$

In these representations, $\boldsymbol{\pi}_{P_3}$ and $\boldsymbol{\pi}_{P_4}$ are the position vectors of the instantaneous points of contact P_3 and P_4 relative to the centers of mass of the respective cylinders. Both of these relative position vectors are functions of the two sets of Euler angles and Cartesian coordinates. Additional details of the characterization of the contact between the two cylinders are presented in Appendix E.

For the constraints (3.5.3) and (3.5.5) the resulting normal force direction is along $\mathbf{E}_3$ and the static friction force lies in the plane spanned by $\{\mathbf{E}_1, \mathbf{E}_2\}$. To prescribe the friction force at the contact between the two cylinders, it is necessary to decompose the force associated with the constraint (3.5.9) into normal and friction components too. For this, we project the constraint at the cylinders' mutual contact on the basis $\{{}_I\mathbf{e}_3, {}_{II}\mathbf{e}_3, \mathbf{n} = {}_I\mathbf{e}_3 \times {}_{II}\mathbf{e}_3/\|{}_I\mathbf{e}_3 \times {}_{II}\mathbf{e}_3\|\}$. The tangential (frictional) component of the contact constraint lies in the plane spanned by the basis $\{{}_I\mathbf{e}_3, {}_{II}\mathbf{e}_3\}$ while the normal component of the constraint force lies along $\mathbf{n}$. This decomposition relies on the fact that the vectors $\{{}_I\mathbf{e}_3, {}_{II}\mathbf{e}_3\}$ span the coincident tangent plane between the two cylinders at their mutual contact point.

The Final Set of Constraints

In Appendix F, we consider the set of nine constraints (3.5.3), (3.5.5) and (3.5.9) for a pair of cylinders in rolling contact with each other while also in rolling contact with a horizontal surface. We find that only eight of the nine constraints are linearly independent and the system of nine constraints is not integrable. Furthermore, we demonstrate that it is very challenging to extract a set of eight linearly independent constraints from the nine constraints and equally challenging to specify a set of 8 independent Lagrange multipliers associated with rolling constraints (cf. Appendix F.3). While, it is possible to use fixed point iterations to simulate the motion of the rolling cylinders (cf. Capobianco et al. [14, Section 9]), we choose to pursue a different strategy and reexamine the contact condition between the cylinders.

Based on physical intuition, one would expect that the normal force at the contact between the two cylinders is small and thus the friction at the inter-cylinder contact point to be insufficient to prevent the two cylinders from slipping with respect to each other. The pair of rolling constraints between each cylinder and the ground (cf. (3.5.3) and (3.5.5)) and the contact condition between the two cylinders,

$$(\mathbf{v}_3 - \mathbf{v}_4) \cdot \mathbf{n} = 0, \tag{3.5.11}$$

amount to seven scalar constraints. We now propose an additional set of five independent constraints that will completely constrain the 12 degree-of-freedom system. As a result, we will obtain the desired motion described in Section 3.5. The five additional constraints consist of three constraints imposed on the top axis of cylinder I and two constraints imposed on the top axis of cylinder II (points P_5 and P_6 respectively in Figure 3.1). We express the aforementioned constraints as follows:

$$\Pi_\Gamma = 0, \qquad (\Gamma = 1, \dots, 12) \tag{3.5.12}$$

where

$$
\begin{aligned}
&\Pi_1 = \mathbf{v}_1 \cdot \mathbf{E}_1, \qquad \Pi_2 = \mathbf{v}_1 \cdot \mathbf{E}_2, \qquad \Pi_3 = \mathbf{v}_1 \cdot \mathbf{E}_3, \\
&\Pi_4 = \mathbf{v}_2 \cdot \mathbf{E}_1, \qquad \Pi_5 = \mathbf{v}_2 \cdot \mathbf{E}_2, \qquad \Pi_6 = \mathbf{v}_2 \cdot \mathbf{E}_3, \\
&\Pi_7 = (\mathbf{v}_3 - \mathbf{v}_4) \cdot \mathbf{n}, \\
&\Pi_8 = \left(\bar{\mathbf{v}}_I + \boldsymbol{\omega}_I \times \frac{h}{2}{}_I \mathbf{e}_3 \right) \cdot \mathbf{E}_3, \qquad \Pi_9 = \dot{\psi}_1, \qquad \Pi_{10} = \dot{\varphi}_1 - \dot{\varphi}_{1_0}, \\
&\Pi_{11} = \left(\bar{\mathbf{v}}_{II} + \boldsymbol{\omega}_{II} \times \frac{h}{2}{}_{II} \mathbf{e}_3 \right) \cdot \mathbf{E}_3, \qquad \Pi_{12} = \dot{\psi}_2.
\end{aligned}
\tag{3.5.13}
$$

The constraint Π_{10} imposed on cylinder I is a prescribed spin of that cylinder about its longitudinal axis.

3.6 Simulating the Transported Cylinders

Based on our prior analysis of the possible constraints on the contacting cylinders shown in Figures 3.1 and 3.13, we assume rolling contact of each cylinder with the horizontal surface and sliding contact at the points of mutual contact. The cylinders are supported by applied forces acting at the centers of their upper surfaces and are each given an initial spin. Thus, the system of two cylinders is subject to 12 constraints described by equation (3.5.13). Ignoring the occupational hazards of transporting two cylinders simultaneously in this manner, we now demonstrate that there is a mechanical advantage.

Simulating the pair of cylinders is non-trivial. We needed to utilize Capobianco's et al. non-smooth generalized-α method for mechanical systems with frictional contact [14] to perform the simulations. Key features of Capobianco's et al. algorithm include successful resolution of frictional contact and significant reduction of numerical penetration. Numerical penetration, which is a common issue for most popular time stepping schemes, is mitigated though constraint stabilization in the sense of Gear-Gupta-Leimkuhler [26]. An animation of a simulation can be found here:

https://www.youtube.com/watch?v=61_Kfkd_s6o

With the aid of calculations in Appendix E, we set up an initial configuration of two identical cylinders inclined at opposite angles to the vertical and touching at a single point.
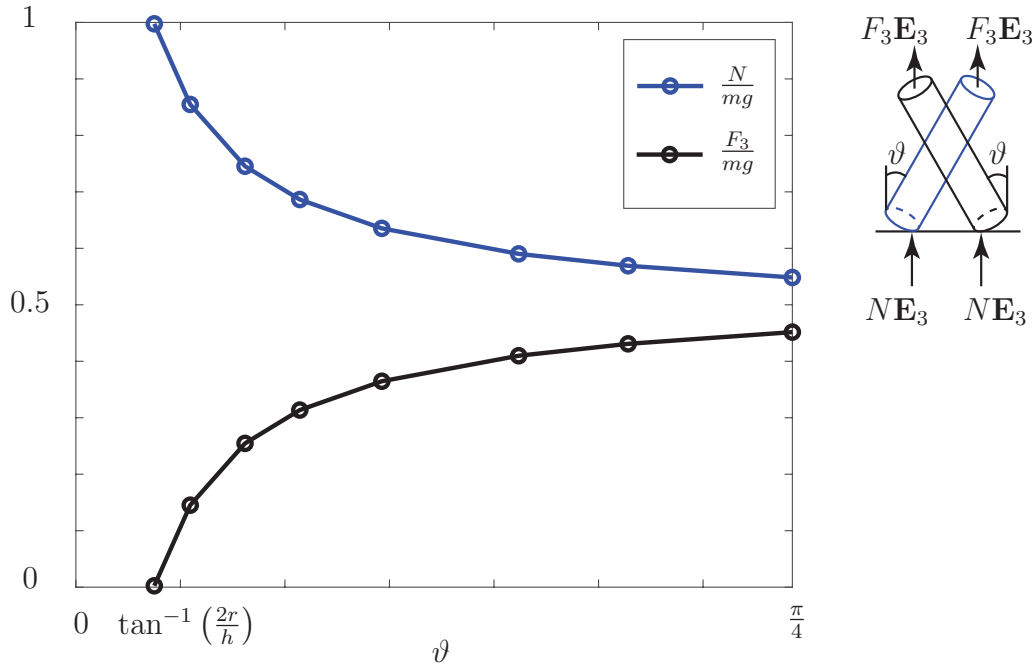
Figure 3.14: The forces needed to sustain the motion of the two cylinders with dimensions $h = 1.2954$ m and $r = 0.1143$ m for several values of angle $\vartheta \in \left(\tan^{-1}\left(\frac{2r}{h}\right), \frac{\pi}{4}\right)$. These forces are identical for both cylinders. The curves $\frac{N}{mg}$ and $\frac{F_3}{mg}$ are drawn in blue and black respectively. The angle $\vartheta = \tan^{-1}\left(\frac{2r}{h}\right)$ corresponds to the case where the vertical normal force on each cylinder completely balances its weight. These results shown are independent of the coefficient of dynamic friction at the contact point between the cylinders.

Motion was initiated by assigning a nonzero angular velocity to $\dot{\varphi}_{1_0}$ (cf. (3.5.13)), propelling cylinder I towards cylinder II. Cylinder II is driven by this motion with $\dot{\varphi}_2 = -\dot{\varphi}_{1_0}$ because both cylinders are subject to rolling constraints at their contact point with the ground. Simulation results show that at steady state the normal force at the inter-cylinder contact is very small (on the order of the algorithm's set tolerance) thereby resulting in a negligible friction force at this contact. This implies that the dynamics of each cylinder in the pair resemble the dynamics of one cylinder that is similarly supported at its top and given a matching initial angular velocity about its longitudinal axis. We also note that the normal forces at the contact point between each cylinder and the ground, as well as the applied forces at the top of each cylinder, are identical due to the configuration's symmetries. More importantly, the simulation results also imply that the analysis in Section 3.3 can be used to compute the range of applied forces F_3 for a given angle of inclination ϑ as well as the minimum force needed to support the motion of the cylinder.

We conduct a series of simulations using two idealized large (220 ft^3) industrial high pressure cylinders that would typically hold welding gas. The cylinders undergo the previously

described motion at varying inclination angles $\vartheta_1 = \vartheta = \vartheta_2$ with respect to the vertical. For each motion, we show in Figure 3.14 the vertical force applied at the top axis of each cylinder and the normal force between each cylinder and the ground. Within a certain range of the angle ϑ, most of the weight of each cylinder is balanced by the normal force, thus enabling an efficient displacement of the cylinders as described in Section 3.1 for a range of applied forces and angles of inclination (as discussed in Section 3.3).

Chapter 4

An Abundance of Motions in the Forced Dynamics of a Stack of Blocks

4.1   Introduction

The dynamics of a vertical stack of blocks has application to a wide range of problems including seismic response of containers in warehouses, the stability of containers on ships at sea, and the transport of stacks of blocks by robots. There has been a growing recent interest among the robotics community in robots stacking objects vertically to form columns [25, 47] or dry stacking objects to form two-dimensional walls [49, 51]. These works have mostly relied on vision-based learning algorithms, although a few also rely on physics simulators. A central question for these stacked objects is the prediction of their dynamics when the columns are perturbed. For instance, will the column stay close to its original configuration or will it collapse?

Unique features of these mechanical systems consisting of stacked blocks include the presence of multiple frictional interfaces, the potential for impacts and collisions, and the necessity of modeling multiple possible configurations. Earlier works on the dynamics of a single rigid block resting on a oscillating horizontal surface show a range of complex dynamics including sensitive dependence on initial conditions, bifurcations of periodic motions and chaotic motions [4, 32, 36, 37]. As a result, one can anticipate a larger variety of complex dynamics for a system of stacked blocks. Owing perhaps to this complexity, other than a recent work by Poincloux et al. [66] on stick-slip behavior of the shearing of a stack of slabs, we were unable to find a substantial literature on the dynamics of stacked blocks.

To study the dynamics of a stack of blocks, recourse to numerical methods is necessary. Earlier works (e.g., [4, 32, 36, 37]) for the single block model the impact of the block with the ground plane using a single coefficient of restitution and integrate the equations of motion between impacts. The methods used by the aforementioned authors are known as event driven. Event-driven schemes resolve every impact which makes them unsuitable to solve motion with infinitely many impacts in a finite time interval, i.e., motions with accumulation

points [14].[1] Other authors, e.g., [75, 76], assume that the block rests on an elastic foundation and do not need to consider the possibility of impact in their studies. A related elastic interface is used in the Discrete Element Method [41, 68] used to analyze colliding rigid bodies.

In the present chapter, we will use an event-capturing method to simulate the dynamics of stack of blocks. The method is based on Capobianco et al.'s [14] non-smooth generalized-α method for systems with friction and impenetrability. The method is used to explore the dynamics of a system of stacked blocks. Our analysis reproduces a well-known instability in the Tower of Lire and shows that low frequency excitation of a stack of blocks is often more detrimental than high frequency excitation. When there is a change in the contact configuration of the stack, we find that an abundance of solutions is possible - making it highly improbable that an algorithm can be used to stabilize a stack of blocks once instability has set in.

An outline of this chapter is as follows. In Section 4.2, we define kinematical parameters and contact conditions for a stack of blocks. This section also contains a description of the numerical method used to explore the dynamics of the block. The toppling of the Leaning Tower of Lire is discussed in Section 4.3. In particular, our simulations demonstrate how the maximum overhang configuration for this stack of blocks is (as expected) unstable to small perturbations. Our main results are presented in Section 4.4 where the effects of a harmonic excitation of the base of the stack can produce an abundance of possible solutions. In Section 4.5, we examine the problem of removing a block quickly from a stack of blocks and explore the possibility of a limiting speed for the removal of the block above which the stack will remain intact. The chapter closes with a discussion of potential future research in this area.

4.2 Preliminary Developments and Numerical Methods

Consider the sample configuration of n vertically stacked blocks depicted in Figure 4.1(a). The kth block has a mass m^k, width w^k, and height h^k. The position vector $\mathbf{r}^k$ of the center of mass of the kth block has the following representation

$$\mathbf{r}^k = x^k \mathbf{E}_1 + y^k \mathbf{E}_2 \qquad (k = 1, \ldots, n). \tag{4.2.1}$$

The basis $\{\mathbf{E}_1, \mathbf{E}_2, \mathbf{E}_3 = \mathbf{E}_1 \times \mathbf{E}_2\}$ is a fixed Cartesian basis for $\mathbb{E}^3$. Referring to Figure 4.1(b), we attach a co-rotational basis $\{\mathbf{e}_1^k, \mathbf{e}_2^k\}$ to the kth block in order to record its rotational

---

[1]The most well known example of a motion with an accumulation point occurs in a ball bouncing on a horizontal surface with a coefficient of restitution $e < 1$. It can be shown that the ball bounces an infinite number of times in a finite amount of time - a phenomenon known as Zeno's paradox (cf. [58, Chapter 6, Section 6.5] and references therein).

motion:

$$\mathbf{e}_1^k = \cos\left(\vartheta^k\right)\mathbf{E}_1 + \sin\left(\vartheta^k\right)\mathbf{E}_2,$$
$$\mathbf{e}_2^k = -\sin\left(\vartheta^k\right)\mathbf{E}_1 + \cos\left(\vartheta^k\right)\mathbf{E}_2, \qquad (k = 1, \ldots, n). \tag{4.2.2}$$

Thus, the configuration of each block is defined by the three coordinates x^k, y^k and ϑ^k. The mass and moment of inertia of the kth block are denoted by m^k and $I^k = \frac{m}{12}\left((w^k)^2 + (h^k)^2\right)$.
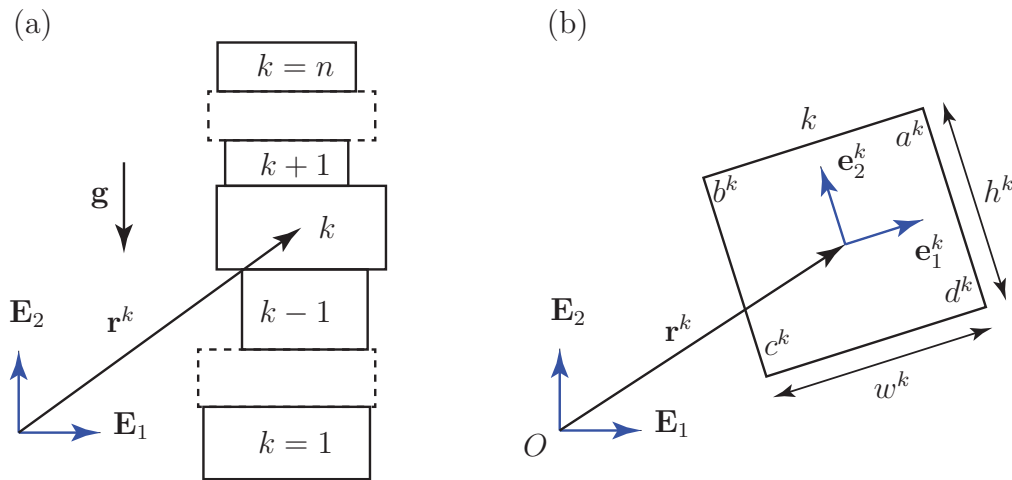
Figure 4.1: (a) A sample configuration of vertically stacked blocks. In an initial static configuration, a block labelled k of width w^k and height h^k lies on top of a block labelled $k-1$ and underneath a block labelled $k+1$. In the current analysis, the blocks need not be uniform. (b) We attach a co-rotational basis $\{\mathbf{e}_1^k, \mathbf{e}_2^k\}$ to a typical block k. We label the corners of each block according to (G.1.1): a^k, b^k, c^k, and d^k.

Expressing the constraint equations between two contacting blocks is complicated by the existence of five possible relative contact configurations (cf. Figure 4.2). In the present work, we choose to write two gap distance constraints for each inter-block contact interface according to equations (G.2.2).[2] When both gap distances are zero, the blocks are not in a state of relative rotation. When only one of two contacts is closed, the cylinders are rotating with respect to each other while touching at one point. When both contacts are open, the two blocks have lost contact vertically. We also include a provision for when two consecutive blocks lose contact in the horizontal direction. Following Cundall [19], we consider the corner-to-corner contact case as a continuation of the cases (b)$_{i-iv}$.

The contact forces between the blocks include normal forces and friction forces. For the friction forces, we distinguish the cases of static and dynamic friction and assume that the coefficients of friction for these two cases are equal. Impact between the blocks is assumed to be completely inelastic (i.e., the coefficient of restitution is equal to zero).

---

[2]A detailed explanation is provided in Appendix G.

(a)

(b)

(i)   (ii)

(iii)   (iv)
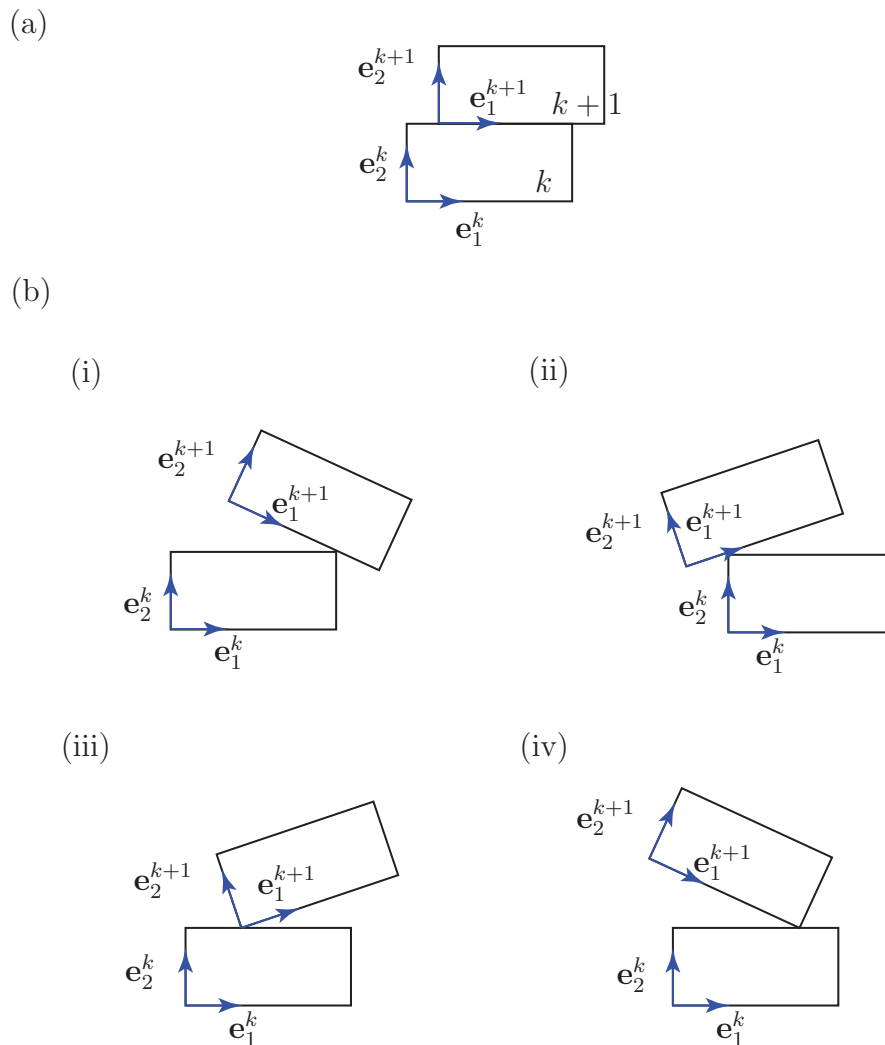
Figure 4.2: (a) A case of edge contact between the kth and $(k+1)$th blocks. (b) Four cases of point contact between the kth and $(k+1)$th blocks: (i) the top right corner of block k contacts the lower surface of block $k+1$; (ii) the top left corner of block k contacts the lower surface of block $k+1$; (iii) the top surface of block k contacts the lower left corner of block $k+1$; and (iv) the top surface of block k contacts the lower right corner of block $k+1$. Here, $k = 1, \ldots, n-1$.

Numerical Methods

A numerical integration scheme for the stack of blocks must be capable of accommodating the non-smooth contact and impacts. The scheme that we employ uses a nonsmooth generalized-α algorithm for systems with friction that is presented by Capobianco et al. [14]. Their work extends a scheme developed by Brüls and coworkers (cf. [3, 10, 18] and

references therein) that in turn adopted the generalized-α algorithm to mechanical systems
with impacts, bilateral constraints, and friction.[3] The generalized-α algorithm used in [10,
3, 9, 14, 18] stabilizes the constraints at the position, velocity, and acceleration levels, thus
preventing the interpenetration of the blocks and numerical integration errors.[4]

The nonsmooth generalized-α scheme enables us to solve the equations of motion of the
blocks subject to the set of constraints described in Appendix G. As the solver progresses
in time, it solves for the contact configuration and motion that simultaneously satisfies the
balance laws and the constraints associated with the computed contact configuration. The
algorithm requires a consistent set of initial conditions and constraint forces that satisfy the
imposed constraints and their derivatives. Since, in our setup, each contact is associated a
pair of constraints, we needed to slightly modify parts of the algorithm presented in [14].
These changes are discussed in Appendix H and the code we use to run our simulations can
be found in
https://github.com/ThH00/abundant-motions-in-the-forced-dynamics-of-a-stack-of-blocks.

Simulation Parameters

Referring to the algorithm parameters in [14], for the numerical simulations our work set
$r = 0.3$, $\rho_{\infty,0} = 0.5$, TOL$n = 10^{-10}$, the finite difference parameter $\varepsilon = 1e^{-6}$, gravity $g = 1$,
and normal and friction restitution coefficients to $e_N = 0$ and $e_F = 0$, respectively. Each
block's mass is set to unity: $m = 1$ and all of the initial configurations start from rest. Except
for the results in Section 4.3, all of the blocks' centers of mass are initially vertically aligned
with $\vartheta^k = 0$ for $k = 1, \ldots, n$. In the simulations where the bottom block is oscillating (cf.
Figures 4.5 and 4.6), the simulation time step is calculated using $\Delta t = \frac{2\pi}{60\omega}$ and $\Delta t = \frac{2\pi}{100\omega}$,
respectively.

In our simulations, we found that some values of spectral radius at infinite frequencies
ρ_∞ can produce a singular Jacobian which are not attributable to the linear dependence of
the constraints. For a given value $\rho_{\infty,0}$ that produces a singular Jacobian, simply changing
the numerical value of ρ_∞ eliminates the singularity. In our simulations, we start with a
value of $\rho_{\infty,0} = 0.5$ and change it as necessary while keeping the restriction that $\rho_{\infty,0} \in [0, 1]$.

4.3   Toppling the Leaning Tower of Lire

The Leaning Tower of Lire [39] is a popular mathematics problem [63, 65, 74] that dates to
the mid-19th century. The solution to the problem involves the calculation of the maximum
overhang that can be achieved at the edge of a table by stacking identical blocks (e.g., coins,
books, or jenga blocks) on top of each other. The static configuration of a stack with a

---

[3]For additional details on the original generalized-α algorithm for structural dynamics, the reader is
referred to [16, 20]

[4]For additional background on constraint stabilization, the interested reader is referred to the seminal
works by Baumgarte [6] and Gear, Leimkuhler, and Gupta [26].

maximum overhang is well known [39, 63]: the outermost edge of a block is at the center of mass of the set of blocks above it (cf. Figure 4.3) and the resulting maximum overhang O_{max} is

$$O_{max} = \sum_{k=1}^{n} \frac{w}{2n},\qquad(4.3.1)$$

where w is the uniform width of the blocks. Thus, a stack of four blocks can be positioned to achieve an overhang that is greater than the width of a single block. To obtain the correct initial constraint forces on the maximum overhang configuration of the blocks, we ran a simulation for one iteration where the normal contacts are forced to be closed and the friction is forced to be static. We confirm that in this case, the normal force exerted on the kth block by the blocks $(1, \ldots k - 1)$ beneath it is at the outer edge of the $k - 1$th block.
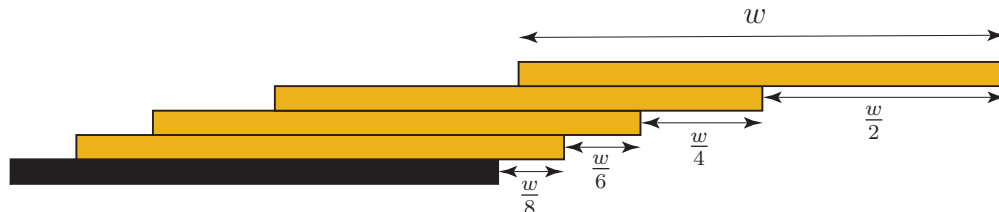
Figure 4.3: The maximum overhang configuration for a set of vertically stacked blocks. Each block has a width w. The figure has been scaled horizontally in the interests of clarity.

The resulting stack of blocks in the maximum overhang configuration is unstable (in the sense of Lyapunov). To explore this instability, we simulate the effects of a perturbation on the set of four blocks shown in Figure 4.3. Our simulations show that displacing the top block by 1% of its width outwards causes it to topple over. In addition, as shown in Figure 4.4(a)-(c)), displacing the lowest block one by 1% of its width outwards causes the entire 4-block column to topple over.

4.4 Harmonic Excitation of a Stack of Blocks

With its widespread application to the fields of transport and earthquake engineering, there is a wealth of studies on the dynamics of structures (including a single block) in contact with a moving horizontal surface [4, 32, 36, 37, 76, 75]. Of particular interest is the dynamics of a stack of blocks that is subject to a horizontal harmonic excitation and dependency of the dynamics of the stack on the frequency of excitation.

We constructed a column of five identical blocks on a wide base that was forced to move in simple harmonic motion in the horizontal direction, $x^1 = A \sin(\omega t)$ where $A = w^2$. The dynamics of the blocks are complicated by the number of possible contact states between each block. Referring to Appendix H, each pair of consecutive blocks can have 46 distinct states

(a) $t = 0$ (b) $t = 5$ (c) $t = 6.4$
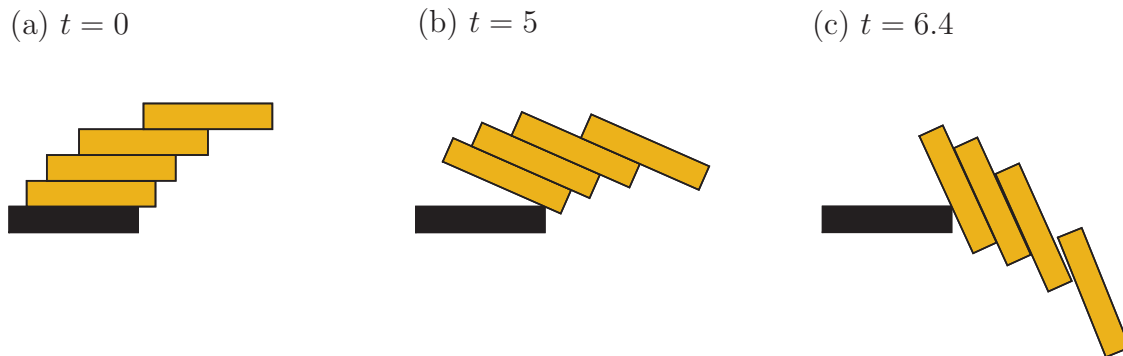
Figure 4.4: The time evolution of the failure of a Leaning Tower of Lire composed of four blocks with the maximum overhang configuration. At $t = 0$, the lowest block is displaced by 1% of its length to the right, the tower collapses and the blocks slide relative to each other as they tumble to the ground. (a) $t = 0$, (b) $t = 5$, and (c) $t = 6.4$. The black block is fixed. For each block, $w = 1$, $h = 0.2$, $\mu = 0.3$, and $\Delta t = 0.01$.

of contact depending on the stick-slip nature of the contact and the associated velocity and acceleration constraints. Thus, for a stack of $n = 4$ blocks, we get a total of 46^4 states or over 4 million possible states. A second possible complication is the presence of Painlevé's paradoxes in the dynamics of rigid bodies with frictional contacts. Fortunately, as discussed in Appendix I, the values of friction we use ($\mu = 0.2$) are much lower than the friction coefficients ($\mu > 4/3$) required to produce the indeterminacy and multiple solutions attributed to the paradoxes.

Algorithm 1 Resolving non converging contact states

Require: iteration fails to converge due to changing contact state
    gather the list of unique contact states from the previous failed iteration
    for each unique contact state **do**
        run the code one iteration while keeping the contact state fixed
        if the code converges **then**
            continue running solver starting from this contact state
        end if
    end for

The simulations of the shaken stack of blocks proved far more complex than we originally imagined. We found cases where the iterations at a given time step would not converge because the contact states would change from one iteration to the next and oscillate between two or more potential contact states. In these instances, Algorithm 1 was used to determine the contact state of the blocks. Each contact state for which the numerical scheme converges becomes a new solution branch: that is, a new starting point, for our simulations. The results of a sample implementation are presented in Figure 4.5. Some simulations found
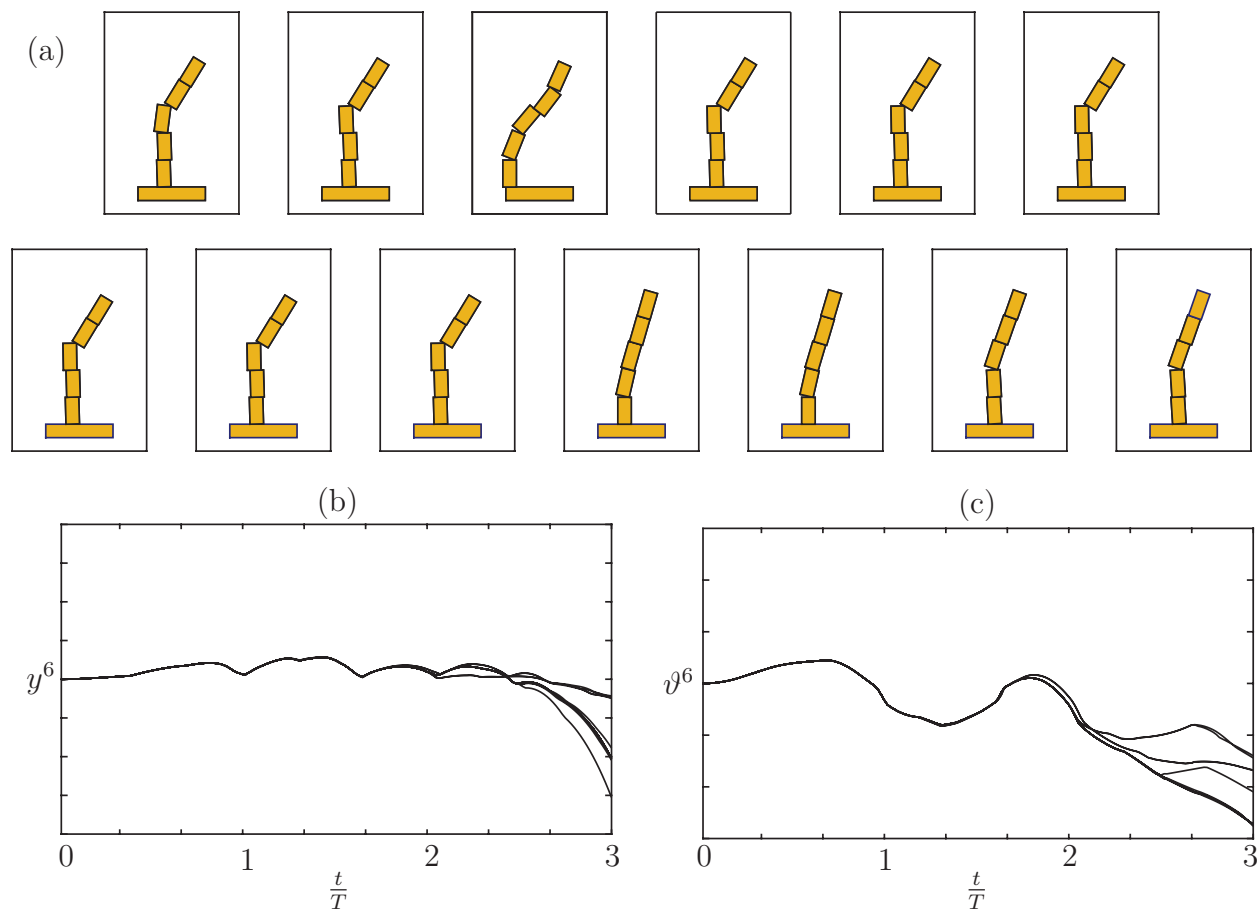
Figure 4.5: (a) A snapshot of distinct solutions arising from the motion of a column of 6 blocks after the completion of 3 oscillations of the bottom block where $x^1 = \sin\left(\frac{3\pi}{2}t\right)$. Graphs (b) and (c) show the time change of the y^6 coordinate of the center of mass and ϑ^6 coordinate of the top block respectively. In these simulations, blocks $n = 2, \ldots, 6$ have a width $w = 0.2$, a height $h = 0.4$, and the coefficient of friction is $\mu = 0.3$. The remaining simulation parameters are discussed in Section 4.2.

hundreds and sometimes even thousands of solutions within the first four oscillation cycles of the bottom block. The large number of bifurcations evident in Figure 4.5 can be explained by the large number of possible contact states of two consecutive blocks discussed earlier. Because of the large number of possible contact states, an exhaustive search for all possible solutions is computationally expensive. In addition, the results will be affected by changing the simulation parameters, such as the time step.

We ran a series of simulations for different values of the forcing frequency ω to assess the stability of the stack.[5] These experiments can be viewed as related to the problem

---

[5]In these simulations, the blocks $2, \ldots, 5$ are taken to be uniform with a width $w^k = 0.2$ m and height
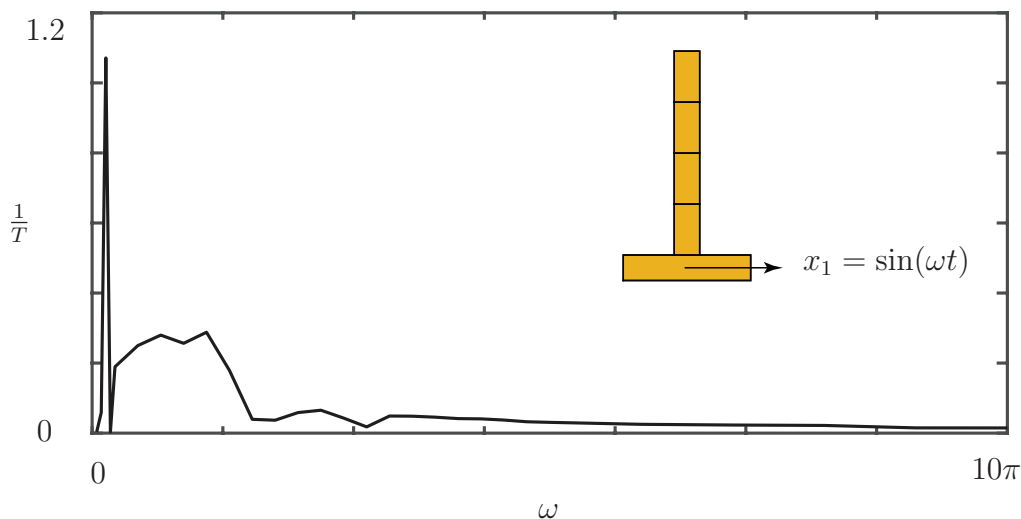
Figure 4.6: A plot of $\frac{1}{T}$ as function of the angular frequency ω of the bottom block. The variable T is the time of the onset of failure where failure is defined to occur when any block in the stack looses all contact with the block beneath it.

of stabilizing double and triple pendula. We plotted the reciprocal of the time of failure onset of the stack versus different angular frequencies. The failure is defined as the instance when any two blocks in the stack lose contact completely. As summarized in Figure 4.6, the stack tends to be more stable at very low frequencies, becomes increasingly unstable as the frequency increases until a sufficient high frequency is reached where the column is stable again. The stability results for the stack have similarities to those presented in Hogan [32] for the forced motion of a single block.

4.5 Sliding the Bottom Block

Imagine a vertical stack of blocks at rest and consider removing the bottom block by imposing an external force so it develops a horizontal velocity $\dot{\mathbf{r}}^1 = v_0\mathbf{E}_1$. If the velocity is sufficiently small and friction is still static, then one anticipates that the entire stack should start to move horizontally. On the other hand if the velocity is sufficiently large and friction is kinetic, then one expects that the other blocks should be unperturbed before falling vertically as one. For intermediate velocities where friction is kinetic, the other blocks would rotate about the corner of the bottom block, thus causing their unstructured failure.

To validate these expectations, we simulate the dynamics of a stack of five blocks where the lowermost block is propelled horizontally at a constant velocity. The results of our numer-

---

$h^k = 0.4$ m while $w^1 = 1$ m and $h^1 = 0.1$ m. The friction coefficient is set to $\mu = 0.2$ at all contacting surfaces.
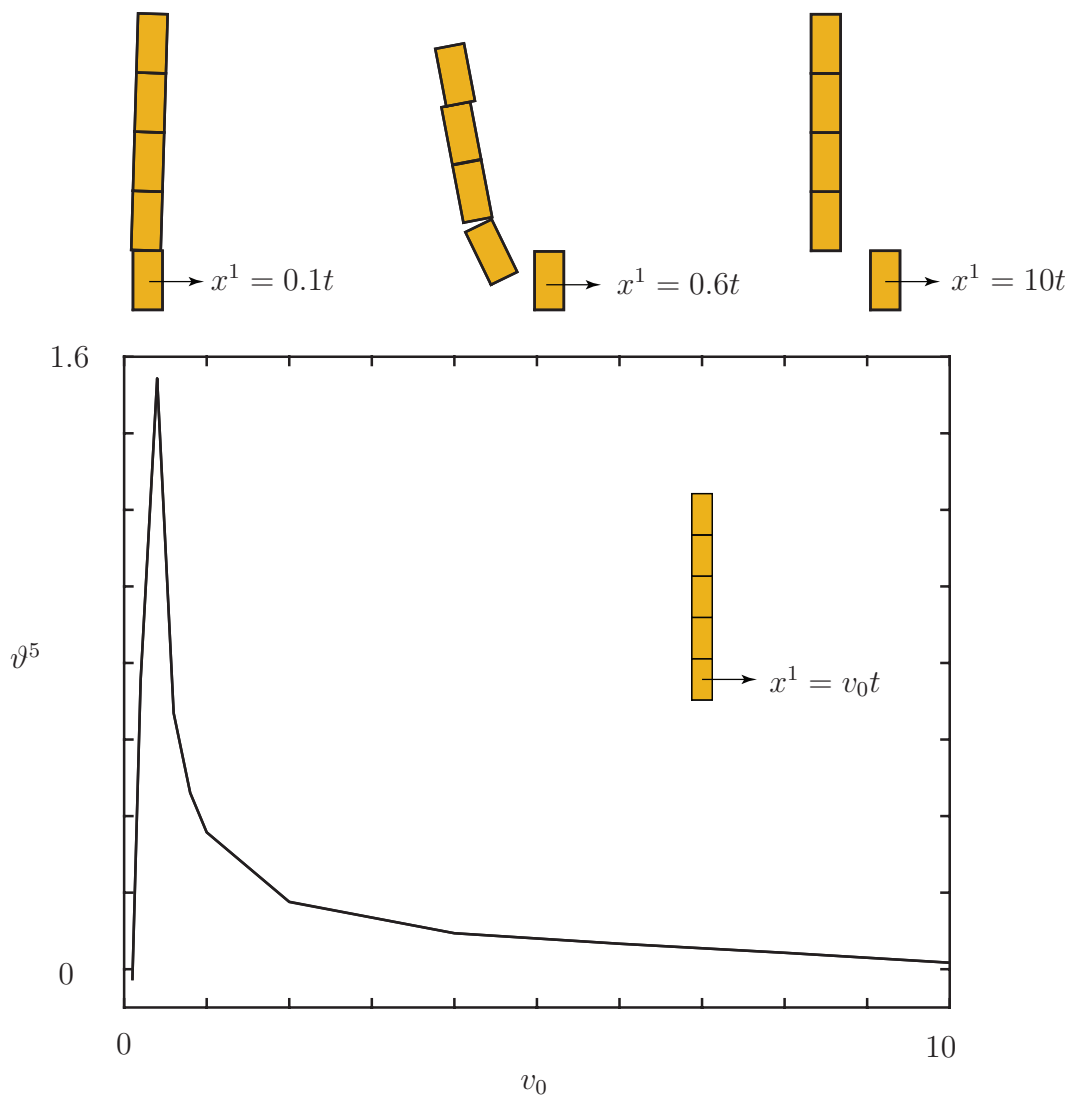
Figure 4.7: The change of the inclination angle of the top block in the stack versus the speed v_0 of the bottom block at time $t = 3$. These is very minor variability in some of the results due to the multiplicity of solutions which is not discernible in this graphical presentation of the results.

ical simulations are shown in Figure 4.7 where the angle of inclination ϑ^5 of the uppermost block is shown.[6]

---

[6]In these simulations, the dimensions of all blocks $k = 1, \ldots, 5$ are $w^k = 0.2$ m and $h^k = 0.4$ m. The friction coefficient at all contact surfaces is $\mu = 0.2$.

4.6 Conclusion

Works in the 1960s-1980s on the dynamics and stability of a block have produced several interesting results. These results include the sensitivity of the dynamics of these systems to initial conditions and the possibility of chaotic motions. Subsequent works on formulation of problems involving constraints, impact and friction (e.g., [6, 26, 64]) laid the foundation for the simulation of systems of rigid bodies with impact and friction (e.g., [3, 9, 14]) that were used in this chapter to explore the dynamics of a stack of blocks. The simulations involved solving discontinuous equations of motion subject to constraints that change depending on the configuration of the system, which also need to be calculated. The numerical experiments on the forced dynamics of a stack of blocks we have presented are far from exhaustive. We hope that this work inspires researchers to think about related problems.

From a practical standpoint, this work is applicable to the areas of packaging and transportation of materials. The developed framework can be integrated into the design of model-informed control strategies to mitigate the toppling of stacked objects. With this, one has to keep in mind that these structures are very sensitive to initial conditions. The bifurcations and multiplicity of solutions may make it impossible to predict the configuration of the stack once the onset of instability has occurred.

Chapter 5

Concluding Remarks

In this thesis, we explored three ubiquitous mechanical systems[1]: a sphere rolling in the plane in Chapter 2, a locomotion mechanism for two contacting cylinders in Chapter 3, and the forced motion of a two-dimensional discrete column of blocks in Chapter 4. The motions of these systems are dictated by their respective constraints.

The dynamics of these systems have great relevance to robotics. The holonomy of a rolling sphere is central to motion planning of spherical robots such as Star Wars' BB8 or Omni Wheels. The investigation of the cylinders is crucial to transport problems. Simulating the motion of a stack of blocks has applications to stacks on moving surfaces, such as during an earthquake or transport.

The study of the rolling sphere expanded upon the classical concept of holonomy to obtain novel results relating its change in orientation resulting from traversing one closed rectangular path. To simulate the motion of the cylinders and the stack of blocks, we used a modern numerical method, the nonsmooth generalized-α method for systems with friction. Simulating these systems faithfully was only possible thanks to recent developments in the generalized-α algorithm by a number of researchers over the course of two decades.

This thesis has revealed the remarkably rich dynamics of a stack of objects, anticipated to be the primary novel contribution of this work. Many problems in this area remain to be explored.

---

[1]The work in Chapter 2 is published in [33]. As of June 2024, the work in Chapter 3 has been submitted for publication [34], and the work in Chapter 4 is being prepared for submission to an archival journal.

Bibliography

[1] P. Akella, O. M. O'Reilly, and K. Sreenath. "Controlling the locomotion of spherical robots or why BB-8 Works". In: *ASME Journal of Mechanisms and Robotics* 11.2 (2019), p. 024501. DOI: 10.1115/1.4042296.

[2] P. Appell. "Sur l'intégration des équations du mouvement d'un corps pesant de révolution roulant par une arête circulaire sur un plan horizontal". In: *Rendiconti del Circolo Mathematico di Palermo* 14 (1900), pp. 1–6. DOI: 10.1007/BF03012823.

[3] M. Arnold and O. Brüls. "Convergence of the generalized-alpha scheme for constrained mechanical systems". In: *Multibody System Dynamics* 18 (2007), pp. 185–202. DOI: 10.1007/s11044-007-9084-0.

[4] M. Aslam, W. G. Godden, and D. T. Scalise. "Earthquake rocking response of rigid bodies". In: *Journal of the Structural Division* 106.2 (1980), pp. 377–392. DOI: 10.1061/JSDEAG.0005363.

[5] M. Batista. "Steady motion of a rigid disk of finite thickness on a horizontal plane". In: *International Journal of Non-Linear Mechanics* 41.4 (2006), pp. 605–621. DOI: 10.1016/j.ijnonlinmec.2006.02.005.

[6] J. Baumgarte. "Stabilization of constraints and integrals of motion in dynamical systems". In: *Computer Methods in Applied Mechanics and Engineering* 1.1 (1972), pp. 1–16. DOI: 10.1016/0045-7825(72)90018-7.

[7] M. Berry. "Anticipations of the geometric phase". In: *Physics Today* 43.12 (1990), pp. 34–40. DOI: 10.1063/1.881219.

[8] A.V. Borisov and I.S. Mamaev. "Conservation laws, hierarchy of dynamics and explicit integration of nonholonomic systems". In: *Regular and Chaotic Dynamics* 13.5 (2008), pp. 443–490. DOI: 10.1134/S1560354708050079.

[9] O. Brüls, V. Acary, and A. Cardona. "Simultaneous enforcement of constraints at position and velocity levels in the nonsmooth generalized-alpha scheme". In: *Computer Methods in Applied Mechanics and Engineering* 281 (2014), pp. 131–161. DOI: 10.1016/j.cma.2014.07.025.

[10] O. Brüls, A. Cardona, and M. Arnold. "Lie group generalized-time integration of constrained flexible multibody systems". In: *Mechanism and Machine Theory* 48 (2012), pp. 121–137. DOI: 10.1007/s11044-007-9084-0.

[11]   G. H. Bryan. *Stability in Aviation: An Introduction to Dynamical Stability as Applied to the Motion of Aeroplanes*. Macmillan's Science Monographs. London: Macmillan and Co., 1911.

[12]   R. L. Bryant. "Geometry of manifolds with special holonomy: "100 years of holonomy"". In: *150 Years of Mathematics at Washington University in St. Louis*. Vol. 395. Contemporary Mathematics. Providence, RI: American Mathematical Society, 2006, pp. 29–38. DOI: 10.1090/conm/395/07414.

[13]   W. L. Burke. *Applied Differential Geometry*. Cambridge: Cambridge University Press, 1985. DOI: 10.1017/CBO9781139171786.

[14]   G. Capobianco et al. "A nonsmooth generalized-alpha method for mechanical systems with frictional contact". In: *International Journal for Numerical Methods in Engineering* 122.22 (2021), pp. 6497–6526. DOI: 10.1002/nme.6801.

[15]   R. Chase and A. Pandya. "A review of active mechanical driving principles of spherical robots". In: *Robotics* 1 (2012), pp. 3–23. DOI: 10.3390/robotics1010003.

[16]   J. Chung and G. M. Hulbert. "A Time integration algorithm for structural dynamics with improved numerical dissipation: The generalized-α method". In: *ASME Journal of Applied Mechanics* 60.2 (1993), pp. 371–375. DOI: 10.1115/1.2900803.

[17]   E. A. Codman. *The Shoulder: Rupture of the Supraspinatus Tendon and Other Lesions in or about the Subacromial Bursa*. Second. Boston: T. Todd Company, 1934.

[18]   A. Cosimo et al. "A robust nonsmooth generalized-alpha scheme for flexible systems with impacts". In: *Multibody System Dynamics* 48 (2020), pp. 127–149. DOI: 10.1007/s11044-019-09692-2.

[19]   P. A. Cundall. "Formulation of a three-dimensional distinct element model—Part I. A scheme to detect and represent contacts in a system composed of many polyhedral blocks". In: *International Journal of Rock Mechanics and Mining Sciences & Geomechanics Abstracts*. Vol. 25. 3. 1988, pp. 107–116. DOI: 10.1016/0148-9062(88)92293-0.

[20]   S. Erlicher, L. Bonaventura, and O. Bursi. "The analysis of the generalized-α method for non-linear dynamic problems". In: *Computational Mechanics* 28 (2002), pp. 83–104. DOI: 10.1007/s00466-001-0273-z.

[21]   L. Euler. "De motum corporum circa punctum fixum mobilum". In: *Leonhardi Euleri Opera Postuma*. Vol. 2. Mathematica Et Physica: Anno MDCCCXLIV Detecta. Zürich: Orell Füssli, 1862, pp. 43–62. URL: https://scholarlycommons.pacific.edu/euler-works/825/.

[22]   A. Fick. "Die bewegungen des menschlichen augapfels". In: *Zeitschrift für rationelle Medizin* 4 (1854), pp. 109–128.

[23]   A. R. Forsyth. *Theory of Differential Equations*. Vol. 1. London: Cambridge University Press, 1890.

[24] G. Frobenius. "Ueber das Pfaffsche problem". In: *Crelles Journal für die reine und angewandte Mathematik* 82 (1877), pp. 230–315. DOI: `10.1515/crll.1877.82.230`.

[25] F. Furrer et al. "Autonomous robotic stone stacking with online next best object target pose planning". In: *2017 IEEE International Conference on Robotics and Automation ICRA*. IEEE. 2017, pp. 2350–2356. DOI: `10.1109/ICRA.2017.7989272`.

[26] C. W. Gear, B. Leimkuhler, and G. K. Gupta. "Automatic integration of Euler-Lagrange equations with constraints". In: *Journal of Computational and Applied Mathematics* 12 (1985), pp. 77–90. DOI: `10.1016/0377-0427(85)90008-1`.

[27] F. Génot and B. Brogliato. "New results on Painlevé paradoxes". In: *European Journal of Mechanics - A/Solids* 18.4 (1999), pp. 653–677. DOI: `10.1016/S0997-7538(99)00144-8`.

[28] T. Haslwanter. "Mathematics of three-dimensional eye rotations". In: *Vision Research* 35.12 (1995), pp. 1727–1739. DOI: `10.1016/0042-6989(94)00257-M`.

[29] T. Hawkins. "Frobenius, Cartan, and the Problem of Pfaff". In: *Archive for History of Exact Sciences* 59.4 (2005), pp. 381–436. DOI: `10.1007/s00407-004-0095-4`.

[30] H. Helmholtz. "Ueber die normalen bewegungen des menschlichen auges". In: *Archiv für Ophthalmologie* 9.2 (1863), pp. 153–214. DOI: `10.1007/BF02720895`.

[31] E. G. Hemingway and O. M. O'Reilly. "Perspectives on Euler angle singularities, gimbal lock, and the orthogonality of applied forces and applied moments". In: *Multibody System Dynamics* 44.1 (2018), pp. 31–56. DOI: `10.1007/s11044-018-9620-0`.

[32] S. J. Hogan. "On the dynamics of rigid-block motion under harmonic forcing". In: *Proceedings of the Royal Society of London. A. Mathematical and Physical Sciences* 425.1869 (1989), pp. 441–476. DOI: `10.1098/rspa.1989.0114`.

[33] T. E. Honein and O. M. O'Reilly. "Explorations of the holonomy of a rolling sphere". In: *Proceedings of the Royal Society A* 480.2282 (2024), p. 20230684. DOI: `10.1098/rspa.2023.0684`.

[34] T. E. Honein and O. M. O'Reilly. "On the Dynamics of Transporting Rolling Cylinders". In: *submitted to Nonlinear Dynamics* (2024).

[35] T. E. Honein and O. M. O'Reilly. "The geometry of equations of motion: particles in equivalent universes". In: *Nonlinear Dynamics* 104.4 (2021), pp. 2979–2994. DOI: `10.1007/s11071-021-06565-2`.

[36] G. W. Housner. "The behavior of inverted pendulum structures during earthquakes". In: *Bulletin of the Seismological Society of America* 53.2 (1963), pp. 403–417. DOI: `10.1785/BSSA0530020403`.

[37] Y. Ishiyama. "Motions of rigid bodies and criteria for overturning by earthquake excitations". In: *Earthquake Engineering & Structural Dynamics* 10.5 (1982), pp. 635–650. DOI: `10.1002/eqe.4290100502`.

[38] B. D. Johnson. "The nonholonomy of the rolling sphere". In: *American Mathematical Monthly* 200.6 (2007), pp. 500–508. URL: https://www.jstor.org/stable/27642248.

[39] Paul B. Johnson. "Leaning tower of Lire". In: *American Journal of Physics* 23.4 (1955), pp. 240–240. DOI: 10.1119/1.1933957.

[40] J. Junkins and M. D. Shuster. "The geometry of the Euler angles". In: *The Journal of the Astronautical Sciences* 41.4 (1993), pp. 531–543.

[41] J. Kafashan et al. "Two-dimensional particle shapes modelling for DEM simulations in engineering: A review". In: *Granular Matter* 21 (2019), pp. 1–19. DOI: 10.1007/s10035-019-0935-1.

[42] Y.L. Karavaev and A.A. Kilin. "The dynamics and control of a spherical robot with an internal omniwheel platform". In: *Regular and Chaotic Dynamics* 20 (2015), pp. 134–152. DOI: 10.1134/S1560354715020033.

[43] Lord Kelvin and P. G. Tait. *A Treatise on Natural Philosophy*. Reprinted. Cambridge: Cambridge University Press, 1912.

[44] P. Kessler and O. M. O'Reilly. "The ringing of Euler's disk". In: *Regular and Chaotic Dynamics* 7.1 (2002), pp. 49–60. DOI: 10.1070/RD2002v007n01ABEH000195.

[45] D. J. Korteweg. "Extrait d'une lettre à M. Appell". In: *Rendiconti del Circolo Mathematico di Palermo* 14 (1900), pp. 7–8. DOI: 10.1007/BF03012824.

[46] J. L. Lagrange. "Théorie de la libration de la Lune, et des autres phénomènes qui dépendent de la figure non sphèrique de cette Planète". In: *Nouveaux Mémoires de l'Académie Royale des Sciences et des Belles-Lettres de Berlin* 30 (1780), pp. 203–309.

[47] A. X. Lee et al. "Beyond pick-and-place: Tackling robotic stacking of diverse shapes". In: *5th Annual Conference on Robot Learning*. Ed. by A. Faust, D. Hsu, and G. Neumann. Vol. 164. Proceedings of Machine Learning Research. PMLR, 2021. URL: https://openreview.net/forum?id=U0Q8CrtBJxJ.

[48] M. Levi. "Geometric phases in the motion of rigid bodies". In: *Archive for Rational Mechanics and Analysis* 122.3 (1993), pp. 213–229. DOI: 10.1007/BF00380255.

[49] Y. Liu, J. Choi, and N. Napp. "Planning for robotic dry stacking with irregular stones". In: *Field and Service Robotics: Results of the 12th International Conference*. Springer. 2021, pp. 321–335. DOI: 10.1007/978-981-15-9460-1_23.

[50] P. Lötstedt. "Coulomb friction in two-dimensional rigid body systems". In: *Zeitschrift für Angewandte Mathematik und Mechanik* 61.12 (1981), pp. 605–615. DOI: 10.1002/zamm.19810611202.

[51] A. Menezes et al. "From rocks to walls: a model-free reinforcement learning approach to dry stacking with irregular rocks". In: *Proceedings of the IEEE/CVF Conference on Computer Vision and Pattern Recognition*. 2021, pp. 2057–2065. DOI: 10.1109/CVPRW53098.2021.00234.

[52]   E. Nelson. *Tensor Analysis*. Princeton, New Jersey: Princeton University Press, 1967.

[53]   A. Novelia and O. M. O'Reilly. "On geodesics of the rotation group SO(3)". In: *Regular and Chaotic Dynamics* 20.6 (2015), pp. 729–738. DOI: 10.1134/S1560354715060088.

[54]   O. M. O'Reilly. *Intermediate Dynamics for Engineers: Newton-Euler and Lagrangian Mechanics*. second. Cambridge: Cambridge University Press, 2020. DOI: 10.1017/9781108644297.

[55]   O. M. O'Reilly. "The dual Euler basis: Constraints, potentials, and Lagrange's equations in rigid body dynamics". In: *ASME Journal of Applied Mechanics* 74.2 (2007), pp. 256–258. DOI: 10.1115/1.2190231.

[56]   O. M. O'Reilly. "The dynamics of rolling disks and sliding disks". In: *Nonlinear Dynamics* 10.3 (1996), pp. 287–305. DOI: 10.1007/BF00045108.

[57]   O. M. O'Reilly and A. R. Srinivasa. "A simple treatment of constraint forces and constraint moments in the dynamics of rigid bodies". In: *ASME Applied Mechanics Reviews* 67.1 (2014), pp. 014801-014801–8. DOI: 10.1115/1.4028099.

[58]   Oliver M. O'Reilly. *Engineering Dynamics: A Primer*. Third. New York: Springer-Verlag, 2019. DOI: 10.1007/978-3-030-11745-0.

[59]   P. Painlevé. "Sur les lois du frottement de glissement". In: *Comptes Rendus des Séances de l'Académie des Sciences* 121 (1895), pp. 112–115.

[60]   P. Painlevé. "Sur les lois du frottement de glissement". In: *Comptes Rendus des Séances de l'Académie des Sciences* 141 (1905), pp. 401–405.

[61]   P. Painlevé. "Sur les lois du frottement de glissement". In: *Comptes Rendus des Séances de l'Académie des Sciences* 141 (1905), pp. 546–552.

[62]   J. G. Papastavridis. *Analytical Mechanics: A Comprehensive Treatise on the Dynamics of Constrained Systems*. Reprint. Singapore: World Scientific, 2014. DOI: 10.1142/8058.

[63]   M. Paterson et al. "Maximum overhang". In: *The American Mathematical Monthly* 116.9 (2009), pp. 763–787. DOI: 10.4169/000298909X474855.

[64]   F. Pfeiffer and C. Glocker. *Multibody Dynamics with Unilateral Contacts*. Weinheim, Germany: Wiley-VCH Verlag GmbH & Co. KGaA, 1996. DOI: 10.1002/9783527618385.

[65]   J. B. Phear. *Elementary Mechanics*. New York, USA: MacMillan, 1850.

[66]   S. Poincloux, P. M. Reis, and T. W. J. de Geus. "Stick-slip in a stack: How slip dissonance reveals aging". In: *Physical Review Research* 6 (1 2024), p. 013080. DOI: 10.1103/PhysRevResearch.6.013080.

[67]   J. C. Politti et al. "Codman's paradox of the arm's rotation is not a paradox: Mathematical validation". In: *Medical Engineering and Physics* 20.4 (1998), pp. 257–260. DOI: 10.1016/S1350-4533(98)00020-4.

[68]   J. Rojek. "Contact modeling in the discrete element method". In: *Contact Modeling for Solids and Particles* (2018), pp. 177–228. DOI: 10.1007/978-3-319-90155-8_4.

[69]   Y. Shen and W. J. Stronge. "Painlevé paradox during oblique impact with friction". In: *European Journal of Mechanics - A/Solids* 30.4 (2011), pp. 457–467. DOI: 10.1016/j.euromechsol.2011.03.001.

[70]   M. D. Shuster. "A survey of attitude representations". In: *American Astronautical Society. Journal of the Astronautical Sciences* 41.4 (1993), pp. 439–517.

[71]   M. Srinivasan and A. Ruina. "Rocking and rolling: A can that appears to rock might actually roll". In: *Phys. Rev. E* 78 (6 2008), p. 066609. DOI: 10.1103/PhysRevE.78.066609.

[72]   D. E. Stewart. "Rigid-body dynamics with friction and impact". In: *SIAM Review* 42.1 (2000), pp. 3–39. DOI: 10.1137/S0036144599360110.

[73]   P. G. Tait. "On the rotation of a rigid body about a fixed point". In: *Proceedings of the Royal Society of Edinburgh* 6 (1869), pp. 430–434. DOI: 10.1017/S0370164600046101.

[74]   W. Walton. *A Collection of Problems in Illustration of the Principles of Theoretical Mechanics*. Cambridge, England: Deighton, Bell and Company, 1855.

[75]   C.-S. Yim and A. K. Chopra. "Earthquake response of structures with partial uplift on Winkler foundation". In: *Earthquake Engineering & Structural Dynamics* 12.2 (1984), pp. 263–281. DOI: 10.1002/eqe.4290120209.

[76]   S. C.-S. Yim and A. K. Chopra. "Dynamics of structures on two-spring foundation allowed to uplift". In: *Journal of Engineering Mechanics* 110.7 (1984), pp. 1124–1146. DOI: 10.1061/(ASCE)0733-9399(1984)110:7(1124).

[77]   J. W. Zwanziger, M. Koenig, and A. Pines. "Berry's phase". In: *Annual Review of Physical Chemistry* 41.1 (1990), pp. 601–646. DOI: 10.1146/annurev.pc.41.100190.003125.

Appendix A

3-1-3 Euler Angle Parameterization of a Rotation Tensor

The rotation tensors $\mathbf{Q}_1$ and $\mathbf{Q}_2$ of the individual cylinders in Chapter 3 are each parameterized by a separate set of 3-1-3 Euler angles. To provide relevant background and details, it suffices to consider a rotation tensor $\mathbf{Q}$ parameterized by a set of 3-1-3 Euler angles ψ, ϑ, and φ. These developments are also applicable to the parameterization of the rotation tensor of the sphere in Chapter 2.

A.1 The Euler angles and Euler basis

The Euler angle parameterization of $\mathbf{Q}$ can be imagined as a set of 3 compound rotations. The first rotation is defined a rotation about the $\mathbf{E}_3$ axis through a counter-clockwise angle ψ. This rotation can be used to define a second basis:

$$\mathbf{e}_1' = \cos(\psi)\mathbf{E}_1 + \sin(\psi)\mathbf{E}_2, \quad \mathbf{e}_2' = -\sin(\psi)\mathbf{E}_1 + \cos(\psi)\mathbf{E}_2, \quad \mathbf{e}_3' = \mathbf{E}_3. \tag{A.1.1}$$

The second rotation is defined as a rotation about $\mathbf{e}_1'$ through a counterclockwise angle of rotation ϑ:

$$\mathbf{e}_1'' = \mathbf{e}_1', \quad \mathbf{e}_2'' = \cos(\vartheta)\mathbf{e}_2' + \sin(\vartheta)\mathbf{e}_3', \quad \mathbf{e}_3'' = -\sin(\vartheta)\mathbf{e}_2' + \cos(\vartheta)\mathbf{e}_3'. \tag{A.1.2}$$

The third and final rotation is defined as a rotation about $\mathbf{e}_3''$ through a counterclockwise angle of rotation φ:

$$\mathbf{e}_1 = \cos(\varphi)\mathbf{e}_1'' + \sin(\varphi)\mathbf{e}_2'', \quad \mathbf{e}_2 = -\sin(\varphi)\mathbf{e}_1'' + \cos(\varphi)\mathbf{e}_2'', \quad \mathbf{e}_3 = \mathbf{e}_3''. \tag{A.1.3}$$

That is, $\mathbf{Q} = \sum_{i=1}^{3} \mathbf{e}_i \otimes \mathbf{E}_i$ where $\otimes$ is the tensor product. The unit vectors used to define the rotations are known as the Euler basis vectors $\{\mathbf{g}_1, \mathbf{g}_2, \mathbf{g}_3\}$. For a 3-1-3 set of Euler angles:

$$\mathbf{g}_1 = \mathbf{E}_3, \qquad \mathbf{g}_2 = \mathbf{e}_1', \qquad \mathbf{g}_3 = \mathbf{e}_3. \tag{A.1.4}$$

A.2 The Angular Velocity Vector

A discussion of the representations of the angular velocity vector can be found in [54, Section 6.8.2]:

$$\begin{aligned}
\boldsymbol{\omega} &= \dot{\psi}\mathbf{E}_3 + \dot{\vartheta}\mathbf{e}_1' + \dot{\varphi}\mathbf{e}_3 \\
&= \left(\dot{\vartheta}\cos(\varphi) + \dot{\psi}\sin(\vartheta)\sin(\varphi)\right)\mathbf{e}_1 + \left(-\dot{\vartheta}\sin(\varphi) + \dot{\psi}\sin(\vartheta)\cos(\varphi)\right)\mathbf{e}_2 \\
&\quad + \left(\dot{\varphi} + \dot{\psi}\cos(\vartheta)\right)\mathbf{e}_3.
\end{aligned} \tag{A.2.1}$$

The dual basis vectors are defined by the relations [55]

$$\mathbf{g}_k \cdot \mathbf{g}^i = 1 \text{ if } i = k \text{ and otherwise } 0. \tag{A.2.2}$$

Thus, $\boldsymbol{\omega} \cdot \mathbf{g}^1 = \dot{\psi}$, $\boldsymbol{\omega} \cdot \mathbf{g}^2 = \dot{\vartheta}$, and $\boldsymbol{\omega} \cdot \mathbf{g}^3 = \dot{\varphi}$. Expressions for the dual basis vectors can be found in [54, Section 6.8.2].

A.3 Matrix Identities

In the sequel, we will use the notation

$$\mathsf{A} = \begin{bmatrix} \mathbf{a} & \mathbf{b} & \mathbf{c} \end{bmatrix} \tag{A.3.1}$$

as shorthand for the matrix

$$\mathsf{A} = \begin{bmatrix} \mathbf{a} \cdot \mathbf{E}_1 & \mathbf{b} \cdot \mathbf{E}_1 & \mathbf{c} \cdot \mathbf{E}_1 \\ \mathbf{a} \cdot \mathbf{E}_2 & \mathbf{b} \cdot \mathbf{E}_2 & \mathbf{c} \cdot \mathbf{E}_2 \\ \mathbf{a} \cdot \mathbf{E}_3 & \mathbf{b} \cdot \mathbf{E}_3 & \mathbf{c} \cdot \mathbf{E}_3 \end{bmatrix}. \tag{A.3.2}$$

For future purposes it is convenient to note that the following matrix is singular:

$$\mathsf{G} = \begin{bmatrix} \mathbf{g}_1 \times \mathbf{x} & \mathbf{g}_2 \times \mathbf{x} & \mathbf{g}_3 \times \mathbf{x} \end{bmatrix}, \tag{A.3.3}$$

where $\mathbf{x}$ is any vector. The singular nature of G can be established by first noting that

$$\mathsf{G} = -\begin{bmatrix} \mathbf{x} \times \mathbf{g}_1 & \mathbf{x} \times \mathbf{g}_2 & \mathbf{x} \times \mathbf{g}_3 \end{bmatrix} = -\begin{bmatrix} \mathrm{Skew}(\mathbf{x}) \end{bmatrix}\begin{bmatrix} \mathbf{g}_1 & \mathbf{g}_2 & \mathbf{g}_3 \end{bmatrix}. \tag{A.3.4}$$

We recall Sylvester's rank inequality, if A is an $m \times n$ matrix and B is an $n \times k$ matrix, then

$$\mathrm{rank}(\mathsf{A}) + \mathrm{rank}(\mathsf{B}) - n \leq \mathrm{rank}(\mathsf{AB}). \tag{A.3.5}$$

Knowing that $\mathrm{rank}([\mathrm{Skew}(\mathbf{x})]) = 2$, the rank inequality allows us to conclude that $\mathrm{rank}(\mathsf{G}) = 2$.

We note that the null space of G is the vector

$$\mathrm{null}(\mathsf{G}) = [\mathbf{g}_1 \; \mathbf{g}_2 \; \mathbf{g}_3]^{-1}\mathbf{x} = [\mathbf{g}^1 \; \mathbf{g}^2 \; \mathbf{g}^3]^T\mathbf{x}, \tag{A.3.6}$$

where $\{\mathbf{g}^1 \; \mathbf{g}^2 \; \mathbf{g}^3\}$ is the dual Euler basis. In computing (A.3.6), we assumed that the matrix $[\mathbf{g}_1 \; \mathbf{g}_2 \; \mathbf{g}_3]$ is invertible which is valid when $\vartheta \neq 0, \pi$.

Appendix B

Representations for the Components of S for the Holonomy of the Rolling Sphere

The holonomy of the rolling sphere moving in such a manner that its center of mass traces a rectangular path is discussed in Chapter 2. The holonomy of the sphere can be described by a rotation $\mathbf{S}$.

B.1 Expressions for the Components S_{ik}

The components

$$S_{ik} = \left(\hat{\mathbf{S}} \left(\vartheta, \varphi_1, \varphi_2, \mathbf{A}_1, \mathbf{A}_2, \circlearrowleft \right) \mathbf{A}_k \right) \cdot \mathbf{A}_i \tag{B.1.1}$$

have the following representations:

$$\begin{bmatrix} S_{11} & S_{12} & S_{13} \\ S_{21} & S_{22} & S_{23} \\ S_{31} & S_{32} & S_{33} \end{bmatrix} = \begin{bmatrix} \cos\left(\varphi_{21}\right) & 0 & \sin\left(\varphi_{21}\right) \\ 0 & 1 & 0 \\ -\sin\left(\varphi_{21}\right) & 0 & \cos\left(\varphi_{21}\right) \end{bmatrix} \begin{bmatrix} M_{11} & M_{21} & M_{31} \\ M_{12} & M_{22} & M_{32} \\ M_{13} & M_{23} & M_{33} \end{bmatrix} \begin{bmatrix} \cos\left(\varphi_1\right) & 0 & \sin\left(\varphi_1\right) \\ 0 & 1 & 0 \\ -\sin\left(\varphi_1\right) & 0 & \cos\left(\varphi_1\right) \end{bmatrix},$$

$$\tag{B.1.2}$$

where

$$\varphi_{21} = \varphi_2 - \varphi_1,$$

$$\begin{bmatrix} M_{11} & M_{12} & M_{13} \\ M_{21} & M_{22} & M_{23} \\ M_{31} & M_{32} & M_{33} \end{bmatrix} = \begin{bmatrix} cz & sysz & -cysz \\ -sysz & cy^2 + czsx^2 & (1 - cz)\,cysy \\ cysz & (1 - cz)\,cysy & cy^2cz + sy^2 \end{bmatrix},$$

$$cy = \cos\left(\vartheta\right), \qquad sy = \sin\left(\vartheta\right),$$

$$cz = \cos\left(\varphi_2\right), \qquad sz = \sin\left(\varphi_2\right). \tag{B.1.3}$$

It is straightforward to show by transposing the matrix products in (B.1.2) that the companion expressions for the components of $\hat{\mathbf{S}}\left(\vartheta, \varphi_1, \varphi_2, \mathbf{A}_1, \mathbf{A}_2, \circlearrowleft\right)$ are S_{ki}.

Appendix C

Computing the Three Angular Variables Given an Axis and Angle of Rotation

A desired holonomy of the sphere circumnavigating a rectangular path can be specified by an angle of rotation ψ and axis of rotation $\mathbf{s}$. The corresponding rectangular path has three parameters: $(\vartheta, \varphi_1, \varphi_2)$. The question we seek to answer is as follows: given any pair $(\psi, \mathbf{s})$ how do we solve equations (2.4.6) and (2.4.7) for the corresponding triple $(\vartheta, \varphi_1, \varphi_2)$?

C.1   The Simplest Cases

It is helpful to consider the case $\varphi_2 = (2n - 1)\pi$. This case was discussed previously in Section 2.4 and produces a holonomy $\mathbf{R}(2\vartheta, \mathbf{A}_r)$ where $\mathbf{A}_r$ is a function of φ_2 (cf. $(2.4.9)_1$). A second case of interest is $\varphi_2 = 2n\pi$. This value of φ_2 results in the sphere returning to its original orientation following a circumnavigation of the rectangular path. In the sequel, we assume that $\varphi_2 \neq n\pi$.

C.2   The Case Where $\varphi_2 \neq n\pi$

Returning to our development of a scheme to compute a rectangular path for a given holonomy, we first manipulate the four scalar equations (2.4.6) to establish the following equation for φ_1 as a function of φ_2:

$$\tan(\varphi_1) = \frac{\tan\left(\frac{\varphi_2}{2}\right) - \left(\frac{\mathbf{s} \cdot \mathbf{A}_1}{\mathbf{s} \cdot \mathbf{A}_3}\right)}{1 + \left(\frac{\mathbf{s} \cdot \mathbf{A}_1}{\mathbf{s} \cdot \mathbf{A}_3}\right) \tan\left(\frac{\varphi_2}{2}\right)} \tag{C.2.1}$$

We seek solutions φ_1 to (C.2.1) where $\varphi_2 \in [0, 3\pi]$, and $\varphi_1 \leq \varphi_2$. The remaining three equations from (2.4.6) provide three equations for the two unknowns ϑ and φ_2:

$$a = \frac{1}{2}\left(1 + \cos(\vartheta) + \cos(\varphi_2) - \cos(\vartheta)\cos(\varphi_2)\right),$$

$$b = \frac{1}{2}\left(1 - \cos(\vartheta)\right)\sin(\varphi_2),$$

$$c = \sin^2(\vartheta)\sin^2\left(\frac{\varphi_2}{2}\right), \tag{C.2.2}$$

where the variables a, b, and c, are prescribed by the chosen values of ψ and $\mathbf{s}$:

$$a = \cos\left(\frac{\psi}{2}\right),$$

$$b = \sin\left(\frac{\psi}{2}\right)(\mathbf{s} \cdot \mathbf{A}_2),$$

$$c = \sin^2\left(\frac{\psi}{2}\right)\left((\mathbf{s} \cdot \mathbf{A}_1)^2 + (\mathbf{s} \cdot \mathbf{A}_3)^2\right). \tag{C.2.3}$$

We make use of the observation that if φ_2 is a solution to (C.2.2) then $\varphi_2 + 2\pi$ is also a solution to these equations. Next, we substitute (C.2.2)$_{2,3}$ into (C.2.2)$_1$ to arrive at a single equation for φ_2:

$$2a = f(\varphi_2, b, c), \tag{C.2.4}$$

where the function f is

$$f = 1 \pm \sqrt{1 - \frac{c}{\sin^2\left(\frac{\varphi_2}{2}\right)}} + 2b\frac{\cos(\varphi_2)}{\sin(\varphi_2)}. \tag{C.2.5}$$

The domain of f is restricted as follows:

$$\varphi_2 \neq n\pi, \qquad 1 - \frac{c}{\sin^2\left(\frac{\varphi_2}{2}\right)} \geq 0. \tag{C.2.6}$$

That is,

$$\varphi_2 \in [2\sin^{-1}(\sqrt{c}), \pi) \cup (\pi, 2\pi - 2\sin^{-1}(\sqrt{c})] \cup [2\pi + 2\sin^{-1}(\sqrt{c}), 3\pi). \tag{C.2.7}$$

We are now in a position to seek numerical solutions φ_2 to (C.2.4) using the Matlab routine vpasolve().[1]

Once we have found all possible solutions of (C.2.4) for a prescribed holonomy, we use (C.2.2)$_1$ to find the corresponding values of ϑ:

$$\cos(\vartheta) = \frac{2a - 1 - \cos(\varphi_2)}{1 - \cos(\varphi_2)}, \tag{C.2.8}$$

---

[1]The code used to compute the solutions can be found in the supplemental materials for Chapter 2.

We disregard any φ_2 values that do not yield real values of ϑ. If the solution ϑ to (C.2.8) is negative, then we add 2π to the solution and make it positive. After we have assembled all the possible solution candidates (ϑ, φ_2), we substitute them into $(C.2.2)_{2,3}$ and eliminate any solution pairs that do not satisfy both equations. Lastly, we use (C.2.1) to calculate φ_1 and eliminate any solutions that do not satisfy the original equations (2.4.6).

C.3 Summary

In summary, we first express the three equations (C.2.2) in the two unknowns ϑ and φ_2 as a single equation for φ_2, i.e., (C.2.4). We then solve (C.2.4) numerically and obtain the corresponding ϑ values from $(C.2.2)_1$ and φ_1 values from equation (C.2.1). We also ensure that our results satisfy (2.4.6). Thus, we find the parameters $(\vartheta, \varphi_1, \varphi_2)$ of a rectangle that yield a desired rotation $\mathbf{R}(\psi, \mathbf{s})$ of a rolling sphere after it has circumnavigated the rectangle.

Appendix D

The Frobenius Integrability Criterion Applied to a Rolling Cylinder

The cylindrical rigid body has six degrees of freedom and the motion of the rolling cylinder is subject to the three constraints $\mathbf{v}_P = \mathbf{0}$. While one of these constraints $(\mathbf{v}_P \cdot \mathbf{E}_3)$ is integrable, it is not clear if the entire system of constraints is integrable. To explore this issue, we use the Frobenius integrability criterion [24] (cf. [23, 29, 54]).

D.1 Preliminaries

Each of the three constraints $\Pi_k = 0$ (cf. (3.2.2)) on the rolling cylinder can be expressed in a canonical form $\Pi = 0$ where

$$\Pi = \mathbf{f} \cdot \bar{\mathbf{v}} + \mathbf{h} \cdot \boldsymbol{\omega}. \tag{D.1.1}$$

After defining the 6 coordinates,

$$q^i = x_i, \quad q^4 = \psi, \quad q^5 = \vartheta, \quad q^6 = \varphi, \tag{D.1.2}$$

where $i = 1, 2, 3$, we compute the following representations for the three constraint functions:

$$\Pi_i = \sum_{K=1}^{6} W_{i_K} \dot{q}^K. \tag{D.1.3}$$

Referring to (3.2.5), we find that

$$\mathsf{W} = \begin{bmatrix} 1 & 0 & 0 & \cos(\psi) f_1 & -\sin(\psi) f_2 & r\cos(\psi) \\ 0 & 1 & 0 & \sin(\psi) f_1 & \cos(\psi) f_2 & r\sin(\psi) \\ 0 & 0 & 1 & 0 & -f_1 & 0 \end{bmatrix}. \tag{D.1.4}$$

We now define the components of three skew-symmetric matrices:

$$S_{L,K}^\Gamma = \frac{\partial W_{\Gamma_L}}{\partial q^K} - \frac{\partial W_{\Gamma_K}}{\partial q^L}, \qquad (K, L = 1, \ldots, 6, \Gamma = 1, \ldots, 3). \tag{D.1.5}$$

There remains to define three vectors:

$$\mathsf{a} = \begin{bmatrix} a_1 \\ \vdots \\ a_6 \end{bmatrix}, \quad \mathsf{b} = \begin{bmatrix} b_1 \\ \vdots \\ b_6 \end{bmatrix}, \quad \mathsf{y} = \begin{bmatrix} y_1 \\ \vdots \\ y_6 \end{bmatrix}. \tag{D.1.6}$$

Frobenius' necessary and sufficient conditions for a system of 3 constraints, $\Pi_1 = 0, \ldots, \Pi_3 = 0$ to be integrable require the following equations to hold:

$$a^T \left(S^\Gamma b \right) = 0 \qquad (\Gamma = 1, \ldots, 3) \tag{D.1.7}$$

for all values of the variables $q^1, \ldots, q^6$ and for all distinct solutions a and b to the equation

$$W\mathsf{y} = 0. \tag{D.1.8}$$

That is, the six-dimensional vectors a and b lie in the null space of W.

D.2 Application of the Integrability Criterion

To apply Frobenuis' integrability criterion, we now compute S_1, S_2, and S_3:

$$\mathsf{S}^1 = \begin{bmatrix} \mathsf{O}_{3\times3} & \mathsf{O}_{3\times3} \\ \mathsf{O}_{3\times3} & \mathsf{E}^1 \end{bmatrix}, \quad \mathsf{E}^1 = \begin{bmatrix} 0 & 0 & r\sin(\psi) \\ 0 & 0 & 0 \\ -r\sin(\psi) & 0 & 0 \end{bmatrix},$$

$$\mathsf{S}_2 = \begin{bmatrix} \mathsf{O}_{3\times3} & \mathsf{O}_{3\times3} \\ \mathsf{O}_{3\times3} & \mathsf{E}^2 \end{bmatrix}, \quad \mathsf{E}^2 = \begin{bmatrix} 0 & 0 & -r\cos(\psi) \\ 0 & 0 & 0 \\ r\cos(\psi) & 0 & 0 \end{bmatrix}, \tag{D.2.1}$$

$$\mathsf{S}_3 = \mathsf{O}_{6\times6},$$

where $\mathsf{O}_{n\times n}$ is the $n \times n$ null matrix. The 3-dimensional null space of W is spanned by the vectors

$$\mathsf{y}_1 = \begin{bmatrix} -\cos(\psi) f_1 \\ -\sin(\psi) f_1 \\ 0 \\ 1 \\ 0 \\ 0 \end{bmatrix}, \quad \mathsf{y}_2 = \begin{bmatrix} \sin(\psi) f_2 \\ -\cos(\psi) f_2 \\ f_1 \\ 0 \\ 1 \\ 0 \end{bmatrix}, \quad \mathsf{y}_3 = \begin{bmatrix} -r\cos(\psi) \\ -r\sin(\psi) \\ 0 \\ 0 \\ 0 \\ 1 \end{bmatrix}. \tag{D.2.2}$$

Finally, applying Frobenius' criterion, we compute all unique combinations

$$\mathsf{a}^T \left(\mathsf{S}^B \mathsf{b} \right) = 0, \quad (B = 1, \ldots, 3) \tag{D.2.3}$$

for all distinct solutions a and b of $\mathsf{Wy} = 0$ except for

$$
\begin{aligned}
\mathsf{y}_1^T \left(\mathsf{S}^1 \mathsf{y}_3 \right) &= r \sin \left(\psi \right), \\
\mathsf{y}_1^T \left(\mathsf{S}^2 \mathsf{y}_3 \right) &= -r \cos \left(\psi \right).
\end{aligned}
\tag{D.2.4}
$$

In conclusion, the application of Frobenius' criterion has shown that while the constraint Π_3 in equation (3.2.2) is integrable, the system of three constraints is non-integrable.

Appendix E

Contact Detection between Two Cylinders

Given the dimensions, position, and orientation of the pair of cylinders such as the pair shown in Figure 3.13, we seek to determine whether the cylinders penetrate (not a valid configuration), touch at one point, or are apart from each other. The resulting characterization of the gap distance d between the cylinders is necessary for contact detection in simulations.

E.1 Preliminaries

For contact detection between the cylinders, we consider the following representations for the position vectors of points $\mathbf{x}_I$ and $\mathbf{x}_{II}$ of material points on the axes of the cylinders I and II, respectively:

$$\begin{aligned}
\mathbf{x}_I &= \bar{\mathbf{x}}_I + m_I \mathbf{e}_3, \\
\mathbf{x}_{II} &= \bar{\mathbf{x}}_{II} + n_{II} \mathbf{e}_3,
\end{aligned} \tag{E.1.1}$$

where

$$m \in \left[-\frac{h_1}{2}, \frac{h_1}{2} \right] \quad \text{and} \quad n \in \left[-\frac{h_2}{2}, \frac{h_2}{2} \right] \tag{E.1.2}$$

are coordinates.

E.2 A Minimization Problem

The distance between two points on the axes of the cylinders is

$$\begin{aligned}
d &= \| \mathbf{x}_{II} - \mathbf{x}_I \|, \\
&= \| \bar{\mathbf{x}}_{II} + n_{II} \mathbf{e}_3 - \bar{\mathbf{x}}_I - m_I \mathbf{e}_3 \|.
\end{aligned} \tag{E.2.1}$$

We seek to find m^* and n^* corresponding to the points $\mathbf{x}_I^*$ and $\mathbf{x}_{II}^*$ for which the distance d is minimized. The relative position vectors of these points are normal to the axes of both cylinders:

$$(\mathbf{x}_I^* - \mathbf{x}_{II}^*) \cdot {}_I\mathbf{e}_3 = 0,$$
$$(\mathbf{x}_I^* - \mathbf{x}_{II}^*) \cdot {}_{II}\mathbf{e}_3 = 0. \tag{E.2.2}$$

With the help of (E.1.1), we can express the pair of equations (E.2.2) in the form

$$\mathsf{H}\mathsf{h} = \mathsf{k}, \tag{E.2.3}$$

where

$$\mathsf{H} = \begin{bmatrix} 1 & -{}_{II}\mathbf{e}_3 \cdot {}_I\mathbf{e}_3 \\ -{}_{II}\mathbf{e}_3 \cdot {}_I\mathbf{e}_3 & 1 \end{bmatrix}, \qquad \mathsf{h} = \begin{bmatrix} m^* \\ n^* \end{bmatrix}, \qquad \mathsf{k} = \begin{bmatrix} (\bar{\mathbf{x}}_{II} - \bar{\mathbf{x}}_I) \cdot {}_I\mathbf{e}_3 \\ (\bar{\mathbf{x}}_I - \bar{\mathbf{x}}_{II}) \cdot {}_{II}\mathbf{e}_3 \end{bmatrix}. \tag{E.2.4}$$

For a given configuration of the cylinders, H and k are known. We seek solutions h to the equation $\mathsf{H}\mathsf{h} = \mathsf{k}$. Notice that the matrix A is singular when the two cylinders are parallel, i.e., when ${}_{II}\mathbf{e}_3 \cdot {}_I\mathbf{e}_3 = \pm 1$ and there is a continuous line of contact points. In our computational algorithm to detect the contact points, we also compute the derivatives of h in order to explore what occurs at later instances of time:

$$\dot{\mathsf{h}} = \mathsf{H}^{-1}\left(\dot{\mathsf{k}} - \dot{\mathsf{H}}\mathsf{h}\right),$$
$$\ddot{\mathsf{h}} = \mathsf{H}^{-1}\left(\ddot{\mathsf{k}} - \ddot{\mathsf{H}}\mathsf{h} - 2\dot{\mathsf{H}}\dot{\mathsf{h}}\right). \tag{E.2.5}$$

If equation (E.1.2) is satisfied by the solutions to (E.2.3), then if

$$\begin{cases} d < r_1 + r_2 & \text{the cylinders penetrate, not a valid configuration} \\ d = r_1 + r_2 & \text{the cylinders touch,} \\ d > r_1 + r_2 & \text{the cylinders are not in contact.} \end{cases} \tag{E.2.6}$$

Once m^* and n^* have been computed, the relative position vectors of the contact points can be found:

$$\boldsymbol{\pi}_{P_3} = m\,{}_I\mathbf{e}_3 + r_1\mathbf{u},$$
$$\boldsymbol{\pi}_{P_4} = n\,{}_{II}\mathbf{e}_3 - r_2\mathbf{u}, \tag{E.2.7}$$

where the unit vector $\mathbf{u}$ is normal to the axes of both cylinders:

$$\mathbf{u} = \frac{\mathbf{x}_{II} - \mathbf{x}_I}{\|\mathbf{x}_{II} - \mathbf{x}_I\|}. \tag{E.2.8}$$

As shown in Figure 3.13, the vector $\mathbf{u} = \pm\mathbf{n}$, has the representations

$$\mathbf{u} = \cos\left(\chi_1\right){}_I\mathbf{e}_1 + \sin\left(\chi_1\right){}_I\mathbf{e}_2$$
$$= \cos\left(\chi_2\right){}_{II}\mathbf{e}_1 + \sin\left(\chi_2\right){}_{II}\mathbf{e}_2. \tag{E.2.9}$$

In computing the solution of the contact problem and applications of the Frobenius integrability criterion, the variables m, n, χ_1, χ_2 should be considered as functions of the 12 coordinates ${}_Ix_k$, ${}_{II}x_k$, ψ_1, ϑ_1, φ_1, ψ_2, ϑ_2, and φ_2.

E.3 The Three Contacts

Referring to Figure 3.13, the two other contact detections of interest are the instantaneous points of contact of each cylinder with the horizontal plane: P_1 and P_4. The normal components of all three constraint velocities $\mathbf{v}_1 = \mathbf{0}$, $\mathbf{v}_2 = \mathbf{0}$, and $\mathbf{v}_3 - \mathbf{v}_4 = \mathbf{0}$ are holonomic.[1] Thus, we can write the gap distances for the two cylinder-ground contact and for the cylinder-cylinder contact respectively as

$$
\begin{aligned}
g_{N1} &= (\bar{\mathbf{x}}_I + \boldsymbol{\pi}_{P_1}) \cdot \mathbf{E}_3, \\
g_{N2} &= (\bar{\mathbf{x}}_{II} + \boldsymbol{\pi}_{P_2}) \cdot \mathbf{E}_3, \\
g_{N3} &= \|\mathbf{x}_3 - \mathbf{x}_4\| - (r_1 + r_2) = (\mathbf{x}_3 - \mathbf{x}_4) \cdot \mathbf{n} - (r_1 + r_2).
\end{aligned}
\tag{E.3.1}
$$

---

[1]According to Papastavridis [62, Section 2.2 p. 249] every condition expressing the direct contact of two rigid bodies, or the contact of one of its bodies with a foreign obstacle (environment) that is either fixed or has known motion (i.e., its position coordinates are known functions of time only), results in a holonomic equation of motion, and the corresponding contact forces are the reactions of that constraint.

Appendix F

Frobenius Integrability Criterion Applied to a Pair of Rolling Cylinders

We consider a pair of cylinders each of which rolls with one point in contact with a horizontal surface. The cylinders are also in mutual contact at a single point. Our interest lies in the case where there is sufficient static friction such that the contact between the cylinders is also one of rolling. We seek to apply Frobenius integrability criterion to determine if the set of 9 rolling constraints are integrable. In the course of our investigation, we also find that they are not independent.

F.1   Preliminaries

Referring to (3.5.3), (3.5.5), and (3.5.9), the system is subject to 9 constraints:

$$\Pi_\Gamma = 0, \qquad (\Gamma = 0, \dots, 9), \tag{F.1.1}$$

where

$$\begin{aligned}
\Pi_k &= \mathbf{v}_1 \cdot \mathbf{E}_k, \quad (k = 1, 2, 3), \\
\Pi_{k+3} &= \mathbf{v}_2 \cdot \mathbf{E}_k, \\
\Pi_{k+6} &= (\mathbf{v}_3 - \mathbf{v}_4) \cdot \mathbf{E}_k.
\end{aligned} \tag{F.1.2}$$

The cylinder has six degrees of freedom and the motion of the rolling cylinder is subject to the three constraints $\mathbf{v}_P = \mathbf{0}$. While one of these constraints $(\mathbf{v}_P \cdot \mathbf{E}_3)$ is integrable, it is not clear if the entire system of constraints is integrable. To explore this issue, we use the Frobenius integrability criterion [24] (cf. [23, 29, 54]).

F.2 Expressions for the Constraint Matrix W

We recall the definitions for the 12 coordinates:

$$q^i = x_{I_i}, \quad q^4 = \psi_1, \quad q^5 = \vartheta_1, \quad q^6 = \varphi_1,$$
$$q^{i+6} = x_{II_i}, \quad q^{10} = \psi_2, \quad q^{11} = \vartheta_2, \quad q^{12} = \varphi_2, \tag{F.2.1}$$

where $i = 1, 2, 3$. Each of the constraint functions Π_Γ in (F.1.2) are linear functions of the velocities:

$$\Pi_\Gamma = \sum_{K=1}^{12} W_{\Gamma_K} \dot{q}^K. \tag{F.2.2}$$

With some additional work, we find that the matrix W has the following block structure:

$$W = \begin{bmatrix} W_{1_1} & \cdots & W_{1_{12}} \\ \vdots & & \vdots \\ W_{9_1} & \cdots & W_{9_{12}} \end{bmatrix} = \begin{bmatrix} I_{3\times3} & A & O_{3\times3} & O_{3\times3} \\ O_{3\times3} & O_{3\times3} & I_{3\times3} & B \\ I_{3\times3} & C & -I_{3\times3} & -D \end{bmatrix}. \tag{F.2.3}$$

In the expression for the matrix W, $I_{3\times3}$ is the 3×3 identity matrix and

$$
\begin{aligned}
A &= \begin{bmatrix} \mathbf{E}_3 \times \boldsymbol{\pi}_{P_1} & {}_I\mathbf{e}'_1 \times \boldsymbol{\pi}_{P_1} & {}_I\mathbf{e}_3 \times \boldsymbol{\pi}_{P_1} \end{bmatrix} \\
&= \begin{bmatrix} -\boldsymbol{\pi}_{P_1} \cdot \mathbf{E}_2 & (\boldsymbol{\pi}_{P_1} \cdot \mathbf{E}_3)\sin(\psi_1) & -r_1 \cos(\psi_1) \\ \boldsymbol{\pi}_{P_1} \cdot \mathbf{E}_1 & -(\boldsymbol{\pi}_{P_1} \cdot \mathbf{E}_3)\cos(\psi_1) & -r_1 \sin(\psi_1) \\ 0 & \boldsymbol{\pi}_{P_1} \cdot {}_I\mathbf{e}'_2 & 0 \end{bmatrix}, \\
B &= \begin{bmatrix} \mathbf{E}_3 \times \boldsymbol{\pi}_{P_2} & {}_{II}\mathbf{e}'_1 \times \boldsymbol{\pi}_{P_2} & {}_{II}\mathbf{e}_3 \times \boldsymbol{\pi}_{P_2} \end{bmatrix}, \\
C &= \begin{bmatrix} \mathbf{E}_3 \times \boldsymbol{\pi}_{P_3} & {}_I\mathbf{e}'_1 \times \boldsymbol{\pi}_{P_3} & {}_I\mathbf{e}_3 \times \boldsymbol{\pi}_{P_3} \end{bmatrix}, \\
D &= \begin{bmatrix} \mathbf{E}_3 \times \boldsymbol{\pi}_{P_4} & {}_{II}\mathbf{e}'_1 \times \boldsymbol{\pi}_{P_4} & {}_{II}\mathbf{e}_3 \times \boldsymbol{\pi}_{P_4} \end{bmatrix}.
\end{aligned} \tag{F.2.4}
$$

Observe that each of the matrices A, B, C, D, and their linear combinations are of the form (A.3.3) and are thus singular. To determine the rank of W, we perform the following matrix row manipulations.

$$W = \begin{bmatrix} I & A & 0 & 0 \\ 0 & 0 & I & B \\ I & C & -I & -D \end{bmatrix} \rightarrow \begin{bmatrix} I & A & 0 & 0 \\ 0 & 0 & I & B \\ 0 & C-A & 0 & B-D \end{bmatrix}, \tag{F.2.5}$$

and observe that $C - A$ and $B - D$ are also of the form of equation (A.3.3). The rows of $[0 \ C - A \ 0 \ B - D]$ can be manipulated in a similar manner to show that the rank of $[0 \ C - A \ 0 \ B - D]$ is 2 and thus the rank of W is 8. We conclude from this result that only eight of the nine constraints $\Pi_1 = 0, \ldots, \Pi_9 = 0$ are independent.

We note that in the singular case where $C - A = 0$ and $B - D = 0$ corresponding to when the contact points between the two cylinders coincide with the contact points of each cylinder with the ground, $\mathrm{rank}(W)$ reduces to 6.

The null space of W is spanned by the vector w_n:

$$\mathsf{w}_n = \begin{bmatrix} -\mathsf{Ay} \\ \mathsf{y} \\ -\mathsf{Bz} \\ \mathsf{z} \end{bmatrix}, \tag{F.2.6}$$

where $\mathsf{y} = [y_1, y_2, y_3]^T$ and $\mathsf{z} = [z_1, z_2, z_3]^T$ are 3-dimensional arrays whose components satisfy the identity

$$(\mathsf{C} - \mathsf{A})\,\mathsf{y} + (\mathsf{D} - \mathsf{B})\,\mathsf{z} = 0. \tag{F.2.7}$$

With the assistance of (A.3.4) and (A.3.6), we obtain the following solutions to equation (F.2.7):

$$\begin{aligned} \mathsf{y} &= [_I\mathbf{g}^1 \ _I\mathbf{g}^2 \ _I\mathbf{g}^3]^T[\boldsymbol{\pi}_{P_2} - \boldsymbol{\pi}_{P_4}], \\ \mathsf{z} &= [_{II}\mathbf{g}^1 \ _{II}\mathbf{g}^2 \ _{II}\mathbf{g}^3]^T[\boldsymbol{\pi}_{P_1} - \boldsymbol{\pi}_{P_3}]. \end{aligned} \tag{F.2.8}$$

The resulting expression for (F.2.6),

$$\mathsf{w}_n = \begin{bmatrix} [\boldsymbol{\pi}_{P_1} \times (\boldsymbol{\pi}_{P_2} - \boldsymbol{\pi}_{P_4})] \\ [_I\mathbf{g}^1 \ _I\mathbf{g}^2 \ _I\mathbf{g}^3]^T[\boldsymbol{\pi}_{P_2} - \boldsymbol{\pi}_{P_4}] \\ [\boldsymbol{\pi}_{P_2} \times (\boldsymbol{\pi}_{P_1} - \boldsymbol{\pi}_{P_3})] \\ [_{II}\mathbf{g}^1 \ _{II}\mathbf{g}^2 \ _{II}\mathbf{g}^3]^T[\boldsymbol{\pi}_{P_1} - \boldsymbol{\pi}_{P_3}] \end{bmatrix}, \tag{F.2.9}$$

has no obvious interpretation. As a result, it is challenging to reduce the nine constraint equations (F.1.1) to a single set of eight independent constraints.

F.3   Comments on Constraint Forces

The constraint forces and constraint moments associated with the nine constraints can be prescribed using a standard procedure (cf. [57]). Thus, the constraints at P_1 will be enforced by a pair of static Coulomb friction forces and a normal force acting at P_1:

$$\mathbf{F}_{c_1} = F_{f_1}\mathbf{E}_1 + F_{f_2}\mathbf{E}_2 + N_1\mathbf{E}_3 \text{ acting at } P_1. \tag{F.3.1}$$

Similarly, the constraints at P_2 will be enforced by a pair of static Coulomb friction forces and a normal force acting at P_2:

$$\mathbf{F}_{c_2} = F_{f_3}\mathbf{E}_1 + F_{f_4}\mathbf{E}_2 + N_2\mathbf{E}_3 \text{ acting at } P_2. \tag{F.3.2}$$

For the mutual contact, the constraints are enforced by the following set of friction and normal forces:

$$\begin{aligned} \mathbf{F}_{c_3} &= F_{f_5 I}\mathbf{e}_3 + F_{f_6 II}\mathbf{e}_3 + N_3\mathbf{n} \text{ acting at } P_3, \\ \mathbf{F}_{c_4} &= -\mathbf{F}_{c_3} \text{ acting at } P_4. \end{aligned} \tag{F.3.3}$$

The components $F_{f_1}, \ldots F_{f_6}$, N_1, N_2, and N_3 can be considered as Lagrange multipliers enforcing the nine constraints $\Pi_1 = 0, \ldots, \Pi_9 = 0$. However, because these constraints are not independent, one of the multipliers is redundant. Determining the redundant multiplier is non-trivial.

F.4 Expressions for the Skew-Symmetric Matrices S^Γ

We recall from (D.1.5) that a set of 9 skew-symmetric matrices S^Γ need to be examined. The components of S^Γ have the following representation:

$$S_{L,K}^\Gamma = \frac{\partial W_{\Gamma_L}}{\partial q^K} - \frac{\partial W_{\Gamma_K}}{\partial q^L}, \qquad (K, L = 1, \ldots, 12, \Gamma = 1, \ldots, 9). \tag{F.4.1}$$

Four of the nine skew-symmetric matrices have only one distinct element and two of the matrices are identically zero:

$$\mathsf{S}^1 = \begin{bmatrix} \mathsf{O}_{3\times3} & \mathsf{O}_{3\times3} & \mathsf{O}_{3\times3} & \mathsf{O}_{3\times3} \\ \mathsf{O}_{3\times3} & -\mathsf{E}^1 & \mathsf{O}_{3\times3} & \mathsf{O}_{3\times3} \\ \mathsf{O}_{3\times3} & \mathsf{O}_{3\times3} & \mathsf{O}_{3\times3} & \mathsf{O}_{3\times3} \\ \mathsf{O}_{3\times3} & \mathsf{O}_{3\times3} & \mathsf{O}_{3\times3} & \mathsf{O}_{3\times3} \end{bmatrix}, \qquad \mathsf{E}^1 = \begin{bmatrix} 0 & 0 & r_1 \sin(_I\psi) \\ 0 & 0 & 0 \\ -r_1 \sin(_I\psi) & 0 & 0 \end{bmatrix}, \tag{F.4.2}$$

$$\mathsf{S}^2 = \begin{bmatrix} \mathsf{O}_{3\times3} & \mathsf{O}_{3\times3} & \mathsf{O}_{3\times3} & \mathsf{O}_{3\times3} \\ \mathsf{O}_{3\times3} & -\mathsf{E}^2 & \mathsf{O}_{3\times3} & \mathsf{O}_{3\times3} \\ \mathsf{O}_{3\times3} & \mathsf{O}_{3\times3} & \mathsf{O}_{3\times3} & \mathsf{O}_{3\times3} \\ \mathsf{O}_{3\times3} & \mathsf{O}_{3\times3} & \mathsf{O}_{3\times3} & \mathsf{O}_{3\times3} \end{bmatrix}, \qquad \mathsf{E}^2 = \begin{bmatrix} 0 & 0 & -r_1 \cos(_I\psi) \\ 0 & 0 & 0 \\ r_1 \cos(_I\psi) & 0 & 0 \end{bmatrix}, \tag{F.4.3}$$

$$\mathsf{S}^3 = \mathsf{O}_{12\times12}, \tag{F.4.4}$$

and

$$\mathsf{S}^4 = \begin{bmatrix} \mathsf{O}_{3\times3} & \mathsf{O}_{3\times3} & \mathsf{O}_{3\times3} & \mathsf{O}_{3\times3} \\ \mathsf{O}_{3\times3} & \mathsf{O}_{3\times3} & \mathsf{O}_{3\times3} & \mathsf{O}_{3\times3} \\ \mathsf{O}_{3\times3} & \mathsf{O}_{3\times3} & \mathsf{O}_{3\times3} & \mathsf{O}_{3\times3} \\ \mathsf{O}_{3\times3} & \mathsf{O}_{3\times3} & \mathsf{O}_{3\times3} & \mathsf{F}^4 \end{bmatrix}, \qquad \mathsf{F}^4 = \begin{bmatrix} 0 & 0 & r_2 \sin(_{II}\psi) \\ 0 & 0 & 0 \\ -r_2 \sin(_{II}\psi) & 0 & 0 \end{bmatrix}, \tag{F.4.5}$$

$$\mathsf{S}^5 = \begin{bmatrix} \mathsf{O}_{3\times3} & \mathsf{O}_{3\times3} & \mathsf{O}_{3\times3} & \mathsf{O}_{3\times3} \\ \mathsf{O}_{3\times3} & \mathsf{O}_{3\times3} & \mathsf{O}_{3\times3} & \mathsf{O}_{3\times3} \\ \mathsf{O}_{3\times3} & \mathsf{O}_{3\times3} & \mathsf{O}_{3\times3} & \mathsf{O}_{3\times3} \\ \mathsf{O}_{3\times3} & \mathsf{O}_{3\times3} & \mathsf{O}_{3\times3} & \mathsf{F}^5 \end{bmatrix}, \qquad \mathsf{F}^5 = \begin{bmatrix} 0 & 0 & -r_2 \cos(_{II}\psi) \\ 0 & 0 & 0 \\ r_2 \cos(_{II}\psi) & 0 & 0 \end{bmatrix}, \tag{F.4.6}$$

$$\mathsf{S}^6 = \mathsf{O}_{12\times12}. \tag{F.4.7}$$

The matrix S^3 and components W_{3_L} are associated with the integrable constraint $\mathbf{v}_{P_1} \cdot \mathbf{E}_3 = 0$:

$$\frac{d}{dt}\left(_I x_3 - r_1 \sin(_I\vartheta) - \frac{h_1}{2}\cos(_I\vartheta)\right) = 0. \tag{F.4.8}$$

Similarly, the matrix S^6 and components W_{6_L} are associated with the integrable constraint $\mathbf{v}_{P_2} \cdot \mathbf{E}_3 = 0$:

$$\frac{d}{dt} \left({}_{II}x_3 - r_2 \sin({}_{II}\vartheta) - \frac{h_2}{2} \cos({}_{II}\vartheta) \right) = 0. \tag{F.4.9}$$

The remaining three matrices $\mathsf{S}^{7,8,9}$ are far more complicated because the coordinates m, n, and $\chi_{1,2}$ (cf. (E.2.7)) are non-trivial functions of $q^1, \ldots, q^{12}$:

$$\mathsf{S}^\Gamma = \begin{bmatrix} \mathsf{M}^\Gamma & \mathsf{E}^\Gamma & \mathsf{N}^\Gamma & \mathsf{F}^\Gamma \\ -\mathsf{E}^\Gamma & \mathsf{G}^\Gamma & \mathsf{H}^\Gamma & \mathsf{I}^\Gamma \\ -\mathsf{N}^\Gamma & -\mathsf{H}^\Gamma & \mathsf{J}^\Gamma & \mathsf{K}^\Gamma \\ -\mathsf{F}^\Gamma & -\mathsf{I}^\Gamma & -\mathsf{K}^\Gamma & \mathsf{L}^\Gamma \end{bmatrix}, \tag{F.4.10}$$

where $\Gamma = 7, 8, 9$ and each of the 3×3 matrices $\mathsf{E}^\Gamma, \ldots \mathsf{M}^\Gamma$ are skew-symmetric. A Matlab code that calculates the expressions S^Γ for $\Gamma = 7, 8, 9$ is available with the supplementary materials that can be found here:

https://github.com/ThH00/On-the-Dynamics-of-Transporting-Rolling-Cylinders

F.5   Application of the Integrability Criterion

The expressions of S^Γ for $\Gamma = 7, 8, 9$ are complicated, so calculating $\mathsf{a}^T \left(\mathsf{S}^B \mathsf{b} \right)$ $(B = 7, \ldots 9)$ for all 12-dimensional distinct solutions a and b of $\mathsf{W} \mathsf{y} = 0$ (cf. (D.1.7)) symbolically is not straightforward. However, we verify with a numeric example[1] that equations $\mathsf{a}^T \left(\mathsf{S}^B \mathsf{b} \right) \neq 0$ for all possible a and b. In conclusion, the system of nine constraints (F.1.1) is not integrable.

---

[1]The numerical work can be found in the supplemental materials cited previously.

Appendix G

Calculating Gap Distances and Slip Speeds

In this Appendix, essential preliminary developments pertaining to the gap distances and slip speeds between a pair of adjacent (and possibly contacting) blocks depending on their relative contact configuration.

G.1 The Four Corners

To streamline these calculations, we denote the four corners of block k by a^k, b^k, c^k, and d^k (cf. Figure 4.1(b)) where

$$
\begin{aligned}
\mathbf{r}_a^k &= \mathbf{r}^k + \frac{w^k}{2}\mathbf{e}_1^k + \frac{h^k}{2}\mathbf{e}_2^k, \\
\mathbf{r}_b^k &= \mathbf{r}^k - \frac{w^k}{2}\mathbf{e}_1^k + \frac{h^k}{2}\mathbf{e}_2^k, \\
\mathbf{r}_c^k &= \mathbf{r}^k - \frac{w^k}{2}\mathbf{e}_1^k - \frac{h^k}{2}\mathbf{e}_2^k, \\
\mathbf{r}_d^k &= \mathbf{r}^k + \frac{w^k}{2}\mathbf{e}_1^k - \frac{h^k}{2}\mathbf{e}_2^k.
\end{aligned}
\tag{G.1.1}
$$

In cases (ii) and (iii) we have $\vartheta^{k+1} > \vartheta^k$ whereas in cases (i) and (iv) $\vartheta^{k+1} < \vartheta^k$. To further differentiate these cases, we note that

$$
\begin{cases}
\mathbf{r}_d^{k+1} \cdot \mathbf{e}_1^k > \mathbf{r}_a^k \cdot \mathbf{e}_1^k & \text{for case (i)}, \\
\mathbf{r}_c^{k+1} \cdot \mathbf{e}_1^k < \mathbf{r}_b^k \cdot \mathbf{e}_1^k & \text{for case (ii)}, \\
\mathbf{r}_c^{k+1} \cdot \mathbf{e}_1^k > \mathbf{r}_b^k \cdot \mathbf{e}_1^k & \text{for case (iii)}, \\
\mathbf{r}_d^{k+1} \cdot \mathbf{e}_1^k < \mathbf{r}_a^k \cdot \mathbf{e}_1^k & \text{for case (iv)}.
\end{cases}
\tag{G.1.2}
$$

Note that in equations (G.1.2), we could have equivalently taken the dot product with $\mathbf{e}_1^{k+1}$ instead of $\mathbf{e}_1^k$. We note that in case (b) $\{\mathbf{N}^{k+1}, \mathbf{F}_f^{k+1}\}$ are applied at the corner involved:

a^k for case (i), b^k for case (ii), c^{k+1} for case (iii) and d^{k+1} for case (iv). In cases (i) and (ii), we have $\mathbf{N}^{k+1} = N^{k+1}\mathbf{e}_2^{k+1}$ and $\mathbf{F}_f^{k+1} = F_f^{k+1}\mathbf{e}_1^{k+1}$ and in cases (iii) and (iv), we have $\mathbf{N}^{k+1} = N^{k+1}\mathbf{e}_2^k$ and $\mathbf{F}_f^{k+1} = F_f^{k+1}\mathbf{e}_1^k$. The treatment of case (a) shown in Figure 4.1(a) will be discussed shortly.

G.2   The Gap Functions

We need to characterize the separation distance $g_N^k \geq 0$ between two representative blocks k and $k+1$, $k = 1, \ldots, n-1$. Equations (G.2.1) provide expressions for the minimum (normal) distance between blocks k and $k + 1$ depending on their configuration. For cases (a) and (b)$_{i-iv}$, respectively, we can write

$$
\begin{aligned}
g_N^k &= \left(\mathbf{r}^{k+1} - \mathbf{r}^k\right) \cdot \mathbf{e}_2^{k+1} - \left(\frac{h^{k+1}}{2} + \frac{h^k}{2}\right), \\
g_N^k &= \left(\mathbf{r}^{k+1} - \mathbf{r}_a^k\right) \cdot \mathbf{e}_2^{k+1} - \frac{h^{k+1}}{2}, \\
g_N^k &= \left(\mathbf{r}^{k+1} - \mathbf{r}_b^k\right) \cdot \mathbf{e}_2^{k+1} - \frac{h^{k+1}}{2}, \\
g_N^k &= \left(\mathbf{r}_c^{k+1} - \mathbf{r}_k\right) \cdot \mathbf{e}_2^k - \frac{h^k}{2}, \\
g_N^k &= \left(\mathbf{r}_d^{k+1} - \mathbf{r}^k\right) \cdot \mathbf{e}_2^k - \frac{h^k}{2}.
\end{aligned}
\tag{G.2.1}
$$

In case (a), enforcing one gap distance constraint (G.2.1)$_1$ is not sufficient to prevent blocks k and $k + 1$ from penetrating. In this situation, the additional constraint $\vartheta^k = \vartheta^{k+1}$ which provides a constraint moment is necessary. To avoid having a varying number of constraints per block depending on each block's configuration relative to its predecessor, we propose an alternative formulation which consists of two gap distance measurements between the top surface of block k and the bottom surface of block $k + 11$ for $(k = 1, \ldots, n - 1)$. This enables a computationally elegant framework that describes all cases (a) and (b) with an equal number of constraints: two normal constraints and one slip speed. We define

$$
\begin{aligned}
g_N^{2k-1} &= \begin{cases} \ell_b^k & \text{if} \quad \left(\mathbf{r}_b^k - \mathbf{r}_c^{k+1}\right) \cdot \mathbf{e}_1^{k+1} > 0, \\ \ell_c^k & \text{if} \quad \left(\mathbf{r}_b^k - \mathbf{r}_c^{k+1}\right) \cdot \mathbf{e}_1^{k+1} < 0 \end{cases} \\
g_N^{2k} &= \begin{cases} \ell_a^k & \text{if} \quad \left(\mathbf{r}_a^k - \mathbf{r}_d^{k+1}\right) \cdot \mathbf{e}_1^{k+1} < 0, \\ \ell_d^k & \text{if} \quad \left(\mathbf{r}_a^k - \mathbf{r}_d^{k+1}\right) \cdot \mathbf{e}_1^{k+1} > 0 \end{cases}
\end{aligned}
\tag{G.2.2}
$$

where, referring to Figure G.1 the distances $\ell_{\square,i}$, $\square \in \{a, b, c, d\}$ are

$$\ell_a^k = \left(\mathbf{r}_{c/d}^{k+1} - \mathbf{r}_a^k\right) \cdot \mathbf{e}_2^{k+1},$$
$$\ell_b^k = \left(\mathbf{r}_{c/d}^{k+1} - \mathbf{r}_b^k\right) \cdot \mathbf{e}_2^{k+1},$$
$$\ell_c^k = \left(\mathbf{r}_c^{k+1} - \mathbf{r}_{a/b}^k\right) \cdot \mathbf{e}_2^k,$$
$$\ell_d^k = \left(\mathbf{r}_d^{k+1} - \mathbf{r}_{a/b}^k\right) \cdot \mathbf{e}_2^k.$$

$$\text{(G.2.3)}$$
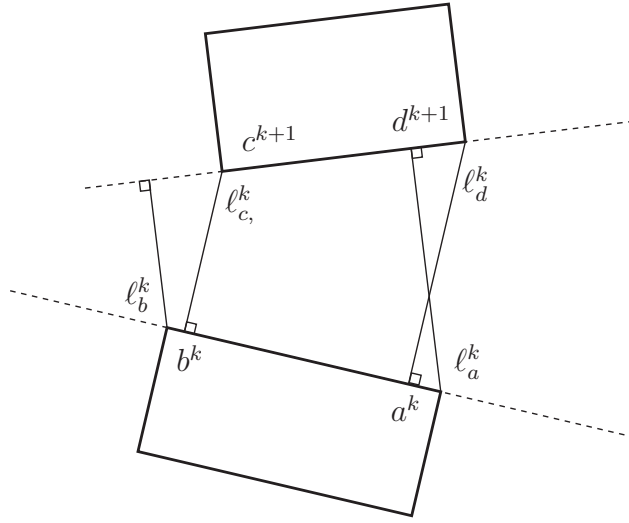
Figure G.1: Between the upper surface of block k and the lower surface of block $k + 1$, we define four length measurements: ℓ_a^k and ℓ_b^k are the minimum distances between the corners a^k and b^k respectively to the lower surface of block $k + 1$ and ℓ_c^k and ℓ_d^k are the minimum distances between the corners c^{k+1} and d^{k+1} respectively to the upper surface of block k.

In case (a), the total normal force between blocks k and $k+1$ is the sum of the constraint forces associated with both gap distance constraints. Another advantage of this constraint formulation is that the transition from (a) to (b) is seamless. If we start in case (a), whenever one corner looses contact with the surface underneath, the block transitions from case (a) to (b). The opposite happens when a block gains contact at a corner. An alternative option for enforcing the gap distance constraints might be to encode all four constraints (G.2.2) for all blocks at all times time. The drawback of this method is it yields linearly dependent force directions in case (a). In this case, we wouldn't be able to solve the system of equations of motion with constraints using Newton iterations.

Equations (G.2.2) are invalid when block $k + 1$ is no longer horizontally supported by block k. Hence, (G.2.2) are supplemented by the requirements that

$$\left(\mathbf{r}_b^k - \mathbf{r}_d^{k+1}\right) \cdot \mathbf{e}_1^{k+1} > 0 \quad \text{and} \quad \left(\mathbf{r}_a^k - \mathbf{r}_c^{k+1}\right) \cdot \mathbf{e}_1^{k+1} < 0. \qquad \text{(G.2.4)}$$

If these conditions do not hold, then the contact between blocks k and $k+1$ is lost. In this study, we limit our scope to displacements that do not lead to a change in the initial ordering of the blocks.

G.3   The Slip Speeds

We define the tangential slip speed between blocks k and $k+1$ in cases $(b)_{i-iv}$, respectively, as follows:

$$
\begin{aligned}
\gamma_F^k &= \left(\mathbf{v}_a^k - \mathbf{v}_{c/d}^{k+1}\right) \cdot \mathbf{e}_1^{k+1}, \\
\gamma_F^k &= \left(\mathbf{v}_b^k - \mathbf{v}_{c/d}^{k+1}\right) \cdot \mathbf{e}_1^{k+1}, \\
\gamma_F^k &= \left(\mathbf{v}_{a/b}^k - \mathbf{v}_c^{k+1}\right) \cdot \mathbf{e}_1^k, \\
\gamma_F^k &= \left(\mathbf{v}_{a/b}^k - \mathbf{v}_d^{k+1}\right) \cdot \mathbf{e}_1^k.
\end{aligned}
\tag{G.3.1}
$$

In our numerical computations, we select the options resulting in uniform slip speed directions. Thus, in equations (G.3.1), we choose the point on block k to always be to the right (or left) of the point on block $k+1$ so that in the case of a transition from one configuration to the next, the slip speed remains a continuous function of time. For case (a), any one of equations (G.3.1) is valid. From rigid body dynamics, the relevant velocities and corresponding slip speeds can be calculated using the identities

$$
\mathbf{v}_\square^k = \mathbf{v}^k + \boldsymbol{\omega}^k \times \left(\mathbf{r}_\square^k - \mathbf{r}^k\right), \qquad \square \in \{a, b, c, d\},
\tag{G.3.2}
$$

where $\mathbf{v}^k$ is the center of mass of block k. Notice that as blocks switch relative configurations, the slip speeds remain continuous functions of time.

Appendix H

Contact States

In Capobianco's et al.'s [14] original algorithm, each contact is associated with one normal constraint and one or more frictional constraints. For the applications in our work, each contact is associated with two normal constraints. We slightly amend Capobianco's et al. expressions in [14, Section 9] for the contact sets at the position ($\mathcal{A}^{k,1}_{i+1}$ and $\mathcal{A}^{k,2}_{i+1}$), velocity ($\mathcal{B}^{k,1}_{i+1}$ and $\mathcal{B}^{k,2}_{i+1}$), and acceleration levels ($\mathcal{C}^{k,1}_{i+1}$ and $\mathcal{C}^{k,2}_{i+1}$). The algebraic and notational complexity in [14] is considerable. In the interests of brevity, we provide sufficient details so the reader familiar with the developments and notation in [14] can follow our developments.

H.1 Sets Associated with the Normal Constraints

For the normal constraints between block k and $k + 1$ at iteration $i + 1$, the respective sets are

$$
\begin{aligned}
\mathcal{A}^1_{i+1} &= \left\{ k = 1, \ldots, n - 1 \middle|\ r\, g^{2k-1}_{N,i+1} - \hat{\kappa}^{2k-1}_{N,i+1} \leq 0 \right\}, \\
\mathcal{A}^2_{i+1} &= \left\{ k = 1, \ldots, n - 1 \middle|\ r\, g^{2k}_{N,i+1} - \hat{\kappa}^{2k}_{N,i+1} \leq 0 \right\}, \\
\mathcal{B}^1_{i+1} &= \left\{ k \in \mathcal{A}^{k,1}_{i+1} \middle|\ r\, \xi^{2k-1}_{N,i+1} - P^{2k-1}_{N,i+1} \leq 0 \right\}, \\
\mathcal{B}^2_{i+1} &= \left\{ k \in \mathcal{A}^{k,2}_{i+1} \middle|\ r\, \xi^{2k}_{N,i+1} - P^{2k}_{N,i+1} \leq 0 \right\}, \\
\mathcal{C}^1_{i+1} &= \left\{ k \in \mathcal{B}^{k,1}_{i+1} \middle|\ r\, \ddot{g}^{2k-1}_{N,i+1} - \lambda^{2k-1}_{N,i+1} \leq 0 \right\}, \\
\mathcal{C}^2_{i+1} &= \left\{ k \in \mathcal{B}^{k,2}_{i+1} \middle|\ r\, \ddot{g}^{2k}_{N,i+1} - \lambda^{2k}_{N,i+1} \leq 0 \right\}.
\end{aligned}
\tag{H.1.1}
$$

The subscript 1 (2) ornamenting $\mathcal{A}$, $\mathcal{B}$, and $\mathcal{C}$ indicates that the contact on the left (right) side of the block.

H.2   Consolidating the Sets

To describe the sets used to record stick-slip transitions at the velocity and acceleration levels for each two contact blocks, we consolidate the set

$$\mathcal{A}_{i+1} = \left\{ k = 1, \ldots, n-1 \mid k \in \mathcal{A}^1_{i+1} \text{ or } k \in \mathcal{A}^2_{i+1} \right\}, \tag{H.2.1}$$

and write

$$
\begin{aligned}
\mathcal{D}^{st}_{i+1} &= \left\{ k \in \mathcal{A}_{i+1} \mid r\, \xi^k_{F,i+1} - P^k_{F,i+1} \in C_F \left(P^{2k-1}_{N,i+1} + P^{2k}_{N,i+1} \right) \right\}, \\
\mathcal{E}^{st}_{i+1} &= \left\{ k \in D^{st}_{i+1} \mid r\, \dot{\gamma}^k_{F,i+1} - \lambda^k_{F,i+1} \in C_F \left(\lambda^{2k-1}_{N,i+1} + \lambda^{2k}_{N,i+1} \right) \right\}.
\end{aligned}
\tag{H.2.2}
$$

H.3   Notation

In (H.1.1)-(H.2.2), the following abbreviations for impulses $\hat{\kappa}_{N,i+1}$, $P_{N,i+1}$, $P_{F,i+1}$, and gap functions $\xi_{N,i+1}$ and $\xi_{F,i+1}$:

$$
\begin{aligned}
\hat{\kappa}_{N,i+1} &\approx \int_I \int_{(t_i,t]} \left((\lambda_N + \nu_N)\, d\tau + \Lambda_N d\eta \right) dt + \int_I \mu_N dt, \\
P_{N,i+1} &\approx \int_I \left((\lambda_N + \mu_N)\, dt + \Lambda_N d\eta \right), \\
P_{F,i+1} &\approx \int_I \left(\Lambda_F d\eta + \lambda_F dt \right), \\
\xi_{N,i+1} &= \dot{g}_{N,i+1} + e_N \dot{g}_{N,i}, \\
\xi_{F,i+1} &= \dot{g}_{F,i+1} + e_F \dot{g}_{F,i}.
\end{aligned}
\tag{H.3.1}
$$

In (H.3.1), g_N is the previously defined gap distance function, and $\lambda_{N,F}$ and $\Lambda_{N,F}$ are the smooth and impulsive forces associated with the normal/friction constraints respectively. We also note that dt and $d\eta$ are absolutely continuous and singular differential measures respectively, μ_N and ν_N are stabilization variables at position and velocity levels respectively for normal constraints, and e_N and e_F are normal and friction restitution coefficients respectively.

H.4   The Number of Possible Contact States Associated with a Pair of Blocks

Following the definitions in the previous sections, we now enumerate the possible contact states associated with a pair of blocks k and $k+1$. The results are presented in Tables H.1 and H.2. An entry of 1 indicates that the index k belongs to the corresponding set, while an entry of 0 indicates the opposite. We count 16 states in Table H.1, 15 of which have $k \in \mathcal{A}^k$, thus admitting 3 friction stick-slip states each according to Table H.2. Hence, the total number of possible contact states between each two consecutive blocks in 46.

$\mathcal{A}^{k,1}$	$\mathcal{A}^{k,2}$	$\mathcal{A}^k$	$\mathcal{B}^{k,1}$	$\mathcal{B}^{k,2}$	$\mathcal{C}^{k,1}$	$\mathcal{C}^{k,2}$
0	0	0	0	0	0	0
0	1	1	0	0	0	0
			0	1	0	0
					0	1
1	0	1	0	0	0	0
			1	0	0	0
					1	0
1	1	1	0	0	0	0
			0	1	0	0
					0	1
			1	0	0	0
					1	0
			1	1	0	0
					0	1
					1	0
					1	1

Table H.1: An enumeration of the possible normal contact states associated with a pair of blocks k and $k+1$. The separations correspond to the contact configurations: no contact, contact of a left corner with an edge, contact of a right corner with an edge, and edge on edge contact between blocks k and $k+1$, respectively.

$\mathcal{A}^k$	$\mathcal{D}^k$	$\mathcal{E}^k$
0	0	0
1	0	0
	1	0
		1

Table H.2: An enumeration of the possible friction contact States associated with a pair of blocks k and $k+1$. The separations correspond to the cases of no contact and contact, respectively.

Appendix I

The Painlevé Paradoxes for a Single Block

Starting in 1895, Painlevé [59, 60, 61] published a series of papers on the dynamics of a rod contacting a rough horizontal surface. Modeling the contact as one of dynamic Coulomb friction, he showed that for high coefficients of friction and specific orientations of the rod it was possible to have multiple solutions (i.e., indeterminacy) or non-existence (i.e., inconsistency) of solutions. These instances of indeterminacy and inconsistency are now known as Painlevé's paradoxes (cf. [27, 64, 69, 72] and references therein).

To complement our numerical work, we examine the presence of the paradoxes in the motion of a block with either one point P or an entire surface in contact with a rough horizontal surface. Schematic illustrations of these cases are shown in Figure I.1(a) and I.1(b), respectively.
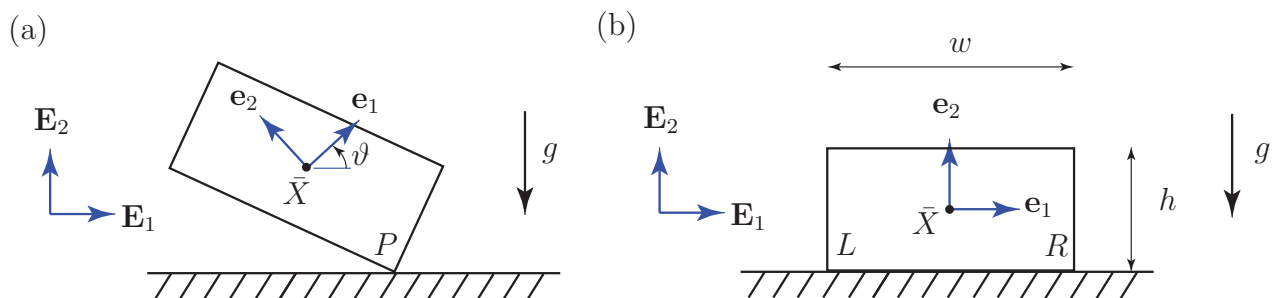

Figure I.1: A rectangular block of height h and width w in planar motion on a rough horizontal plane: (a) motion with a single point P of contact and (b) motion where an entire side of the block is in contact with the ground plane.

I.1 The Case of a Single Point of Contact

The position vector of the center of mass $\bar{X}$ has the representation $\bar{\mathbf{x}} = x\mathbf{E}_1 + y\mathbf{E}_2$. For the case where there is a single point of contact P, we conveniently choose the corotational basis $\{\mathbf{e}_1, \mathbf{e}_2, \mathbf{E}_3\}$ such that the position vector of P relative to the center of mass $\bar{X}$ has the representation

$$\boldsymbol{\pi}_P = -\ell\mathbf{e}_2, \qquad \ell = \frac{\sqrt{w^2 + h^2}}{2}. \tag{I.1.1}$$

Differentiating the relationship $\mathbf{x}_P = \bar{\mathbf{x}} + \boldsymbol{\pi}_P$ twice we find that

$$\begin{aligned}
\ddot{\mathbf{x}}_P &= \ddot{x}_P\mathbf{E}_1 + \ddot{y}_P\mathbf{E}_2 \\
&= \ddot{x}\mathbf{E}_1 + \ddot{y}\mathbf{E}_2 + \ell\ddot{\vartheta}\mathbf{e}_1 + \ell\dot{\vartheta}^2\mathbf{e}_2.
\end{aligned} \tag{I.1.2}$$

Referring to Figure I.1(a), in addition to a gravitational force $-mg\mathbf{E}_2$ acting at $\bar{X}$, a normal force $N\mathbf{E}_2$ and a friction force $F_f\mathbf{E}_1$ act at P.

The angle ϑ has a restricted range for the case of interest. The minimum value of ϑ, which we denote by $\vartheta_{\min}$ occurs when the block rests on the side of length h and the maximum value of $\vartheta_{\max}$ occurs when the block rests on the side of length w. The extreme angles can be readily computed using the corresponding values for the position vector $\ell\mathbf{e}_2$. Omitting details of the computation, we find that

$$\vartheta \in \left(\vartheta_{\min} = -\arctan\left(\frac{h}{w}\right), \vartheta_{\max} = \arctan\left(\frac{w}{h}\right) \right). \tag{I.1.3}$$

The variation of this pair of angles as functions of the aspect ratio $\frac{w}{h}$ of the block are shown in Figure I.2(a). For blocks where $\frac{w}{h} = 0.5$, $\vartheta_{\min} = -63.435°$ and $\vartheta_{\max} = 26.565°$. For a slender rod of length 2ℓ, the corresponding range of ϑ is $\vartheta \in \left(-\frac{\pi}{2}, \frac{\pi}{2}\right)$.

We now use (I.1.2) and the balances of linear and angular momenta for the block to establish the following equations of motion:

$$\begin{aligned}
m\ddot{x}_P &= F_f + \frac{\ell\cos(\vartheta)}{I}\left(F_f\ell\cos(\vartheta) + N\ell\sin(\vartheta)\right) - m\ell\dot{\vartheta}^2\sin(\vartheta), \\
m\ddot{y}_P &= N - mg + \frac{\ell\sin(\vartheta)}{I}\left(F_f\ell\cos(\vartheta) + N\ell\sin(\vartheta)\right) + m\ell\dot{\vartheta}^2\sin(\vartheta), \\
I\ddot{\vartheta} &= F_f\ell\cos(\vartheta) + N\ell\sin(\vartheta).
\end{aligned} \tag{I.1.4}$$

where

$$\begin{aligned}
y_P N &= 0, \quad y_P \geq 0, \quad N \geq 0, \\
\dot{x}_P &= 0 \Rightarrow -\mu_s N \leq F_f \leq \mu_s N, \\
\dot{x}_P &\neq 0 \Rightarrow F_f = -\mu_d N \operatorname{sgn}(\dot{x}_P).
\end{aligned} \tag{I.1.5}$$

In (I.1.4) and (I.1.5), $I = \frac{m}{12}\left(w^2 + h^2\right)$ is the moment of inertia of the block, μ_s is the coefficient of static Coulomb friction, and μ_d is the coefficient of dynamic Coulomb friction.

We henceforth restrict attention to the case where $\dot{x}_P \neq 0$. It is convenient to use the following non-dimensionalizations:

$$\tau = \sqrt{\frac{g}{\ell}}t, \qquad u_P = \frac{y_P}{\ell}, \qquad n = \frac{N}{mg}, \tag{I.1.6}$$

to show that $(\text{I.1.4})_2$ implies that

$$u_P'' = \mathsf{a} + \mathsf{b}n \tag{I.1.7}$$

where

$$\begin{aligned}
\mathsf{a} &= \mathsf{a}\left(\vartheta, \vartheta'\right) = \vartheta'^2 \cos\left(\vartheta\right) - 1, \\
\mathsf{b} &= \mathsf{b}\left(\vartheta, \operatorname{sgn}\left(\dot{x}_P\right), \mu_d\right) = \left(1 + 3\cos\left(\vartheta\right) - 3\mu_d \cos\left(\vartheta\right)\sin\left(\vartheta\right)\operatorname{sgn}\left(\dot{x}_P\right)\right).
\end{aligned} \tag{I.1.8}$$

where the prime denotes the derivative with respect to τ.

The dimensionless expression for u_P'' enables us to readily use analyses on the incidence of Painlevé's paradox for a slender rod. Following [27, 50, 64], the contact problem can be formulated as a linear complementary problem. That is, we seek u_P and n such that

$$nu_P'' = 0, \quad n \geq 0, \qquad u_P'' \geq 0, \tag{I.1.9}$$

where (cf. (I.1.7)) $u_P'' = \mathsf{a} + \mathsf{b}n$. As shown in [27, 50, 69], a pair of possible solutions, $n = 0$ and $n = -\frac{\mathsf{a}}{\mathsf{b}}$, occurs when $\mathsf{a} > 0$ and $\mathsf{b} < 0$ and no solutions are possible when $\mathsf{a} < 0$ and $\mathsf{b} \leq 0$. That is, the Painlevé paradoxes occur when $\mathsf{b} \leq 0$.

With the help of (I.1.7) and (I.1.8), we can determine regions in the $\mu_d - \vartheta$ plane where Painlevé's paradoxes occur by examining the sign of the function $\mathsf{b}\left(\vartheta, \operatorname{sgn}\left(\dot{x}_P\right), \mu_d\right)$. The results are shown in Figure I.2(b) and parallel the classic results for a rod of length ℓ that date to Painlevé with the caveat that the range of ϑ is restricted by the geometry of the block (cf. (I.1.3)). In particular, regardless of the sign of the slip speed $\dot{x}_P$ or the aspect ration $\frac{w}{h}$, the minimum value of the coefficient of friction required for the paradox is $\mu_d = \frac{4}{3}$ - a value which is far higher that the one used in our numerical work with the stack of blocks.

I.2 The Case of a Line of Contact

We now turn to the situation shown in Figure I.1(b). The block in this case has an entire side of length w in contact with the rough horizontal surface. We assume that the contact forces can be modeled as a pair of normal, $N_R\mathbf{E}_2$ and $N_L\mathbf{E}_2$, and friction forces $F_{f_R}\mathbf{E}_1$ and $F_{f_L}\mathbf{E}_1$ applied at the edges of the block. The material points at the edges of the block are labelled X_L and X_R:

$$\begin{aligned}
\mathbf{x}_L &= x_L\mathbf{E}_1 + y_L\mathbf{E}_2 = \bar{\mathbf{x}} - \frac{w}{2}\mathbf{e}_1 - \frac{h}{2}\mathbf{e}_2, \\
\mathbf{x}_R &= x_R\mathbf{E}_1 + y_R\mathbf{E}_2 = \bar{\mathbf{x}} + \frac{w}{2}\mathbf{e}_1 - \frac{h}{2}\mathbf{e}_2.
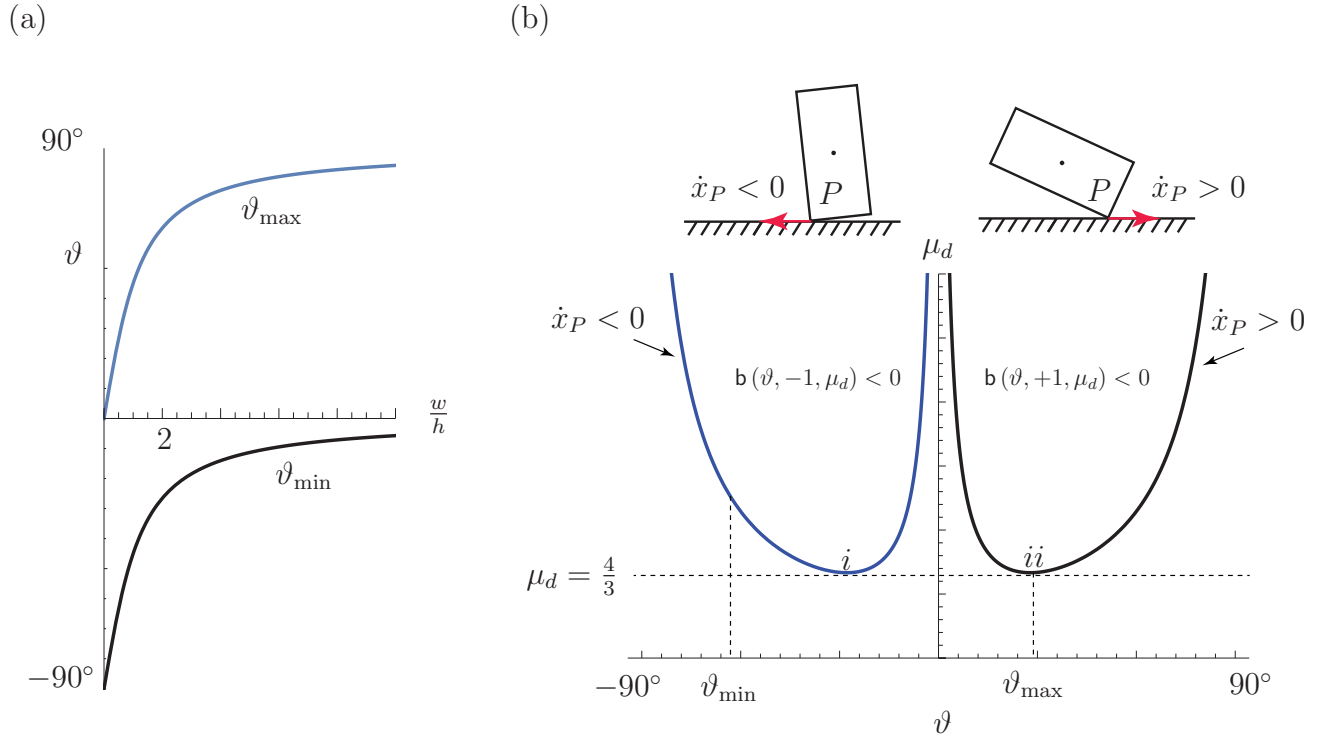\end{aligned} \tag{I.2.1}$$

Figure I.2: (a) The values of the angles $\vartheta_{\min}$ and $\vartheta_{\min}$ as functions of the aspect $\frac{w}{h}$. (b) The loci of points in the $\vartheta - \mu_d$ plane where $\mathsf{b}\left(\vartheta, \mathrm{sgn}\left(\dot{x}_P\right), \mu_d\right) = 0$. The loci determine the region $\mathsf{b} \leq 0$ in the $\vartheta - \mu_d$ plane where the Painlevé paradoxes occur. The values of $\vartheta_{\min} = -64.435°$ and $\vartheta_{\max} = 26.565°$ for $\frac{w}{h} = 0.5$ are shown. The points labeled i and ii correspond to the values of $\vartheta = \pm 26.6^o$ and $\mu_d = \frac{4}{3}$ - which is the minimum value of μ_d where the Painlevé paradoxes occur.

The balances of linear and angular momenta for the block provide the following equations of motion:

$$m\ddot{x} = F_{f_R} + F_{f_L},$$
$$m\ddot{y} = N_R + N_L - mg$$
$$I\ddot{\vartheta} = \frac{w}{2}\left(-F_{f_R} + F_{f_L}\right)\sin\left(\vartheta\right) + \frac{h}{2}\left(N_R + N_L\right)\sin\left(\vartheta\right) + \frac{w}{2}\left(N_R - N_L\right)\cos\left(\vartheta\right) \qquad \text{(I.2.2)}$$
$$+ \frac{h}{2}\left(F_{f_R} + F_{f_L}\right)\cos\left(\vartheta\right),$$

where

$$
\begin{aligned}
y_R N_R = 0, \quad & y_R \geq 0, \quad N_R \geq 0, \\
y_L N_L = 0, \quad & y_L \geq 0, \quad N_L \geq 0, \\
\dot{x} = 0 \Rightarrow -\mu_s N_R \leq F_{f_R} \leq \mu_s N_R \quad & \& \quad -\mu_s N_L \leq F_{f_L} \leq \mu_s N_L, \\
\dot{x} \neq 0 \Rightarrow F_{f_L} = -\mu_d N_L \mathrm{sgn}\left(\dot{x}_L\right) \quad & \& \quad F_{f_R} = -\mu_d N_R \mathrm{sgn}\left(\dot{x}_R\right).
\end{aligned}
\tag{I.2.3}
$$

These equations can be non-dimensionalized:

$$
\tau = \sqrt{\frac{g}{\ell}} t, \qquad u_{R,L} = \frac{y_{R,L}}{\ell}, \qquad n_{R,L} = \frac{N_{R,L}}{mg},
\tag{I.2.4}
$$

where $2\ell = \sqrt{w^2 + h^2}$.

We now parallel the analysis used previously and formulate the linear complementary problem:

$$
\begin{aligned}
u_R'' n_R = 0, \quad u_R'' \geq 0, \quad & n_R \geq 0, \\
u_L'' n_R = 0, \quad u_L'' \geq 0, \quad & n_L \geq 0.
\end{aligned}
\tag{I.2.5}
$$

With the assistance of (I.2.2), we find that

$$
\begin{bmatrix} u_R'' \\ u_L'' \end{bmatrix} = \mathsf{b} \begin{bmatrix} n_R \\ n_L \end{bmatrix} + \mathsf{a},
\tag{I.2.6}
$$

where

$$
\begin{aligned}
\mathsf{a} = \hat{\mathsf{a}}\left(\vartheta, \vartheta'\right) &= \begin{bmatrix} -1 + \left(\frac{h}{2\ell}\cos\left(\vartheta\right) - \frac{w}{2\ell}\sin\left(\vartheta\right)\right)\vartheta'^2 \\ -1 + \left(\frac{h}{2\ell}\cos\left(\vartheta\right) + \frac{w}{2\ell}\sin\left(\vartheta\right)\right)\vartheta'^2 \end{bmatrix}, \\
\mathsf{b} = \hat{\mathsf{b}}\left(\vartheta, \mathrm{sgn}\left(\dot{x}_L\right), \mathrm{sgn}\left(\dot{x}_R\right), \mu_d\right) &= \begin{bmatrix} 1 & \frac{h}{2\ell}\sin\left(\vartheta\right) + \frac{w}{2\ell}\cos\left(\vartheta\right) \\ 1 & \frac{h}{2\ell}\sin\left(\vartheta\right) - \frac{w}{2\ell}\cos\left(\vartheta\right) \end{bmatrix} \begin{bmatrix} 1 & 1 \\ \delta_1 & \delta_2 \end{bmatrix},
\end{aligned}
\tag{I.2.7}
$$

where

$$
\begin{aligned}
\delta_1 &= \frac{m\ell}{2I}\left(h\sin\left(\vartheta\right) + w\cos\left(\vartheta\right)\right) - \mu_d\mathrm{sgn}\left(\dot{x}_R\right)\frac{m\ell}{2I}\left(h\cos\left(\vartheta\right) - w\sin\left(\vartheta\right)\right), \\
\delta_2 &= \frac{m\ell}{2I}\left(h\sin\left(\vartheta\right) - w\cos\left(\vartheta\right)\right) - \mu_d\mathrm{sgn}\left(\dot{x}_L\right)\frac{m\ell}{2I}\left(h\cos\left(\vartheta\right) + w\sin\left(\vartheta\right)\right).
\end{aligned}
\tag{I.2.8}
$$

We now restrict attention to the case $\vartheta = 0$ and $\vartheta' = 0$. Thus, $\dot{x}_L = \dot{x}_R = \dot{x}$. In this case, b is invertible with eigenvalues 2 and $\frac{mw^2}{4I}$ and respective eigenvalues:

$$
\mathsf{e}_1 = \begin{bmatrix} \frac{1 - \frac{mw^2}{4I}\left(1 + \mu_d\mathrm{sgn}(\dot{x})\frac{h}{w}\right)}{1 - \frac{mw^2}{4I}\left(1 - \mu_d\mathrm{sgn}(\dot{x})\frac{h}{w}\right)} \\ 1 \end{bmatrix}, \qquad \mathsf{e}_2 = \begin{bmatrix} -1 \\ 1 \end{bmatrix}.
\tag{I.2.9}
$$

The solution to the LCP problem (I.2.5) can be found from (I.2.6),

$$
n_R = \frac{1}{2}\left(1 + \mu_d\mathrm{sgn}\left(\dot{x}\right)\frac{h}{w}\right), \qquad n_L = \frac{1}{2}\left(1 - \mu_d\mathrm{sgn}\left(\dot{x}\right)\frac{h}{w}\right).
\tag{I.2.10}
$$

Thus, the Painlevé paradoxes are absent from this case.